The Thesis Committee for Corey Anthony Joy
Certifies that this is the approved version of the following thesis:

The Effects of Pressure Variations and Chemical Reactions on the Elasticity of the Lower Tuscaloosa Sandstone of the Cranfield Field, Mississippi

APPROVED BY
SUPERVISING COMMITTEE:

Supervisor:

Mrinal Sen

Robert Tatham

Kyle Spikes

The Effects of Pressure Variations and Chemical Reactions on the Elasticity of the Lower Tuscaloosa Sandstone of the Cranfield Field, Mississippi

by

Corey Anthony Joy, B.S.M.E.

Thesis

Presented to the Faculty of the Graduate School of

The University of Texas at Austin

in Partial Fulfillment

of the Requirements

for the Degree of

Master of Science in Geological Sciences

The University of Texas at Austin

August 2011

Dedication

I dedicate this to my family, Cyrus Sr., Alicia, Cyrus Jr. and Gary, my friends, the scientific community, and, last but certainly not least, Sabrina Marie.

Acknowledgements

I would like to acknowledge my supervisor, Dr. Mrinal Sen, for his guidance, support, and invaluable expertise in the field of geophysics. His dedication to my education and personal growth as his student has made this project possible.

Tiziana Vanorio's interest in my work and the field of rock physics helped this project take off. The countless hours Tiziana and Yael Ebert dedicated to my project during my time at Stanford's rock physics lab were invaluable. Thank you.

I give thanks to my committee, Dr. Robert Tatham and Dr. Kyle Spikes. Thank you Dr. Tatham for the time you spent helping me perfect this thesis. Thank you Dr. Spikes for fueling my interest in rock physics and encouraging me to strive for great results.

I would like to acknowledge Jiemin Lu for helping me select core samples, putting extra time in the lab, and giving me the insight in order to integrate geochemistry into my study.

I would also like to thank Kevin Dodds (BP), the EDGER Forum, Sue Hovorka, and the entire Gulf Coast Carbon Center (UT BEG) for data and support.

Lastly, I would like to thank my fellow students, especially Mohammed Alhussain, Terence Campbell, and Bruce Frederick.

This research was partially supported by the Center for Frontiers of Subsurface Energy Security, an Energy Frontier Research Center funded by the U.S. Department of Energy, Office of Science, Office of Basic Energy Sciences under Award Number DE-SC0001114. Core on which these experiments were conducted was collected as part of the Southeast Regional Carbon Sequestration Partnership Phase III project supported by

the U.S. Department of Energy (DOE) National Energy Technology Laboratory (NETL) under Grant Number DEFE FC26-05NT42590. This project is administered by the Southern States Energy Board.

August 5th, 2011

Abstract

The Effects of Pressure Variations and Chemical Reactions on the Elasticity of the Lower Tuscaloosa Sandstone of the Cranfield Field, Mississippi

Corey Anthony Joy, MSGeoSci

The University of Texas at Austin, 2011

Supervisor: Mrinal Sen

Compliance with current and evolving federal and commercial regulations require the monitoring of injected carbon dioxide for geological sequestration. The goal of this project is to provide geophysicists with tools to quantitatively interpret seismic data for the amount of carbon dioxide retained in subsurface reservoirs. Rock physics can be used to predict the effects on the seismic response of injecting carbon dioxide on the reservoir. However, classical rock physics models fail when chemical reactions alter the microstructure of the host rock. These chemically induced changes can stiffen or soften the rock frame by precipitation or dissolution, respectively, of minerals in the pore space. Increasing pore pressure is another effect of sequestering carbon dioxide. The amount of change in the microstructure due to chemical reactions and pressure variations depends

on the reservoir into which the fluid is injected. Therefore, measuring velocities on site-specific subsurface core samples may provide the ability to differentiate between chemical reactions and pressure variations on the elastic properties of the reservoir rock.

Core samples come from the Lower Tuscaloosa Sandstone of the Cranfield study area in Mississippi. The experiments consisted of injecting core plugs with carbon dioxide rich brine and measuring compressional and shear velocities at different effective pressures. The elastic moduli of the rock frame are calculated from the measured elastic wave propagation velocities at specific injected pore volumes and effective pressures.

Injecting carbon dioxide rich brine into sandstone core samples, which are composed on average of 80% quartz and 20% clay minerals, resulted in softening of the rock frame due to the dissolution of iron bearing minerals. The moduli exponentially decreased with injected pore volumes and were linearly proportional to effective pressure. The bulk modulus and rigidity of the more quartz rich sample decreased by 13% and 6.5%, respectively, due to a combined effect of changing differential pressure from 35 MPa to 27 MPa and injecting CO2-rich brine. For the more clay rich sample, the moduli decreased by even larger percentages (39.0% and 20.1%, respectively), which could have significant implications on time-lapse seismic data and subsequent estimations of injected CO_2 volumes.

Table of Contents

List of Tables

List of Figures

Chapter 1: Introduction

With indications that anthropogenic carbon dioxide is a contributor to global warming, scientists, engineers and policy makers have proposed that storing the greenhouse gas in the subsurface might be a viable solution. The effectiveness of carbon capture and storage (CCS) to mitigate global warming depends on the amount of carbon dioxide stored and the length of time it is stored in the subsurface. Therefore, injecting carbon dioxide into depleted oil and gas reservoirs or saline aquifers poses unique issues in monitoring and quantifying the amount ultimately retained in the subsurface.

Various surface-based geophysical technologies exist that indirectly measure fluid (liquid or gas) volumes in the subsurface. Commonly used geophysical techniques include seismic reflection, gravity, electric, magnetic and electromagnetic methods. The purpose of this thesis is to contribute tools needed to quantitatively interpret time-lapse reflection seismic data by incorporating the effects of pressure variations and chemical reactions on elastic rock properties.

Conventional fluid substitution models have been used to partially explain time-lapse seismic signatures caused by injecting fluids into the subsurface (Mikkelsen, 2009). Current rock physics models, however, break down when the microstructure of the host rock undergoes changes caused by pressure, temperature and chemical reactions (Vanorio et al., 2010). Chemical reactions may induce microstructural changes by dissolving or precipitating minerals inside the pore space and at grain boundaries within the rock. For example, the injection of carbon dioxide into a saline aquifer, composed of calcite-cemented quartz sandstone, may produce carbonic acid. The carbonic acid can dissolve the calcite cement, which then alters the bulk elastic properties of the host rock. Increasing the pore pressure in the aquifer may also decrease the stiffness of the host rock

by decreasing differential pressure. The complex effects of geologically sequestering carbon dioxide, for example, cannot be fully explained with currently applied models. They must be determined experimentally for each site. The Cranfield Detailed Area Study (DAS) is the study area for this thesis.

CRANFIELD HISTORY AND GEOLOGY

Cranfield is located in Adams County, southwest Mississippi as shown in figure 1.1. This field was discovered in 1943 and has a long history of oil and gas production. Water was injected in 1958-1959 to enhance oil recovery on the western side of the field (Mississippi Oil and Gas Board, 1966). These efforts to enhance oil recovery proved ineffective and were suspended, and the field was abandoned in 1966. After 40 years of pressure re-equilibration, Denbury Resources, Inc. believed the field was a good candidate for enhanced oil recovery (EOR) using carbon dioxide injection (Lu et al., 2011). Denbury's project provided others the opportunity to use this EOR project to study injected CO_2 from a geologic sequestration (CCS) viewpoint. The Gulf Coast Carbon Center of the Bureau of Economic Geology at The University of Texas in Austin is working in conjunction with Southeast Regional Carbon Sequestration Partnership on the CCS aspect. The project is supported by National Energy Technology Laboratory and the U.S. Department of Energy and managed by the Southern States Energy Board (SECARB, 2011).

The Cranfield DAS provides an ideal opportunity to study the effects of injecting carbon dioxide into the saline leg of a deep reservoir. Denbury Resources, Inc., began injecting carbon dioxide into the reservoir in July 2008 at a rate of 1 million tons per year. By early 2011, the mass of injected, non-recycled CO_2 totaled 2.5 million tons. The source of the injected CO_2 occurs naturally and is produced from Jackson Dome near

Jackson, Mississippi. Denbury Resources, Inc., transports the carbon dioxide by pipeline to the injection site on the eastern flank of the field (Lu et al., 2011). The location of the one km^2 DAS within in the field is shown in figure 1.1. The DAS consists of one injection well and two observation wells (CFU 31F#1, 2 and 3, respectively), which are structurally downdip of the injection well (Figure 1.2). The two observation wells provide the opportunity to diligently study the process using geophysical, geochemical, and petroleum engineering methods.

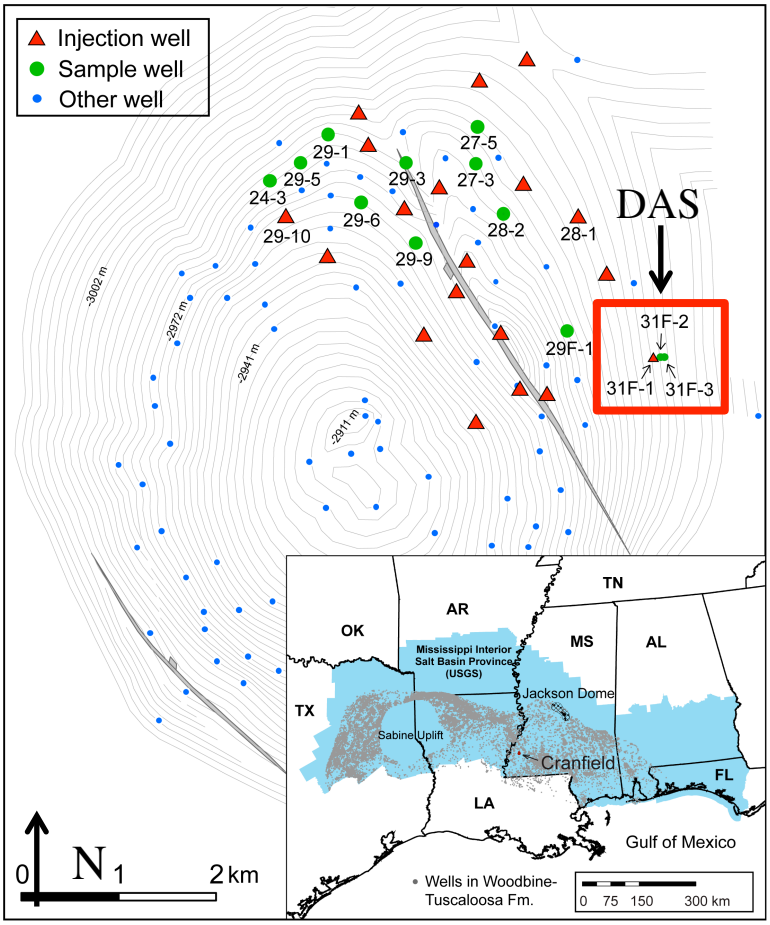

Figure 1.1: Depth structure map (contour interval = 3m) of the top of the Lower Tuscaloosa Sandstone of the Cranfield DAS and geographical location of Cranfield, MS. The rectangle denotes the location of the detailed area study. (Lu et al., 2011)

Figure 1.2: Cranfield DAS infrastructure. (Photo courtesy of Romanak, 2010)

The structure of the Cranfield field is a salt-cored, domed anticline as seen in the depth structure map (Figure 1.1). There are two major normal faults striking NW-SE (330˚). One fault cuts through the southwestern flank of the field, and the other is in the northeast. The regional stratigraphy of the reservoir and seals consists of sand-shale sequences In the Late Cretaceous Tuscaloosa group (figure 1.3). The reservoir is the basal Sand (with minor conglomerates) of the Upper Cretaceous Lower Tuscaloosa Formation, which is porous (20%) and permeable (0.1-1000 millidarcies). The Lower Tuscaloosa Sandstone "consists of vertically stacked, fluvial point-bar and channel deposits" (Lu et al., 2011), which are described in the type section (figure 1.4). The thickness of the reservoir ranges from 10 m to 25 m. There are an abundance of reservoir seals in the area. The immediate, local seal in the DAS is a mudstone roughly 8 m thick. A regional seal form the Middle Tuscaloosa Formation, open-marine shale and mudstone, is nearly 75 m thick.

System	Series	Group in MS & Eastern LA	Formation	Sedimentary environment
Cretaceous	Late Cretaceous	Eagle Ford	Eagle Ford	Open-marine
		Tuscaloosa Group	Upper Tuscaloosa	Fluvial-deltaic-marine complex
			Middle Tuscaloosa	Shallow open-marine
			Lower Tuscaloosa	Fluvial-deltaic-complex
	Early	Washita	Washita	Open-marine

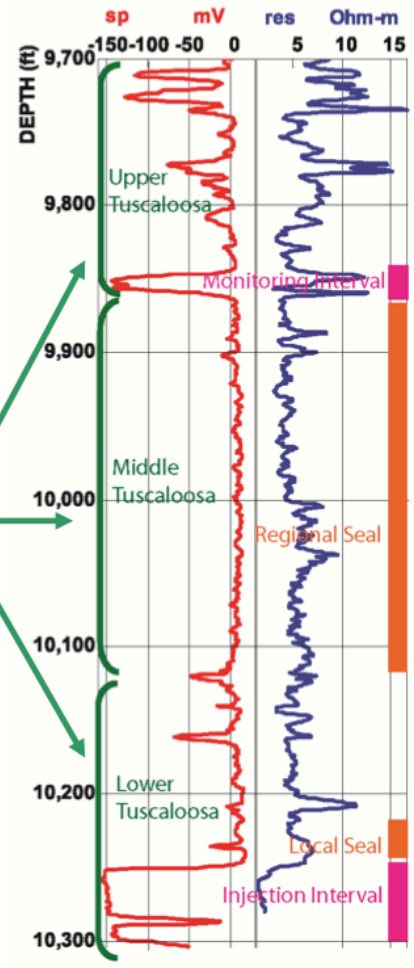

Figure 1.3: Regional stratigraphy with spontaneous potential and resistivity well logs. (From Kordi et al., 2010)

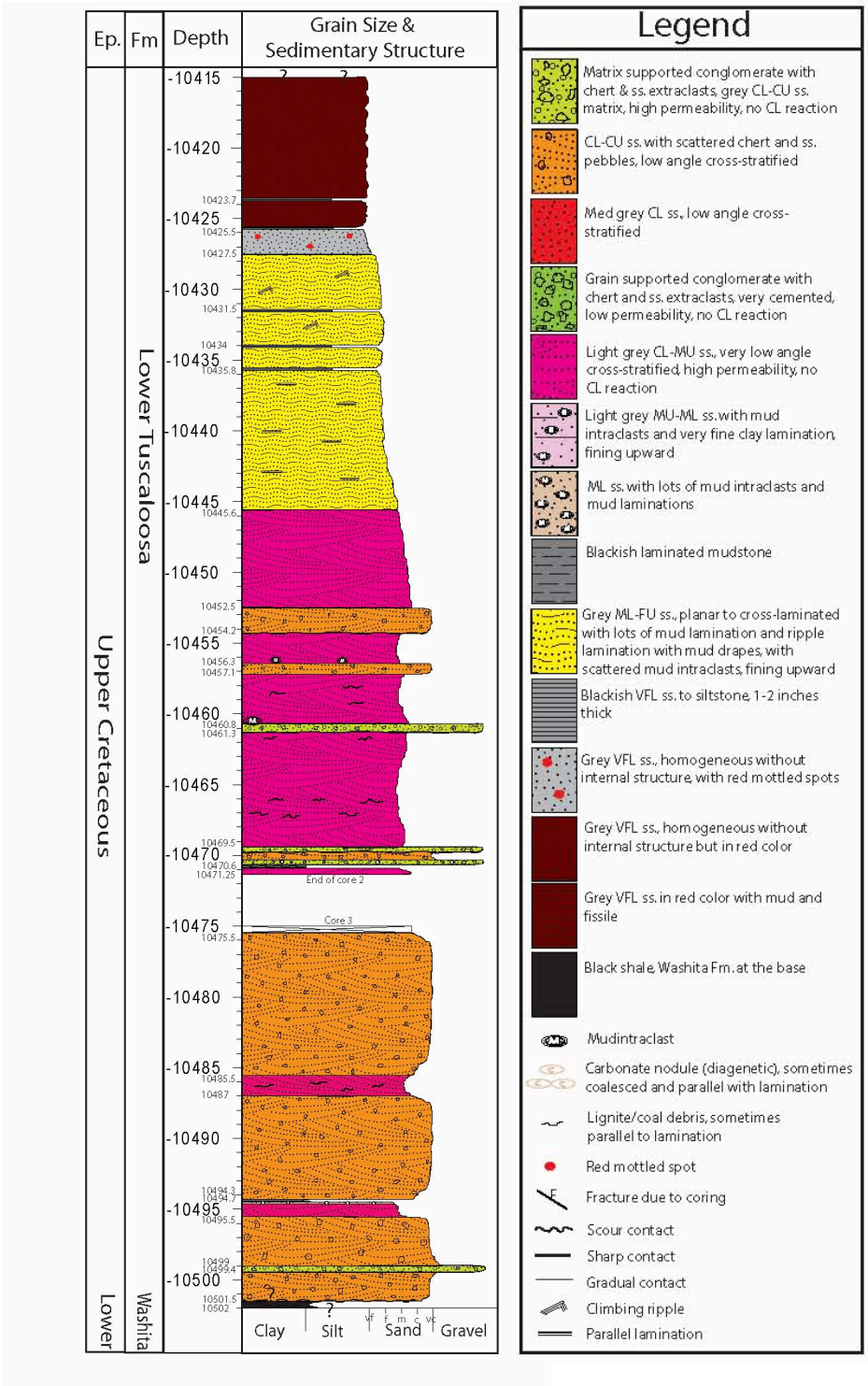

Figure 1.4: Type section of observation well CFU 31F # 2 Lower Tuscaloosa formation. (From Kordi et al., 2010)

PROJECT OUTLINE

This thesis develops a hypothesis (chapter 2) and an accompanying experimental confirmation (chapter 3) to determine changes in elastic properties associated with changing pore pressure and precipitation or dissolution of minerals. Chapter 2 develops the hypothesis of how excess stiffness and excess compliance can describe the bulk elastic effects caused by minerals precipitating or dissolving in the pore space or at grain contacts. Also, the assumptions and limitations of the hypothesis are addressed.

The experimental method and apparatuses are described in chapter 3. The function and limitation of each apparatus is explained in detail. After introducing the equipment, the experimental variables are stated. The variables include the composition of the injected fluid, the confining pressure on the core plugs, and the pore pressure at which the fluid is injected. Finally, the experimental protocol is described, which consists of injecting carbon dioxide rich brine into a core sample and observing seismic velocities at various differential pressures. Using a Scanning Electron Microscope (SEM), Images of the core samples are taken before and after injection to qualitatively describe how the microstructure of the core samples has changed.

The results of the experiment are presented in chapter 4, which describes both composition of the injected fluid and sample characterization before and after injecting carbon dioxide-rich brine. An empirical relationship between elastic properties and injected pore volumes is stated for the current differential pressure acting on the reservoir. The dependency of the bulk elastic moduli on differential pressure and injected pore volumes are graphically depicted. Using these results, possible seismic implications are described in chapter 5. The chapter consists of building acoustic impedance models before and after injection, post-stack seismic modeling, and amplitude versus angle of incidence analysis.

PREVIOUS WORK

There has been a great effort in studying the effects of CO_2 injection from the standpoint of multiple disciplines, such as geophysics, geochemistry, and petroleum engineering. For example, Mikkelsen (2009) attempted to model the effects of pressure variation and CO_2 saturation on seismic velocities. However, they did not include the chemical effects of injecting carbon dioxide. Hovorka (2009) and Kharaka et al. (2006) studied the gas-water-rock interactions in the clastic Frio formation. Lu et al. (2011) researched the geochemical effects of injecting carbon dioxide into the Lower Tuscaloosa Sandstone Formation in the Cranfield Field. Vilarrasa et al. (2010) determined the effects of CO_2 compressibility on CO_2 storage in deep saline aquifers, which describes how CO_2 plumes form after injection. Very little research has been performed that combines multiple disciplines. Vanorio et al. (2011) led the way by injecting carbon dioxide rich brine into carbonate samples. However, they did not include the effects of pressure variations on elastic properties when carbon dioxide is injected. The goal of this thesis is to complement the work of Vanorio et al. (2011) with the added complexity of pressure variations.

REFERENCES

Hovorka, S., 2009, Frio brine pilot: The first U.S. sequestration test, *Southwest Hydrology*, **8**(5), 26-31.

Kharaka, Y.K., Cole, D.R., Hovorka, S.D., et al., 2006, Gas-water-rock interactions in Frio Formation following CO2 injection: Implications for the storage of greenhouse gases in sedimentary basins, *Geol*., 34(7): 577-580.

Kordi, M., Hovorka, S., Milliken, K., Treviño, R., and Lu, J., 2010, Diagenesis and reservoir heterogeneity in the Lower Tuscaloosa Formation at Cranfield Field, Mississippi: presented at the 60th Annual Convention of the Gulf Coast Association of Geological Societies and the Gulf Coast Section of SEPM, San Antonio, Texas, October 10-12, 2010. GCCC Digital Publication Series #10-13.

Lu, J., Kharaka, Y., Thordsen, J., Horita, J., Karamalidis, A., Griffith, C., Hakala, A., Ambats, G., Cole, D., Phelps, T., Cook, P., Manning, M., and Hovorka, S., 2011, Geochemical interactions in the Lower Tuscaloosa reservoir at the Cranfield CO_2 sequestration site, Mississippi, USA, Elsevier Editorial System for Chemical Geology, in press.

Mikkelsen, E. R., 2009. Monitoring of CO_2 sequestration at the Longyearbyen CO_2 lab by time-lapse seismic, Master's thesis, Norwegian University of Science and Technology.

Mississippi Oil and Gas Board, 1966. Mississippi Oil and Gas Board (MOGB), Cranfield Field, Cranfield unit, basal Tuscaloosa reservoir, Adams and Franklin Counties, pp. 42-58.

Romanak, K.D., 2010, Monitoring CO_2 storage in deep geological formations: presented at the University of Bern, Bern, Switzerland, November 10th, 2010. GCCC Digital Publication Series #10-17.

Southeast Regional Carbon Sequestration Partnership (SECARB), 2011, Phase III early CO2 injection field test at Cranfield.

Vanorio, T. et al., 2010. The rock physics basis for 4D seismic monitoring of CO2 fate: Are we there yet?. *The Leading Edge*, Feb., 156-162.

Vanorio, T., Nur, A., and Ebert, Y., 2011, Rock physics analysis and time-lapse rock imaging of geochemical effects due to the injection of CO2 into reservoir rocks, *Geophysics*, in press.

Vilarrasa, V., Bolster, D., Dentz, M., Olivella, S., and Carrera, J., 2010, Effects of CO2 compressibility on CO2 storage in deep saline aquifers, Springer, *Transport in Porous Media*, 11242.

Chapter 2: Chemical Fluid Substitution Theory

Classical fluid substitution calculations fail when the injected fluid chemically reacts with the host rock, thus changing the mechanical properties of the rock. If minerals precipitate on and between grains or dissolve in the pore space, the elastic moduli of the rock frame may change significantly. Therefore, sole use of classical fluid substitution models using non-reactive fluids, such as Gassmann's (1951) or Brown and Korringa's (1975), are likely to fail. The presence of a reactive fluid, or reactant, can induce changes (decrease or increase) in seismic wave propagation velocities of the host rock beyond that predicted by Gassmann's fluid substitution calculations (Vanorio et al. 2010). I hypothesize that in addition to the compliance or stiffness induced by mechanical fluid substitution, dissolution or precipitation induces excess compliance or stiffness, respectively, due to the chemical reaction of the reactant with the host rock. The magnitude of changes in elastic properties should depend on the mineralogy of the host rock, the composition of the reactant, and time of the reaction. Also, the elastic properties depend on differential pressure, P_D, which is confining pressure less pore pressure. The dependency of elastic properties on differential pressure is determined experimentally and included in the fluid substitution model in a general way.

This study is motivated by the need to understand the effects of carbon dioxide saturation on the elastic properties of rock for the purpose of seismically monitoring carbon dioxide in the subsurface. This mechanical-chemical problem is too complex to generalize to all combinations of host rock and reactant in the current study. In the most general case, core samples from each reservoir under consideration for storing carbon dioxide should undergo the necessary rock physics tests pre- and post-carbon dioxide injection to determine the candidacy of the reservoir for carbon dioxide storage.

HYPOTHESES

There are three primary hypotheses that describe why, how and for what duration the elastic properties change. The baseline refers to the host rock before the injection of reactant. The reactant is injected incrementally and quantified by injected pore volumes. The total injected volume of reactant normalized by the total volume of pore space is called a pore volume,

2.1 $$V_N = {V_{Injected\ Reactant}}\Big/{V_{Pore}},$$

where V_N is the normalized injected pore volumes, $V_{Injected\ Reactant}$ is the actual volume of injected reactant, and V_{Pore} is the total volume of pores. A value of V_N>1 suggests that reactive fluid is swept through the rock.

Excess compliance/stiffness

I hypothesize that a chemical reaction of a reactant with the host rock induces excess compliance or stiffness in the "dry" frame that is not predicted by mechanical fluid substitution models. The increase or decrease in compliance is due solely to dissolution or precipitation, respectively, of minerals. That is

2.2 $$S^*_{eff} = S^*_0 \pm S_{chem},$$

and

2.3 $$\nu^*_{eff} = \nu^*_0 \pm \nu_{chem},$$

where S is bulk compliance, ν is shear compliance, S_{eff}^* and ν_{eff}^* are the effective bulk and shear compliances, respectively, of the "dry" frame after the chemical reaction has occurred, S_0^* and ν_0^* are the bulk and shear compliance, respectively, of the "dry" frame prior to fluid substitution, and S_{chem} and ν_{chem} are the excess bulk and shear, respectively, compliances, induced by the chemical reaction. Addition of compliances corresponds to

dissolution, and subtraction corresponds to precipitation. It is the resultant effective compliance that is then used in a fluid substitution model as the properties for the "dry" frame. This hypothesis can be used with the scalars above or with complete compliance tensors.

Exponential change in elasticity with injected fluid

The elastic properties should change at various rates with respect to injected pore volumes of reactant and time of exposure to the reactant. In the present experiments, I do not address time of exposure to the reactant, but do address total injected volumes of reactant. These rates are also associated with each combination of rock and reactant. The rate of reactions depends on various parameters, such as the reactant, the concentration of the reactant, composition of reacting surface, area and volume of the reacting surface, pressure, temperature, permeability, porosity amount and type, and flow rates, to name a few. Overall, I assume that the bulk and shear moduli change exponentially with concentration and the amount of injected pore volumes. Assuming a constant reactant concentration and differential pressure, the elastic parameters of the "dry" frame, K^*_{eff} and μ^*_{eff}, behave as equations 2.4 and 2.5.

2.4 $$K^*_{eff}(V_{Norm}) = K^*_0 + K^*_\infty(1 - e^{-\zeta_K V_{Norm}}) \quad \text{and}$$

2.5 $$\mu^*_{eff}(V_{Norm}) = \mu^*_0 + \mu^*_\infty(1 - e^{-\zeta_\mu V_{Norm}}),$$

where K^*_0 and μ^*_0 are the baseline bulk and shear moduli of the "dry" frame, K^*_∞ and μ^*_∞ are the limits of the bulk and shear moduli of the "dry" frame as injected pore volumes approaches infinity, and ζ_K and ζ_μ describe the elastic sensitivity to a chemical reaction. The basis for this assumption is that chemical reactions tend to occur exponentially with concentration described by the Arrhenius equation, where the majority of the reaction occurs quickly and reaches steady state (Kotz et al., 2009). If the mineral precipitates or

dissolves in the pore space exponentially with injected volume of reactant, the elastic moduli should also change exponentially.

Critical injected pore volumes

The chemical compliance or stiffness can reach a maximum. This occurs when the chemical reactions cease with injected pore volumes. The chemical reactions cease when no more reactive minerals are available to react with the reactant. For a given concentration of reactant, the number of injected pore volumes that corresponds to the chemically induced compliance or stiffness within 0.5% of its maximum is called critical injected pore volumes.

THEORY

The theory of linear elasticity (Hooke's Law) is used to develop this model. The general form of Hooke's law can be used to define changes in elastic parameters for the case of a fully anisotropic linear elastic medium. For example,

2.6 $\sigma_{ij} = C_{ijkl}\varepsilon_{kl}$,

or

2.7 $\varepsilon_{kl} = S_{klij}\sigma_{ij}$,

where σ_{ij} is the second rank tensor of stress ε_{kl} is the second rank tensor of strain, C_{ijkl} is the fourth rank tensor of stiffness, and S_{klij} is the fourth rank tensor of compliance. I assume homogeneity and isotropy to simplify the initial stages of this model, but this model can be expanded to include anisotropic materials. Only two independent elastic coefficients, λ – "fluid incompressibility" and μ – "rigidity", are required to fully describe an isotropic solid (e.g., Timoshenko and Goodier, 1934), which is expressed as Hooke's Law

2.8 $\sigma_{ij} = \lambda\varepsilon_{\alpha\alpha}\delta_{ij} + 2\mu\varepsilon_{ij}$.

where δ_{ij}=1 when i=j, and δ_{ij}=0 when i≠j. The bulk modulus, K, is

2.9 $$K = \lambda + \frac{2}{3}\mu.$$

Next, a major assumption is that the total porosity change with fluid injection is negligible, i.e.

2.10 $$\phi_1 \approx \phi_2,$$

where ϕ_1 is the porosity before fluid substitution, and ϕ_2 is the porosity after fluid substitution. Therefore, the mechanical fluid substitution models do no have to be updated to accommodate the change in porosity. Finally, the theory includes the assumptions of the mechanical fluid substitution model. I employ Gassmann's fluid substitution model. Therefore, the other assumptions are the rock is isotropic, the moduli are homogenous, and the fluid within the pore space is able to flow freely and equilibrate with applied stress and strain. The last assumption makes this model valid at low seismic frequencies.

The validity of this model relies on the idea that the rock sample is initially fully saturated with the in-situ fluid, which represents the baseline case for the microstructure. The initial saturant, brine, in the sample is then replaced by the reactant, H_2CO_3. In this example, some of the injected carbon dioxide dissolves into the brine to form the reactant, carbonic acid (H_2CO_3), and the rest remains in free-phase as a supercritical fluid. The procedure is broken into two parts in order to address the two processes: chemical reactions and mechanical fluid substitution. First, the effective elasticity of the "dry" frame is determined from the injected pore volumes of reactant and differential pressure. Second, the effective P and S-wave velocities are determined through Gassmann's fluid substitution model.

If a chemical reaction occurs, the effective rigidity, in particular, may increase or decrease. The chemical effect of the reactant is measured by the relative decrease or

increase in shear wave velocity as functions of injected pore volumes. For example, the shear wave velocity of the "dry" frame after a given amount of injected reactant is

2.11 $$V_S^* = \sqrt{\frac{\mu^*}{\rho^*}},$$

where the superscript * represents properties of the "dry" frame, V_S^* is shear wave velocity, ρ^* is the density, and $\mu^*$is the effective rigidity. The effective rigidity of the "dry" frame, μ^*, is

2.12 $$\mu^* = (V_S^*)^2 \rho^*.$$

The hypothesis states that

2.13 $$\nu_{eff}^* = \nu_0^* \pm \nu_{chem},$$

where the subscript 0 represents baseline properties, ν_{eff}^* is the effective shear compliance of the "dry" frame after chemical reactions have occurred, ν_0^* is the baseline compliance of the "dry" frame, and ν_{chem} is the chemical shear compliance. The shear compliance, ν, is inversely related to rigidity, μ, i.e.

2.14 $$\nu = \frac{1}{\mu}.$$

Therefore,

2.15 $$\frac{1}{\mu_{eff}^*} = \frac{1}{\mu_0^*} \pm \frac{1}{\mu_{chem}},$$

and

2.16 $$\mu_{chem} = \left[\pm \frac{1}{\mu_{eff}^*} \mp \frac{1}{\mu_0^*}\right]^{-1}.$$

A similar derivation is used for the bulk modulus using the velocity of a P-wave, V_P^*,

2.17 $$V_P^* = \sqrt{\frac{K^* + \frac{4}{3}\mu^*}{\rho^*}},$$

where K^* is the bulk modulus of the "dry" frame. Therefore, the effective bulk modulus of the "dry" frame is

2.18 $K^* = (V_P^*)^2\rho^* - \frac{4}{3}\mu^*$.

The hypothesis states that

2.19 $S_{eff}^* = S_0^* \pm S_{chem}$,

where the compliance, S, is inversely related to bulk modulus, K, i.e.

2.20 $S = \frac{1}{K}$.

Substituting the compliances of the hypothesis with the inverse of bulk modulus of each component gives

2.21 $\frac{1}{K_{eff}^*} = \frac{1}{K_0^*} \pm \frac{1}{K_{chem}}$.

The parameter of interest, K_{chem}, is then given by

2.22 $K_{chem} = \left[\pm\frac{1}{K_{eff}^*} \mp \frac{1}{K_0^*}\right]^{-1}$.

Now the problem is fully defined for fluid substitution calculations.

The updated fluid substitution model, which is based on Gassmann's model, that can handle changing elastic parameters caused by chemical reactions or pressure variations is

2.23

$$K_{sat}(V_N, P_D) = K_{eff}^*(V_N, P_D) + \frac{\left(1 - {K_{eff}^*(V_N,P_D)}/{K_M}\right)^2}{\left({\phi}/{K_{fl}} + {(1-\phi)}/{K_M} - {K_{eff}^*(V_N,P_D)}/{K_M^2}\right)},$$

where K_{sat}, K_M, K_{fl} are the bulk moduli of the saturated rock, mineral matrix and pore fluid, respectively, and ϕ is the fractional porosity. The bulk modulus of the mineral matrix, K_M, can be approximated using the Voigt-Reuss-Hill average (Hill, 1952) of the minerals that the rock is composed of. Assuming the constituent minerals are quartz and clay minerals,

2.24 $K_M = \frac{1}{2}\left[\left(V_{clay}K_{clay} + V_{qtz}K_{qtz}\right) + \left(\frac{V_{clay}}{K_{clay}} + \frac{V_{qtz}}{K_{qtz}}\right)^{-1}\right]$,

where V_{clay} and V_{qtz} are the volume fractions of clay minerals and quartz, respectively, and K_{clay} and K_{qtz} are the bulk moduli of clay minerals and quartz, respectively. The bulk modulus of a uniform or patchy fluid mixture, K_{fl}, is the harmonic or arithmetic average, respectively, of the bulk moduli of the fluid components weighted by volumetric fraction. For example, the bulk modulus of a uniform fluid mixture, which is based on an iso-stress model, is

2.25 $$K_{fl} = \left(\frac{V_{CO2}}{K_{CO2}} + \frac{V_W}{K_W}\right)^{-1},$$

where V_{CO2} and V_W are the volume fractions of free-phase CO2 and brine, respectively, and K_{CO2} and K_W are the bulk moduli of free-phase CO2 and brine, respectively. The bulk modulus of a patchy fluid mixture, which is based on an iso-strain model, is

2.26 $$K_{fl} = V_{CO2}K_{CO2} + V_W K_W.$$

According to the Gassmann formulation,

2.27 $$\mu_{sat} = \mu^*_{eff}(V_N, P_D),$$

where μ_{sat} is the shear modulus of the saturated rock.

SIMULATION

The first part of simulating a hypothesis is to quality check the end limits of the theory, which are velocities approaching zero and infinity. Consider a simple case where the P- and S-wave velocities of a dry core plug are measured before and after a series of injections of reactant. The core plug is dry in order to avoid any dispersion effects from a fluid filling the pore space. Therefore, changes in velocity are caused by changes in elastic properties of the "dry" frame of the core plug. The behavior of the effective shear and bulk moduli can be seen in figure 2.1 as functions of a fractional change in velocity. The excess shear and bulk compliance/stiffness of the simplistic models are displayed in figure 2.2. In both figures, the curves are broken into two sections, precipitation and

dissolution. Precipitation corresponds to stiffening of the "dry" frame and an increase in fractional change in velocity; dissolution corresponds to softening of the "dry" frame and a decrease in fractional change in velocity.

The maximum Vp and Vs of the "dry" frame can decrease is -100%, which indicates the velocities are zero. The effective elastic parameters approach zero as the fractional change in velocity approaches -100%, a physically unrealistic limit because energy considerations require $K>0$ and $\mu>0$ (Mavko et al., 2009). In this model, I did not put a limit on the positive or negative maximum fractional change in velocity to test the end members. As shown in the experimental results (Chapter 4), Vp and Vs reach minimum and maximum values when minerals have entirely filled the pore space or entirely dissolved leaving behind the original matrix. The maximum velocities depend on the pore filling material and the matrix. Various rock physics models, such as the Dvorkin and Nur's (1996) contact-cement model, can predict how stiffness changes with increasing mineral precipitation.

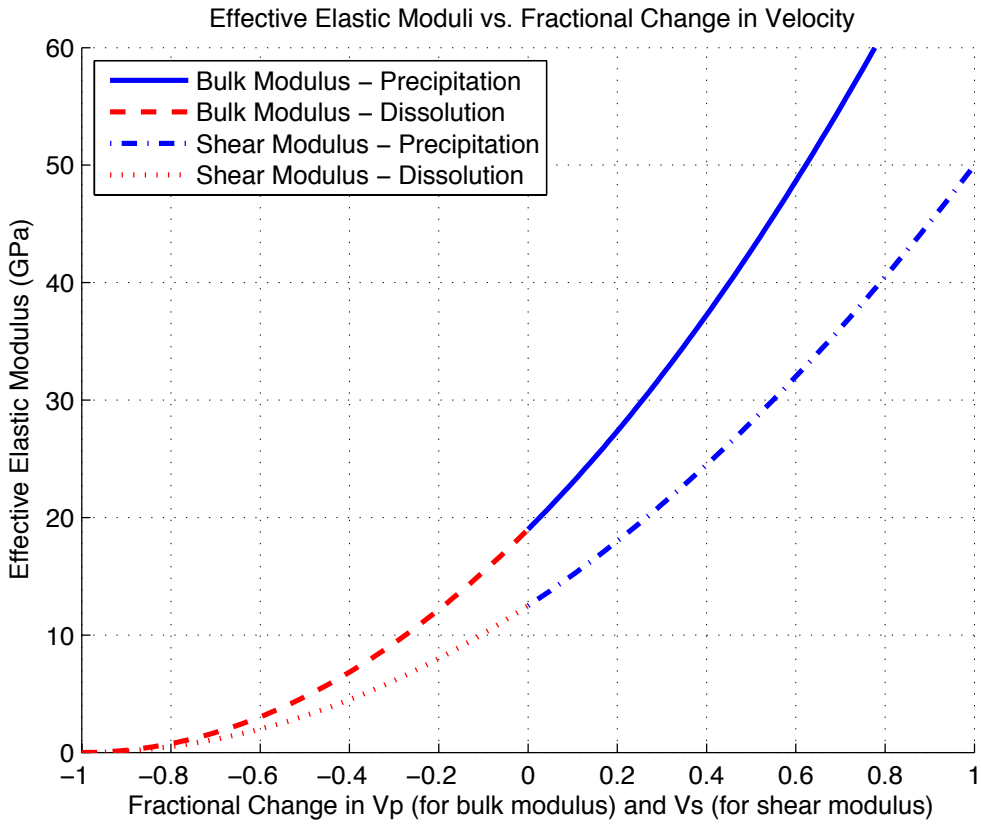

Figure 2.1: Effective bulk and shear moduli of the "dry" frame as functions of fractional change in Vp (for the bulk modulus) and Vs (for the shear modulus) caused by precipitation (increasing velocity) or dissolution (decreasing velocity). The effective moduli increase for increasing fractional change in velocity due to precipitation of minerals. The effective moduli decrease for decreasing fractional change in velocity due to dissolution of minerals.

The chemical bulk and shear moduli approach infinity as Vp and Vs approach zero fractional change in velocity. Therefore, the effective stiffness is equal to the baseline stiffness according to the proposed iso-stress model, which indicates the sample has not undergone any microstructural changes. Also, the excess chemical bulk modulus and rigidity approach zero as the fractional change in velocity approaches zero. The chemical moduli equal zero as a limit, which drives the effective moduli to zero. On the

other hand, the chemical moduli approach the value of the baseline moduli for increasing fractional change in velocity with precipitation, which causes the velocity to approach positive infinity.

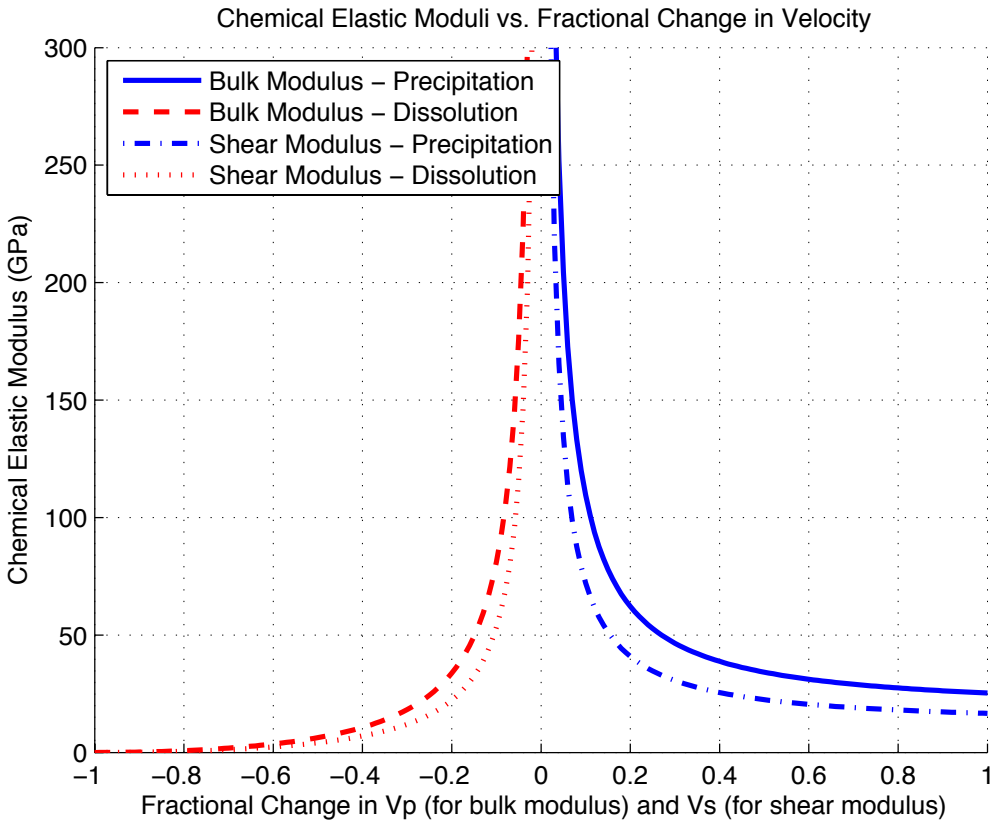

Figure 2.2: Chemical bulk and shear moduli as function of fractional change in Vp (for the bulk modulus) and Vs (for the shear modulus) caused by precipitation (increasing velocity) or dissolution (decreasing velocity). The chemical bulk and shear moduli approach infinity as the fractional change in Vp and Vs approach zero. The chemical elastic moduli approach zero GPa as Vp and Vs approach zero. Whereas the chemical moduli approach zero GPa as the Vp and Vs approach infinity, which is why the curves are not symmetric about zero fractional change in velocity.

The effects of chemical fluid substitution are shown in figures 2.3 and 2.4. The fluid substitution is performed while taking into account the changing elasticity of the

"dry" frame. The baseline bulk modulus and rigidity are 19 GPa and 12.5 GPa, respectively. The relationship between the elastic parameters of the "dry" frame (the constants of equation 2.4 and 2.5) and injected pore volumes was arbitrarily chosen. The density was kept constant. The bulk modulus and density of brine were 2.5 GPa and 1.1 g/cm^3 respectively (Mavko et al., 2009). The mechanical properties of carbon dioxide significantly depend on pressure and temperature. For consistency, the reservoir temperature and pore pressure after CO_2 injection were used to calculate density and bulk modulus, which are 90ºC and .04 GPa respectively. According to the Span and Wagner (1996) equation of state, the density of the supercritical CO_2 is 0.781 g/cm^3 and the bulk modulus is 0.23 GPa. Note that CO_2 saturation is only a function of the volumetric fraction of free-phase CO_2. Free-phase CO_2 is actually inert, and it only becomes reactive when dissolved in water. The bulk modulus of the fluid mixture is 0.63 GPa, which is found using equation 2.23 for a uniform mixture. The density of the fluid mixture is 1.004 g/cm^3. For simplicity, the amount of dissolved carbon dioxide is held constant. Therefore, chemical reactions are only a function of injected pore volumes. Reactions take place with increasing injected pore volumes until the critical injected pore volumes for the bulk and shear moduli.

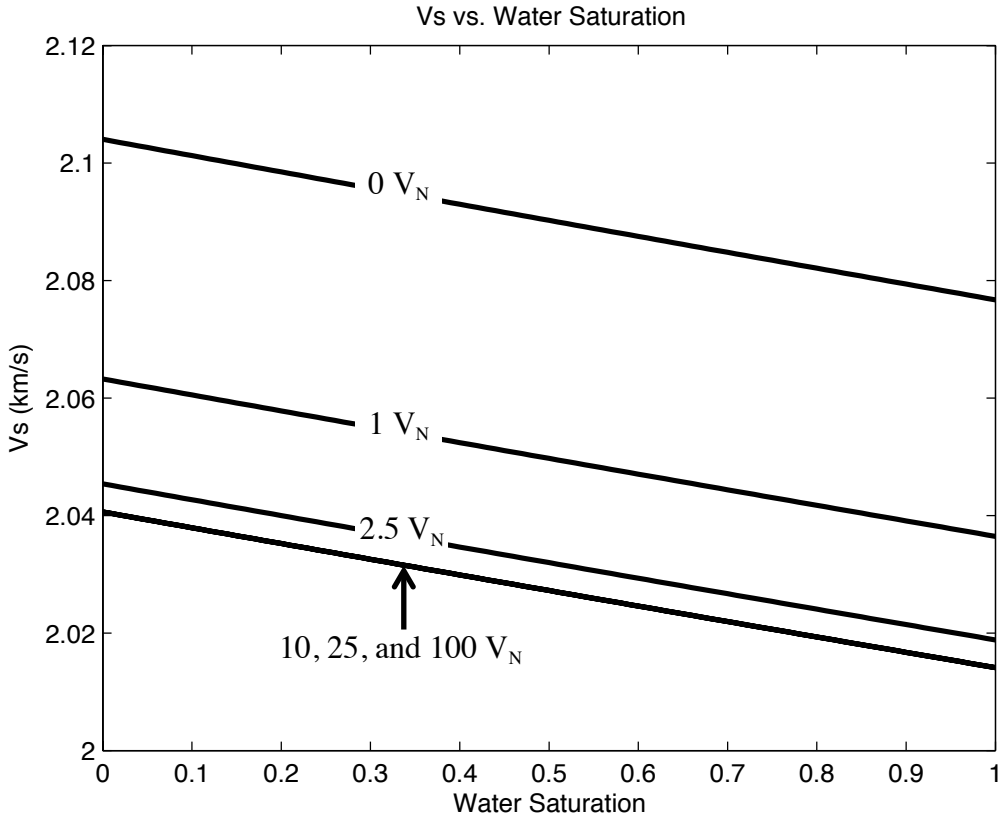

Figure 2.3: Shear wave velocity versus water saturation for various injected pore volumes. Vs decreases with increasing water saturation, because the density of water is greater than that of CO_2. Vs decreases exponentially with increasing injected pore volumes. The velocity for injected pore volumes greater than or equal to 10 overlap, because the sample was injected with the critical amount of pore volumes of reactant.

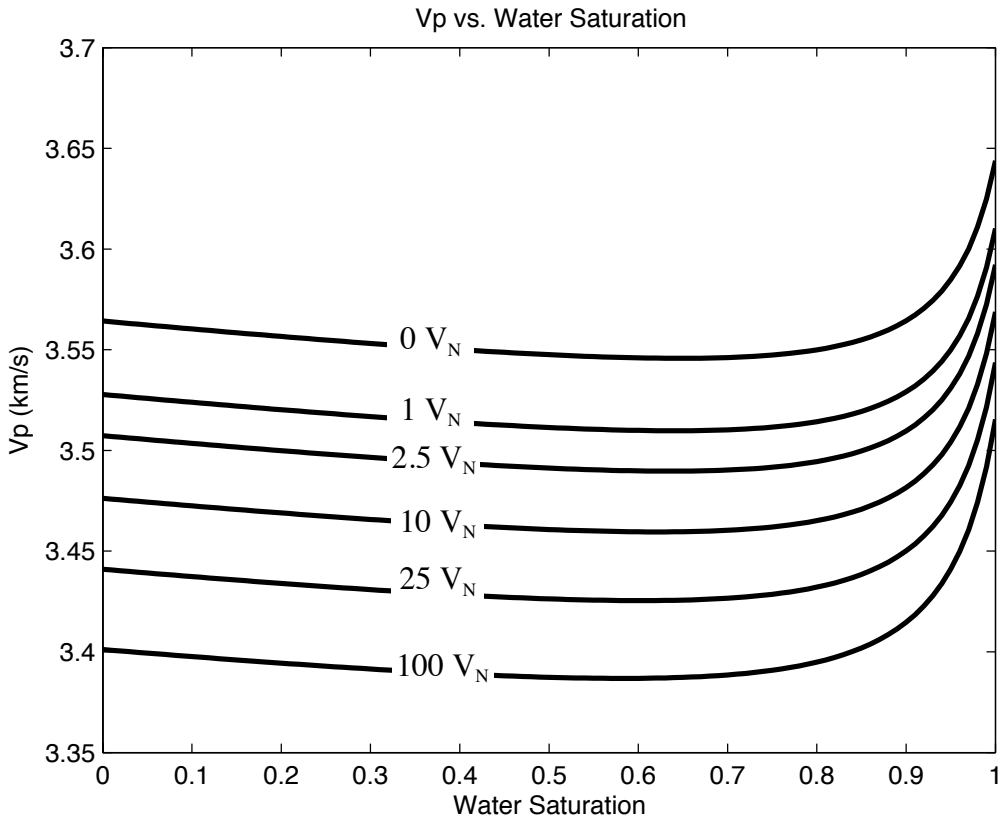

Figure 2.4: Compressional wave velocity versus water saturation for various injected pore volumes. Velocity decreases with decreasing water saturation from 1 to 0.7 and increasing injected pore volumes. Velocity increases with decreasing water saturation from 0.6 to 0 due to density.

Velocity exponentially decays with increasing injected pore volumes, as seen in both figures. Shear wave velocity increases with CO_2 saturation, because the density of CO_2 is less than that of brine. P-wave velocity decreases with decreasing water saturation from about 0.6 to 1 because the bulk modulus of carbon dioxide is less than that of brine. However, Vp increases with decreasing water saturation from 0.6 to 0 because the density of CO_2 is less than that of brine.

DISCUSSION

The terms K_{chem} and μ_{chem} are fitting variables for the wave velocities when the actual wave velocities do not match those predicted by mechanical fluid substitution models. When K_{chem} and μ_{chem} are estimated, one can begin to interpret how the microstructure of the rock has changed. For example, the dissolution of calcite cement in sandstone may change the shape or volume of the pores. The mechanical effects of changing pore shape is much different than changing the volume of the pore while maintaining shape (Walsh, 1965). Essentially, K_{chem} and μ_{chem} represent the induced pore compliances of the chemically affected rock. Changes in the shape of the pore may be caused by non-uniform flow of reactant through the pore space. I hypothesize that the dissolution will occur more drastically at fast fluid flow velocities than slow fluid flow velocities, and vice versa for precipitation. Therefore, dissolution will also be non-uniform if the reactant flow is non-uniform, thus, changing the shape of the pore space.

The changes in elastic properties depend on how and where the chemical reaction occurs. If precipitation occurs, it is possible and likely that the stiffness and rigidity will increase. However, the amount that the elastic parameters increase greatly depends on where the solid phase precipitates. According to Dvorkin and Nur (1996), the bulk modulus may increase slightly if the solid phase precipitates on a grain without making contact with another grain (non-contact cement). The mechanical effects of non-contact cement can be described using the friable sand model (Dvorkin and Brevik, 1999), which treats the reduction in porosity as a sorting trend. On the other hand, the effective elastic properties may increase rapidly with even slight cementation if the cement bridges between two grains, which can also be approximated using the grain contact cement model (Dvorkin and Nur, 1996). The constant cement model assumes that cement is precipitating at and away from grain contacts (Avseth et al., 2000). One can imagine that

the opposite of the above statements is true for dissolution. For example, dissolution of grain contact cement can significantly decrease the stiffness and rigidity of the "dry" frame. However, dissolution of non-contact cement will likely have a small impact on the stiffness of the frame. Note that the Tuscaloosa Sandstone consists of mostly quartz grains, and all effects considered consist of changes in iron bearing minerals and carbonate cement between grains. Carbonate reservoirs have an additional complication of changes in grain properties with the introduction of carbonic acid. Also, there is essentially an endless supply of carbonate that is free to react with carbonic acid. Therefore, porosity could significantly change, thus making my model invalid.

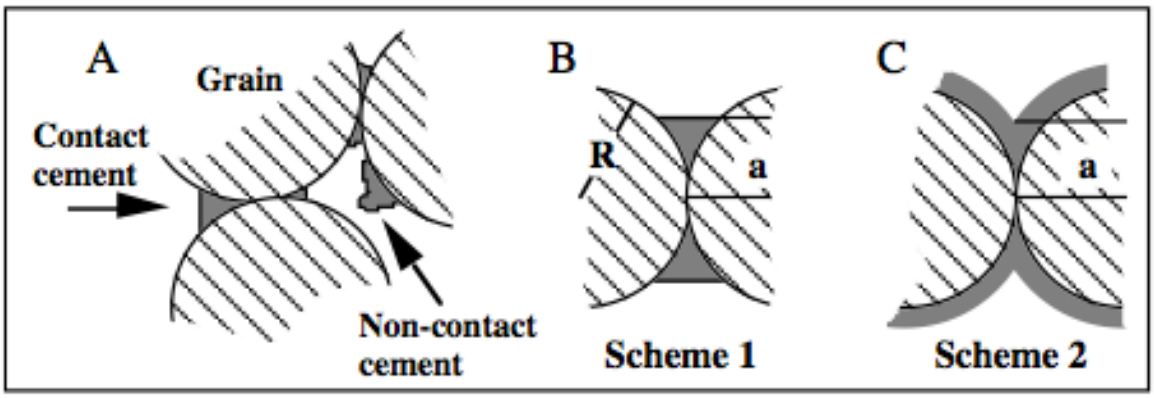

Figure 2.5: (A) Schematic representation of types of cement deposition. (B) All cement deposited at grain contacts. (C) Cement deposited in a uniform layer around the grains. (from Dvorkin and Nur, 1996)

Time is potentially a significant factor for understanding the effects of chemical reactions on the elasticity of rock. A larger degree of dissolution or precipitation will occur if the reaction has more time to take place. However, the reaction may happen so fast that time is not a significant factor when considering long term effects of chemical reactions for time-lapse monitoring. The importance of time depends on the chemical reaction.

CONCLUSION

Chemical fluid substitution is a very complex problem to model. Therefore, it is important to separate mechanical and chemical effects on the elastic properties of the reservoir rock. Separating the two effects enables one to begin to interpret reactant saturation levels and changes in microstructure. Any change in microstructure is caused by the dissolution or precipitation of minerals within the pore space of the host rock. Dissolution of minerals caused by a chemical reaction induces excess bulk and shear compliances in the host rock that is not predicted by Gassmann's mechanical fluid substitution model. Precipitation of minerals caused by a chemical reaction increases the stiffness and rigidity of the host rock not predicted by Gassmann's mechanical fluid substitution model. Depending on the combination of host rock and reactant, there may exist a critical number of injected pore volumes at which the host rock no longer reacts with any further injection. This critical volume defines the maximum change in elastic parameters. Therefore, the rock should behave as Gassmann's model predicts after the critical injected pore volume. The chemical fluid substitution model will break down for appreciable changes in porosity due to the chemical reaction, because the mechanical fluid substitution model must be updated to account for the change in porosity. The chemical fluid substitution model is applicable for negligible changes in porosity, such as the example of carbonic acid dissolving cementing minerals at grain contacts in unconsolidated sandstone.

REFERENCES

Avseth, P., Dvorkin, J., Mavko, G., and Rykkje, J., 2000, Rock physics diagnostic of north sea sands: Link between microstructure and seismic properties. *Geophys. Res. Lett.*, 27(17), 276102764, doi:10.1029/1999GL008468.

Brown, R. and Korringa, J., 1975. On the dependence of the elastic properties of a porous rock on the compressibility of the pore fluid. *Geophys.* **40**, 608-616.

Dvorkin, J. and A. Nur, 1996, Elasticity of High-porosity sandstones: Theory for two North Sea datasets, Geophysics, 61, 1363-1370.

Dvorkin, J., and Brevik, I., 1999, Diagnosing high-porosity sandstones: Strength and permeability from porosity and velocity, *Geophysics*, **64**, 795-799

Gassmann, F., 1951, Über die Elastizität poröser Medien. *Vierteljahrsschrift der Naturforschende Gesellschaft Zürich*, **96**, 1-23.

Hill, R., 1952, The elastic behavior of a crystalline aggregate: *Proc. Phys. Soc. London Ser. A*, **65**, 349-354.

Kotz, J. C., Treichel, P., and Townsend, J. R. 2009. Chemistry and chemical reactivity, vol. 2. Califronia: Thomson Higher Education, 671-703.

Mavko, G., T. Mukerji, and J. Dvorkin, 2009, The rock physics handbook: tools for seismic analysis of porous media, 2nd ed. New York: Cambridge University Press, 21-24.

Span, R. and Wagner, W., 1996. A new equation of state for carbon dioxide covering the fluid region from the triple-point to 1100 K at pressures up to 88 MPa. Journal of Physical and Chemical Reference Data, **25**(6), 1509-1596.

Timoshenko, S.P. and Goodier, J.N., 1934. Theory of Elasticity. New York: McGraw-Hill.

Vanorio, T. et al., 2010. The rock physics basis for 4D seismic monitoring of CO2 fate: Are we there yet?. *The Leading Edge*, Feb., 156-162.

Walsh, J. B., 1965, The effect of cracks on the compressibility of rock: *Journal of Geophysical Research.*, **70**, 381-390.

Chapter 3: Experimental Design

Designing an appropriate protocol for a suite of experiments is a very important step to study a scientific process systematically. This approach enables one to discern the effects among multiple variables. The basis for my experiments is to understand the effects of chemical reactions and pressure variations on the elastic properties of the Tuscaloosa sandstone, but in such a way that the results are directly applicable to the Cranfield DAS. Velocity-pressure data are measured before and after each injection to simulate the effect of varying pore pressure induced by carbon dioxide injection. In order to emulate the chemical reactions that take place in the field, the in-situ conditions of the Tuscaloosa formation must constrain the experiments. Therefore, it is important to match the in-situ fluid, pore pressure, confining pressure, and temperature. However, the experiments are performed at 25ºC to simplify the experimental procedure.

EXPERIMENTAL APPARATUSES

The apparatuses used to measure different parameters of the core plug are a porosimeter, a permeameter, and a pressure vessel. All metal parts are stainless steel to minimize corrosion and chemical reactions from occurring between the metal and the reactive or corrosive fluid.

Porosimeter

The porosimeter measures porosity, or the volume of pores normalized by the volume of the core plug based on Boyle's law. Boyle's law states that the product of pressure and volume of an ideal gas is constant at a given temperature (Schmidt et al., 2006), i.e.,

3.1 $$P_1V_1 = P_2V_2$$

where P is pressure and V is volume. Helium is the ideal gas used to measure porosity, because helium is inert and small relative to the pore size of the samples in this study. The small size of the helium atom allows it to migrate into very small but connected pores.

The porosimeter consists of a helium tank, tubing, a core holder, a helium reservoir, a pressure transducer, and a series of valves to control the flow of gaseous helium. While the valve to the core holder is shut, the gaseous helium flows through the tubing into the reservoir to roughly 0.55 MPa, and then the helium tank is closed off from the system. The system is calibrated by measuring the change in pressure by opening the valve to the core holder of known volume, which establishes the constant value of the product of pressure and volume of helium. The core plug is inserted into the core holder of the calibrated porosimeter. The core holder is closed off from helium. Again, helium flows into the reservoir until the pressure reaches 0.55 MPa, and the helium source is then closed off from porosimeter. The valve to the core plug is opened and the helium flows into the pores of the core plug. The volume of the pores is calculated from drop in pressure based on Boyle's law.

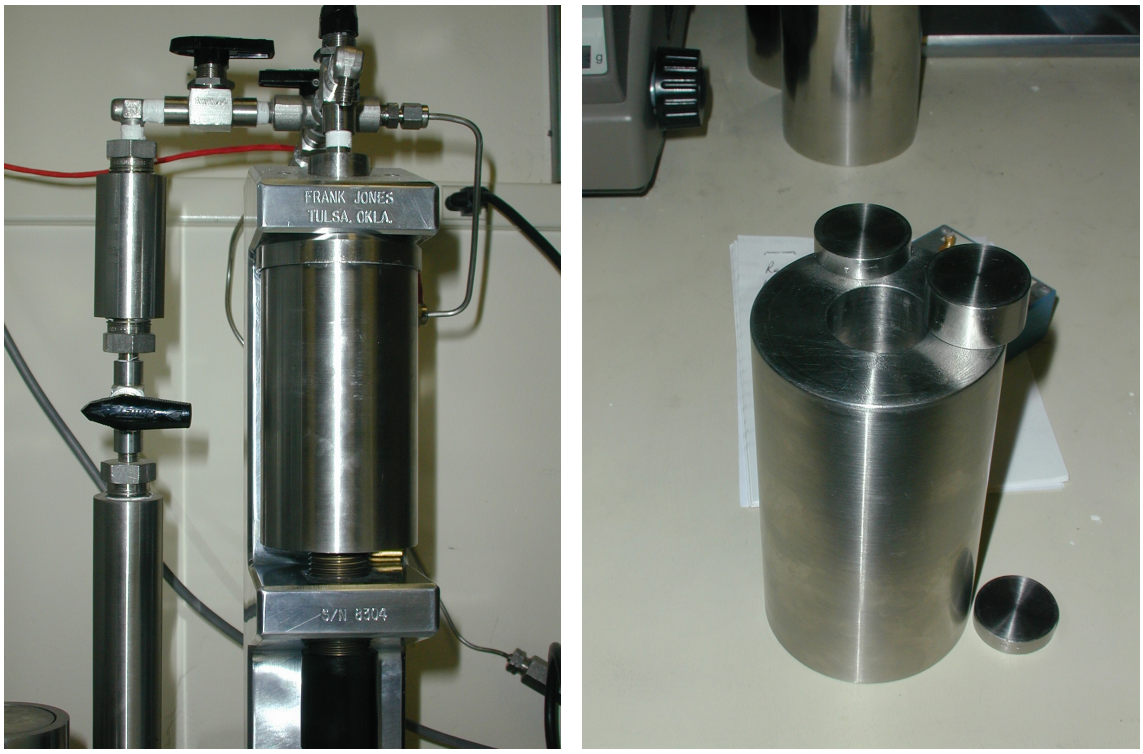

Figure 3.1: Porosimeter (Left) and core holder and billets for the porosimeter (Right). The porosimeter consists of a helium tank (not shown in picture), a helium reservoir (on the left), a core holder (in the front), a pressure transducer (not shown in picture), and a series of valves to control the flow of gaseous helium. Removing different permutations of billets allows the user to put one-inch diameter core plugs of various lengths into the core holder. (Photos courtesy of T. Vanorio, 2011)

Permeameter

The permeameter measures the permeability of a core sample based on Darcy's law using nitrogen gas. Darcy's law relates volumetric flow rate through a porous medium, viscosity of the injected fluid, and inlet and outlet fluid pressure. More specifically, the instantaneous flow rate is

3.2 $$Q = \frac{-kA}{\mu}\frac{(P_{out}-P_{in})}{L},$$

where Q is the flow rate (m^3/s), k is the permeability of the porous medium (m^2), A is the cross-sectional area (m^2) through which the fluid flows, μ is the viscosity of the fluid

(Pa*s), L is the length (m) of the sample, P_{out} is the outlet fluid pressure (Pa) and P_{in} is the inlet fluid pressure (Pa). The length and diameter, which are used to the compute cross-sectional area of the core plug, are measured using a caliper. The outlet and inlet pressures are monitored with a pressure transducer. Flow rate is measured using a flow meter. Viscosity of the gaseous nitrogen is calculated from temperature and pressure. The permeability of the sample is then defined by the measurements and calculated viscosity of the fluid. There is one major caveat when using Darcy's law to calculate permeability. The flow of nitrogen through the core plug must be laminar, which has a Reynolds number less than or equal to ten. The Reynolds number of the nitrogen is

3.3 $$Re = \frac{\rho v d_{30}}{\mu},$$

where ρ is the fluid density, ν is the specific discharge of the fluid, d_{30} is an average grain diameter, and μ is the viscosity of the fluid (Darcy, 1856). For a density of 2 kg/m^3, a specific discharge of 0.009 m/s, an average grain diameter of 0.5 mm, and a viscosity of 0.0002 kg/(m*s), the predicted Reynolds number for the experiments is 0.05. Therefore, the flow of CO_2 through the core plug should be laminar. Very low permeability samples can deviate from Darcy's law due to gas slippage, which is corrected using the Klinkenberg correction. Gas slippage occurs when the mean free path of the gas is the close to the path through the pore space (Klinkenberg, 1941). A throttle valve is used while measuring high permeability samples to keep the differential pressure in an acceptable range for the equipment.

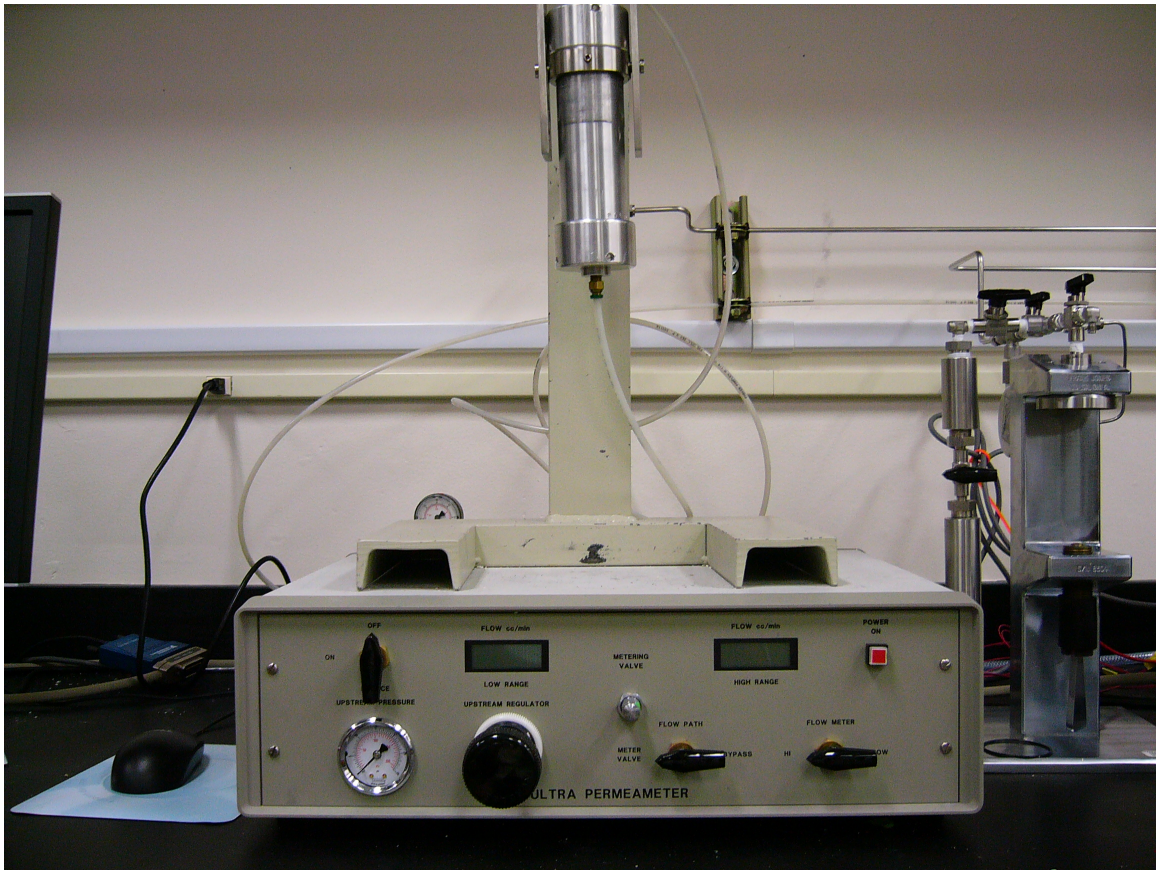

Figure 3.2: Permeameter (Photo courtesy of T. Vanorio, 2011)

Pressure vessel

The pressure vessel allows one to measure the velocity of compressional or shear waves through the core plug at varying confining pressures. The compressional wave velocity of the fluid must be measured using different equipment. The velocity of a wave is based on travel time and the length of the sample. For example,

3.4 $$V = \frac{L}{T},$$

where V is wave velocity, L is the length of the sample, and T is the travel time of the wave through the sample.

The mechanical components of the pressure vessel consist of a reservoir of the injected fluid, a pump to inject the fluid and increase the pore pressure, and an oil reservoir and pump to increase the confining pressure. The pumps are driven by compressed air. Also, there is a metering valve on the outlet of the injected fluid in order to fine tune the outlet flow rate and pore pressure. The maximum confining pressure the system can handle is 60 megapascals (MPa).

The electrical components of the pressure vessel consist of three potentiometers, piezoelectric transducers with longitudinal and shear polarizations, an oscilloscope, and a power supply. The potentiometers indirectly measure the change in length of the sample under different confining pressures. Piezoelectric transducers expand and contract based on the applied voltage, or they produce a voltage when a force is applied to them. In this system, voltage is applied to the transducer housed in the inlet end-cap, which produces a wave of stress that propagates through the sample. Located in the outlet end-cap, the other transducer acts as a receiver by producing a voltage, which is monitored by the oscilloscope, when the stress wave arrives. The peak frequencies of the P- and S-wave transducers are 1 MHz and 0.7 MHz respectively. The accuracy of the velocity measurements was estimated to be roughly ± 1%.

The process for preparing the core plug to measure the compaction curve consists of many steps:

1. Insert sample into the rubber jacket to prevent the pressurizing oil from saturating the sample.
2. Insert the inlet end-cap into the inlet side of the jacketed sample.
3. Insert the outlet end-cap into the outlet side of the jacketed sample.
4. Fasten the outlet end-cap such that it can slide towards and not away from the inlet end-cap.

5. Fasten the electrical potentiometers such that the voltage drop along the potentiometers are approximately the same and within their dynamic range.
6. Apply voltage to the piezoelectric transducers and check waveform signal on the oscilloscope.
7. If the waveform signal is strong enough, insert the end-caps, which are attached to a top-plate, into the pressure vessel
8. Securely fasten the top-plate to the pressure vessel.
9. Now compress the sample.

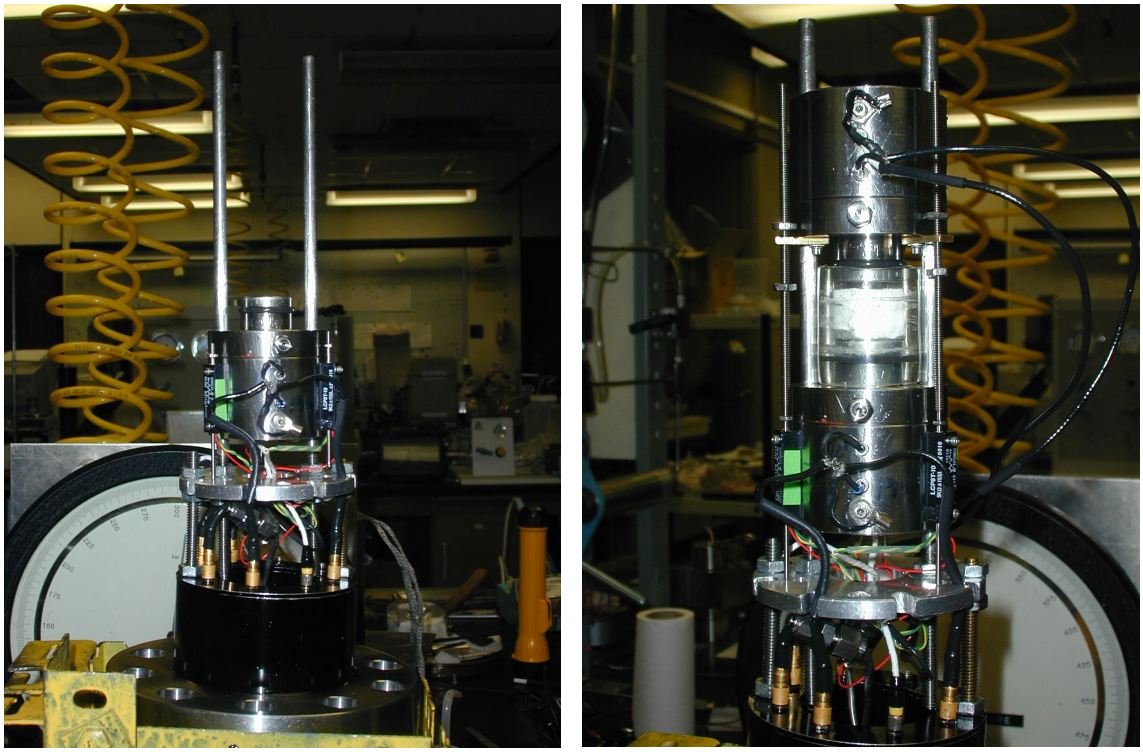

Figure 3.3: The upstream end-cap attached to the top-plate (Left). The core plug jacketed between the two end-caps (Right). (Photo courtesy of T. Vanorio, 2011)

Titrator

The fluid is regularly sampled at the inlet and outlet to measure iron content using the titration method. The HACH LANGE 16900 digital titrator was used with a color indicator and TitraVer 0.0716 M solution titrant to determine iron content of the fluid. Before the titrant is added, the solution of outlet fluid with the color indicator is yellow (figure 3.7). The solution turns red-orange when enough titrant is added to bond with the iron ions (figure 3.8). The concentration of iron is calculated from the total concentration of titrant.

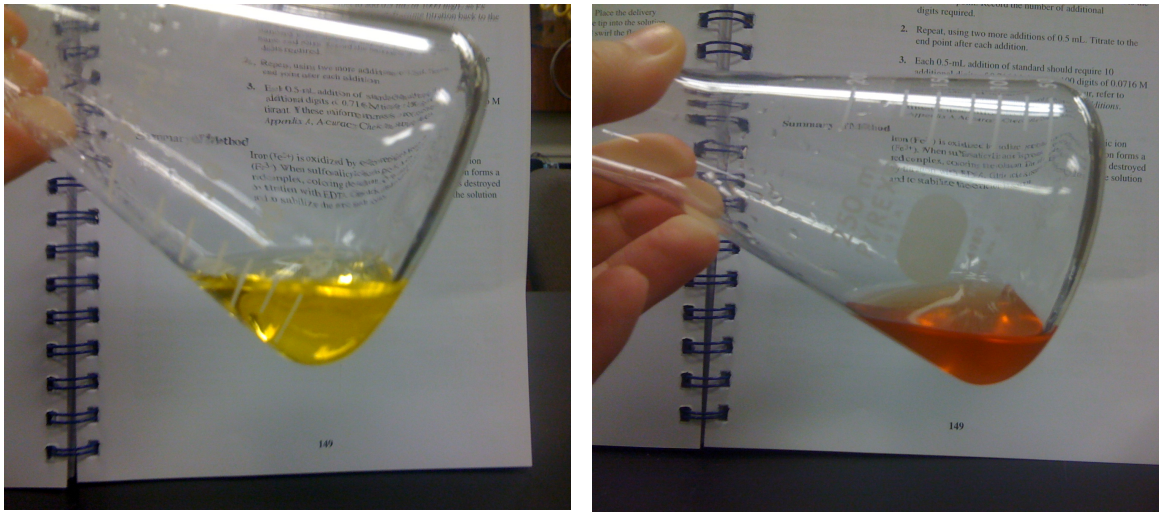

Figure 3.4: Post-injection fluid mixed with an iron color indicator (Left). The yellow color of the solution indicates the presence of iron ions. Solution after titrant is mixed with post-injection fluid and color indicator (Right). The red-orange color of the solution indicates all iron ions are bound to the titrant. (Photo courtesy of T. Vanorio, 2011)

EXPERIMENTAL VARIABLES

In-situ fluid

The brine that saturates the Tuscaloosa formation in Cranfield Field, Mississippi, is a sodium-calcium-chloride type with total dissolved solids of 156 grams per liter, a pH

of 5.8, and density of 1.1 grams per cubic centimeter (g/cm^3). Tuscaloosa brine is composed of many cations and anions, but the main constituents are sodium, calcium, and chloride. The concentrations of sodium, calcium and chloride are 44,500 milligrams per liter, 11,700 milligrams per liter, and 95,300 milligrams per liter respectively (Lu et al., 2011). In order to emulate the concentrations of the major constituents in the field, different quantities of sodium chloride (NaCl) and calcium chloride ($CaCl_2$) were added to one liter of deionized water. It is impossible to match the exact concentrations of the three major ions. Because the presence of calcium affects reactivity, the concentrations of the cations were matched with the results of the water analysis. Therefore, chloride concentration is a product of the concentrations of sodium and calcium.

3.5 $$[Cl^-] = [Na^+] + 2 * [Ca^{2+}],$$

where $[Cl^-]$ is the concentration of chloride ions, $[Na^+]$ is the concentration of sodium ions, and $[Ca^{2+}]$ is the concentration of calcium ions.

In order to add the correct mass of salts to the water, the mass concentrations of sodium, calcium, and chloride ions must first be converted into moles per liter. The number of moles of an ion is

3.6 $$MOL_I = \frac{MASS_I}{MW_I},$$

where MOL_I is the number of moles of the ion, $MASS_I$ is the mass of the ion, and MW_I is the molecular weight of the ion. Using the equation above, the molar concentrations of sodium, calcium, and chloride ions are 1.93 mol/L, 0.29 mol/L, and 2.51 mol/L respectively. The molar concentration of a salt is equal to the respective molar concentration of the cation of the salt. Therefore, the number of moles of sodium chloride and calcium chloride in one liter of water are 1.93 moles and 0.29 moles respectively. The mass of salt to be added is

3.7 $$MASS_{SALT} = \frac{MOLE_{SALT}}{MW_{SALT}},$$

where $MASS_{SALT}$ is the mass of the salt, MOL_{SALT} is the number of moles of the salt, and MW_{SALT} is the molecular weight of the salt. Synthetic Tuscaloosa brine was made by adding 112.9 grams of sodium chloride (NaCl) and 42.6 grams of calcium chloride ($CaCl_2$) to one liter of deionized water. There were 89,100 milligrams per liter of chloride in the synthetic Tuscaloosa brine compared to the 95,300 milligrams per liter in the actual Tuscaloosa brine (Lu et al., 2011).

Matching the pH of the reactive fluid is also very important to simulate the chemical reactions that take place in-situ. The pH of the in-situ brine and the synthetic brine were 5.6 and 5.8 respectively before CO_2 injection. According to Lu et al. (2011), the average pH measured down hole is between 3.5 and 4.0 after each carbon dioxide injection. In the lab, the brine is bubbled with carbon dioxide for approximately 15 minutes at standard temperature and pressure to achieve a pH of 3.4. The pH of the reactant is measured each time before injecting into core plugs.

Confining and pore pressures

Confining pressure plays an important role in simulating the chemical reactions. A pressure column approach was used to resolve the confining stress. According to well logs, the average density is roughly 2.1 grams per cubic centimeter (g/cm^3). The formation under consideration is roughly 3.2 kilometers (km) deep. Therefore, the confining stress is roughly 65 MPa.

The in-situ pore pressure before injection is approximately 31 MPa. The pore pressure after injection depends on the amount of injected reactant, CO_2 in this case, as seen in figure 3.9 (Hovorka et al., 2009). The maximum pore pressure after carbon dioxide injection is approximately 38 MPa. However, due to the limitations of the

pressure vessel, both confining and pore pressures are scaled back by 10 MPa in order to maintain in-situ differential pressure. Therefore, the confining pressure, initial pore pressure, and final pore pressure are 55 MPa, 21 MPa, and 28 MPa respectively.

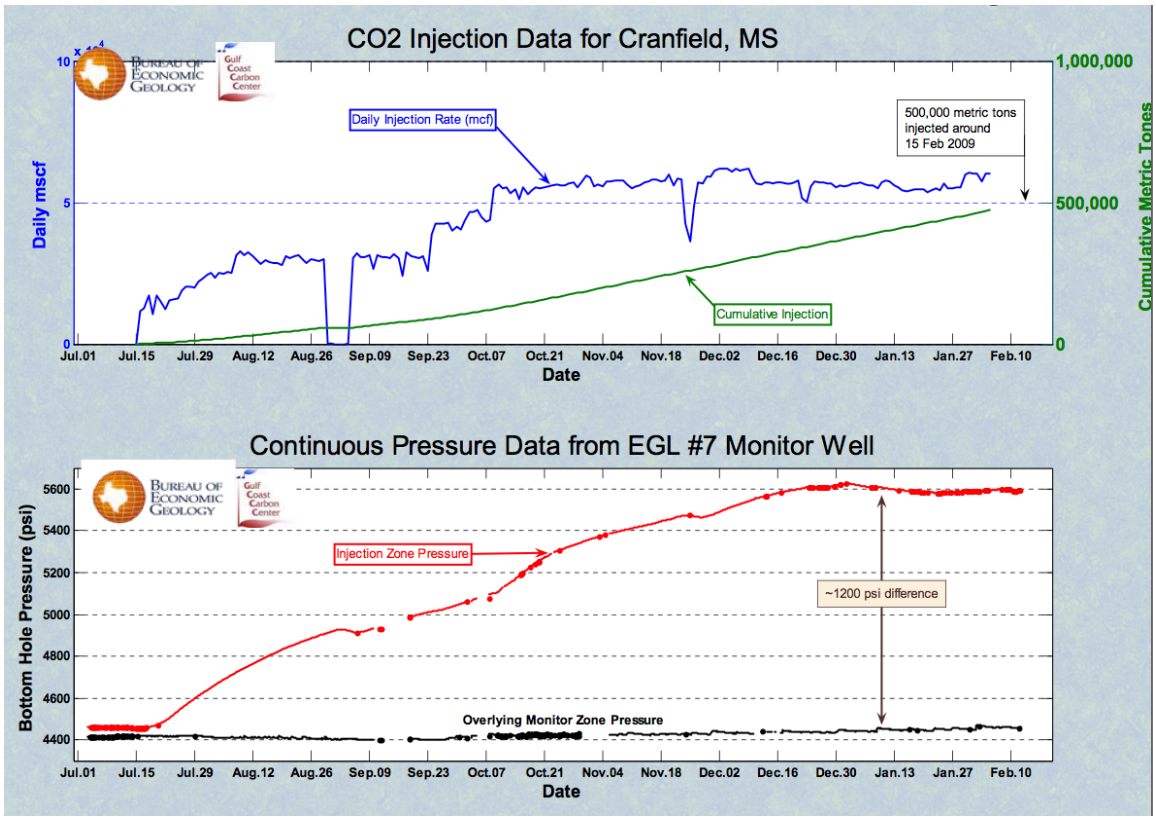

Figure 3.5: Injection rate, cumulative injection, pore pressure injection zone, and pressure of monitoring zone above injection zone. (From Hovorka et al., 2009)

EXPERIMENTAL WORKFLOW

The first step in the experimental process was to prepare the sample and record a baseline of the mechanical properties. It was important to dry the samples before measuring their mass to calculate accurate bulk and grain densities. The core plugs were dried at 70ºC for 72 hours. The initial dimensions and mass of the core plugs were recorded to note any change in bulk properties after the injection of CO_2-rich brine.

Baseline porosity and permeability of the initial core plug were measured next. After measuring porosity and permeability, a sample was inserted into the pressure vessel where it underwent a series of loadings, reactant injections, and unloadings. Measuring the pressure dependency of P- and S- wave velocities for the dry core plug, before any injection, established a baseline for the elastic properties. Both the compressional and shear velocities of the core plug were measured as a function of confining pressure, in this case ranging from 0 to 55 MPa. Smaller pressure intervals were used at low confining pressures to map the nonlinear portion of the compaction curve. The following list is the workflow used in these experiments:

1. Load sample to 55 MPa.
2. Inject sample with carbon dioxide-rich synthetic Tuscaloosa brine to a pore pressure of 28 MPa.
3. Measure the change in length, Vp, and Vs.
4. Flush the sample with a given number of pore volumes of carbon dioxide-rich synthetic Tuscaloosa brine while maintaining a pore pressure of 28 MPa.
5. Measure change in length, Vp, and Vs.
6. Leave saturated sample in current conditions for 12 hours.
7. Measure change in length, Vp, and Vs.
8. Drain fluid and dry with gaseous helium at 150 psi for five hours. The helium pushes liquid out of the core plug.
9. Measure changes in length, Vp, and Vs while decreasing confining pressure to 20 MPa. Note that the pore pressure of the sample is zero.
10. Repeat steps 1-9 to monitor the effect on Vp and Vs while increasing injected pore volumes.

DISCUSSION

Measuring velocity at various differential pressures after injecting CO_2-rich brine may emulate changing the pore pressure. For a given pore pressure, injecting various amounts of CO_2-rich brine can enable one to determine the change in velocity of the "dry" frame due to chemical reactions. Knowing the impact of pore pressure on the elastic properties of the samples can enable one to determine the change in velocity due a change in pore pressure. However, loading and unloading a core plug in this manner may permanently deform the microstructure of the sample by damaging the quartz grains, pore filling material, or the bond between the pore filling material and the grains. Hysteresis can reveal if loading and unloading pressure compromised the microstructure of the sample. In order to understand if one of the samples underwent permanent microstructural changes caused by pressurizing and depressurizing, a "twin" sample was subjected to the same stress path as the injected sample. The "twin" sample was not injected with CO_2-rich brine. The "twin" core plug comes from the same depth as one of the injected samples and has the same porosity, permeability, and mineral composition.

REFERENCES

Darcy, H., Les Fontaines Publiques de la Ville de Dijon, Dalmont, Paris (1856).

Hovorka, S. D., T. A. Meckel, R. H. Treviño, J. P. Nicot, J. W. Choi, J. Lu, H. Zeng, K. Romanak, C. Yang, M. Kordi, and P. Wang, SECARB Phase II – Cranfield, MS: presented at the Southern States Energy Board Stakeholders' Meeting, Atlanta, Georgia, March 3, 2009. GCCC Digital Publication #09-03.

Klinkenberg, L. J.: 1941, The permeability of porous media to liquids and gases, Drilling and Production Practice, American Petroleum Inst., pp. 200–213.

Lu, J., Kharaka, Y., Thordsen, J., Horita, J., Karamalidis, A., Griffith, C., Hakala, A., Ambats, G., Cole, D., Phelps, T., Cook, P., Manning, M., and Hovorka, S., 2011, Geochemical interactions in the Lower Tuscaloosa reservoir at the Cranfield CO_2 sequestration site, Mississippi, USA, Elsevier Editorial System for Chemical Geology, in press.

Schmidt, P. S., O. Ezekoye, J. Howell, and D. Baker. 2006. Thermodynamics: An Integrated Learning System. Hoboken: John Wiley & Sons, Inc.

Chapter 4: Experimental Results

RESULTS

The results section has two subcategories, which are focused on fluid composition and sample characterization. The pH measurements and titration results are given for the fluid before and after injection into the rock samples. The samples are characterized before and after reactant injection in terms of dimension, porosity, and permeability. The samples are characterized by length, elastic wave propagation velocity, and elasticity as functions of differential pressure and injected pore volumes. The velocity is measured on dry samples. Therefore, the differential pressure is equal to the confining pressure because pore pressure is zero.

Fluid composition

The fluid composition is described in Table 4.1. The pH decreased during the injection of CO_2 and increased for some time after injection for both synthetic and in situ brine. Also, the iron (Fe^{2+}) concentration increased both in the field and experimentally due to dissolution. The concentration of the iron was greatest after the first injection and exponentially decayed with subsequent injections. Due to the large initial calcium concentration, any change in calcium concentration of the brine after injection into the sample was below the resolution of the titration technique.

	SYNTHETIC			IN SITU		
	PRE-CO2	DURING-INJECTION	POST-INJECTION	PRE-C02	DURING-INJECTION	POST-INJECTION
pH	5.78	3.4	4.78	5.7	3.5	5.2
$[Ca^{2+}]$ (mg/L)	11,422	11,422	11,422	11,500	11,500	11,500
$[Fe^{2+}]$ (mg/L)	0	0	40-80	500	500	590-670

Table 4.1: Fluid composition before, during and after CO_2 injection, of the synthetic and in-situ brine. (In situ fluid composition from Lu et al., 2011)

Sample characterization and measurements

The samples are characterized by composition before injection and geometry, porosity and permeability before and after each injection. While the samples are in the pressure vessel, length and travel times of P- and S-waves are measured. These are used to compute elastic parameters as functions of differential pressure and injected pore volumes. The samples are visually characterized by taking scanning electron microscope (SEM) images of the same location before and after injection.

Samples A and Y were injected with carbon dioxide-rich brine and subjected to loading and unloading pressure. Sample B was subjected to only pressure loading and unloading as a control.

Mineral composition

The samples are primarily sandstone with some clay minerals, such as kaolinite, chlorite and illite, in the pore space. Samples A and B have almost the same composition. Sample Y is more clay rich and less quartz rich than the samples from the 31F-2 well. Also, sample Y has slightly more anatase and halite than samples A and B.

Well	Sample	Quartz	Kaolinite	Chlorite	Illite	Halite	Anatase	Total
31F-2	A	85.16	2.88	7.62	1.48	0	2.86	100
31F-2	B (control)	86.02	2.44	7.49	1.41	0	2.64	100
31F-3	Y	74.97	4.99	15.08	0.46	1.31	3.18	99.99

Table 4.2: Mineral composition of the samples in volumetric percent. Sample Y from the F-3 observation well is more clay rich than the samples from F-2. Also, sample Y has a small percentage of halite, which is likely from the formation water or drilling fluid.

Dimensions, porosity and permeability

The changes in size, mass, density, porosity, and permeability for all three samples is summarized in table 4.3. In all of the samples, the measured length after

pressure loading was slightly shorter than prior to loading. However, the maximum change in length after unloading was 0.6 mm for sample Y. The radii of all samples recovered upon unloading are within error of the caliper. The mass of the sample after injecting carbon dioxide-rich brine was roughly equal to the mass before injection within error of the mass balance. The porosity of sample A decreased by 1.1% and sample Y decreased by 0.5% after the injection of carbon dioxide-rich brine and pressure loading. The permeability changes are larger than any other parameter. The permeability of sample A increased from 5.2 to 10.4 mD (100%) and sample Y increased from 18.0 to 44.1 mD (145%) after the injection of carbon dioxide-rich brine and pressure loading. The properties of sample B did not change within error of the instruments used for the measurements.

SAMPLE		A	B	Y
WELL		31F-2	31F-2	31F-3
DEPTH (feet)		10446.3	10446.4	10476.7
LENGTH (cm)	Before	2.75	2.99	2.81
	After	2.73 (-1%)	2.99	2.75 (-2%)
DIAMETER (cm)	Before	2.53	2.54	2.41
	After	2.53	2.53	2.38 (-1%)
MASS (g)	Before	29.06	31.59	23.59
	After	29.10	31.54	23.26 (-1%)
GRAIN DENSITY (g/cc)	Before	2.66	2.66	2.70
	After	2.65	2.66	2.72
POROSITY (%)	Before	21.3	21.4	31.6
	After	20.2	21.5	30.1
PERMEABILITY (mD)	Before	5.2	5.7	18.0
	After	10.4 (+100%)	5.12 (-1%)	44.1 (+145%)

Table 4.3: Sample nomenclature and characterization.

Length pressure curves

Change in length (ΔL) versus differential pressure is plotted in figures 4.1-4.3. Note that positive ΔL corresponds to decrease in length. The lengths of the core plugs nonlinearly decrease with increasing confining pressure for all samples, as seen in figures 4.1-4.3. The gradients of the curves decrease as differential pressure increases. The gradients become constant for differential pressures greater than 20 MPa. Also, the samples shorten with increasing injected pore volumes until a critical amount of injected pore volumes. Injecting more reactant than the critical injected pore volumes does not cause the length of the samples to decrease. Among the injected samples, sample A exhibits the least change in length compared to the pressure curve before injecting reactant. Sample Y exhibits the largest change in length with respect to injected pore volumes.

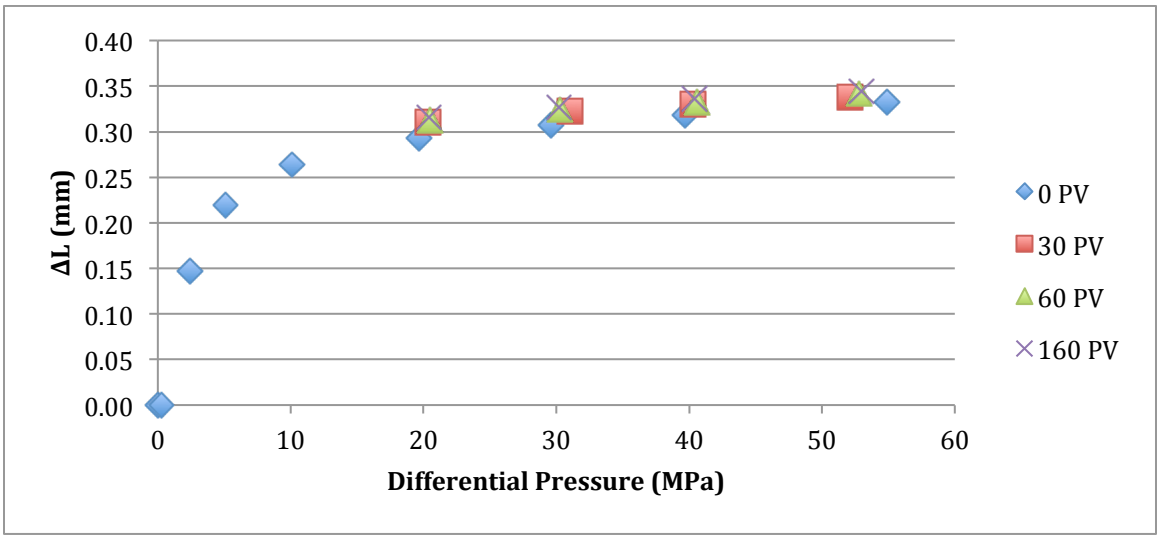

Figure 4.1: Change in length for sample A as a function of differential pressure and injected pore volumes. Note that a positive ΔL corresponds to sample shortening. ΔL nonlinearly increases with differential pressure. From 20 to 55 MPa, the change in length is linearly proportional to differential pressure. There is a slight increase in ΔL with increasing injected pore volumes. ΔL almost fully recovers injecting 160 pore volumes and loading.

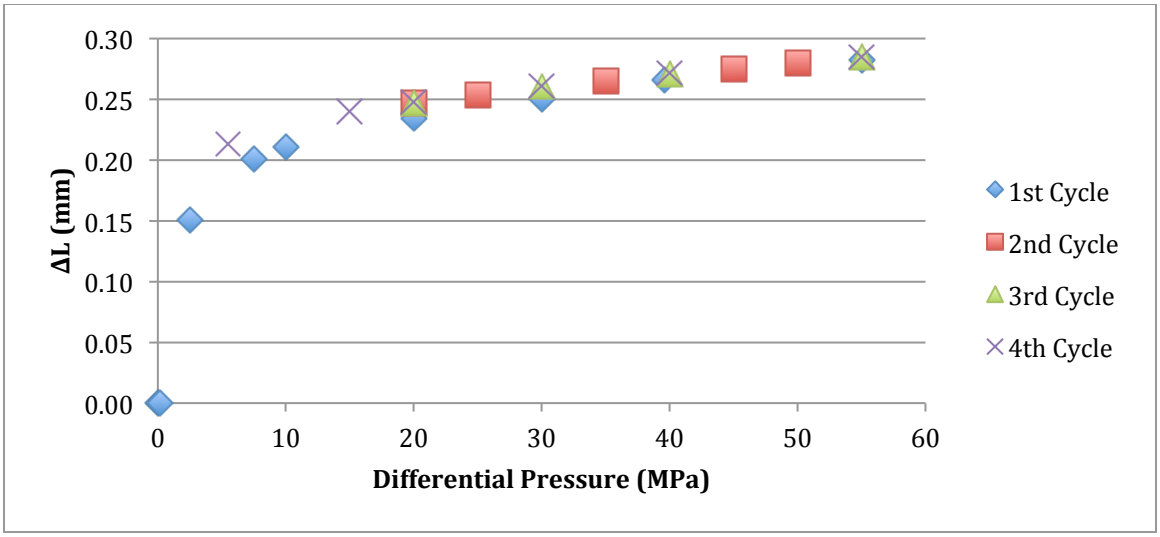

Figure 4.2: Change in length for sample B as a function of differential pressure and injected pore volumes. Note that a positive ΔL corresponds to sample shortening. ΔL nonlinearly increases with differential pressure. From 20 to 55 MPa, ΔL is linearly proportional to differential pressure. ΔL while loading is approximately the same as ΔL while unloading.

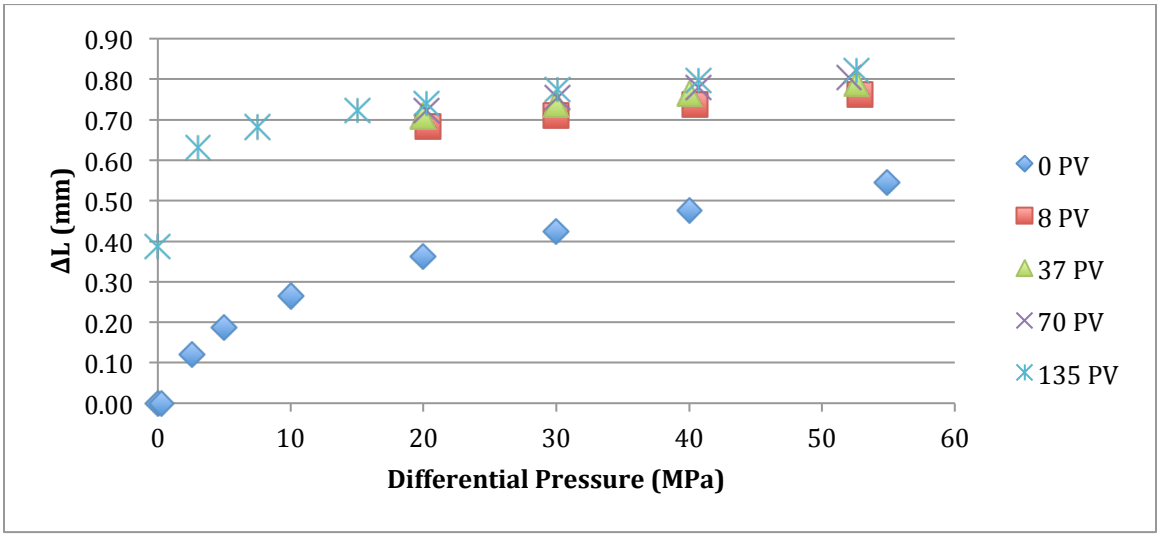

Figure 4.3: Change in length for sample Y as a function of differential pressure and injected pore volumes. Note that a positive ΔL corresponds to sample shortening. ΔL nonlinearly increases with differential pressure. From 20 to 55 MPa, ΔL is linearly proportional to differential pressure. There is a slight increase in ΔL with increasing injected pore volumes. Also, ΔL did not recover fully after injection.

Elastic wave velocity measurements

The wave propagation velocities of the core plugs nonlinearly increase with increasing differential pressure. The gradient of the velocities decrease with differential pressure. The gradients become approximately constant for Vp and Vs for differential pressures greater than 20 MPa. Also, the velocities decrease with increasing injected pore volumes. However, there is a critical amount of injected pore volumes where further injection induces negligible change in velocity. With increasing differential pressures, the difference between the baseline velocities and the velocities after injecting CO_2-rich brine increases for sample A. The differences between baseline and time-lapse velocity measurements are approximately constant at all differential pressures. Sample B does not show a change in velocity with respect to the number of times the sample was loaded and unloaded with pressure. Velocities of sample Y are more sensitive to injected pore volumes than that of sample A.

The shear wave data is similar to the primary wave data, but they have slightly more scatter than the P-wave data. Again, velocity decreases with increasing injected pore volumes. Also, the difference between baseline and time-lapse measurements is greatest at large differential pressures.

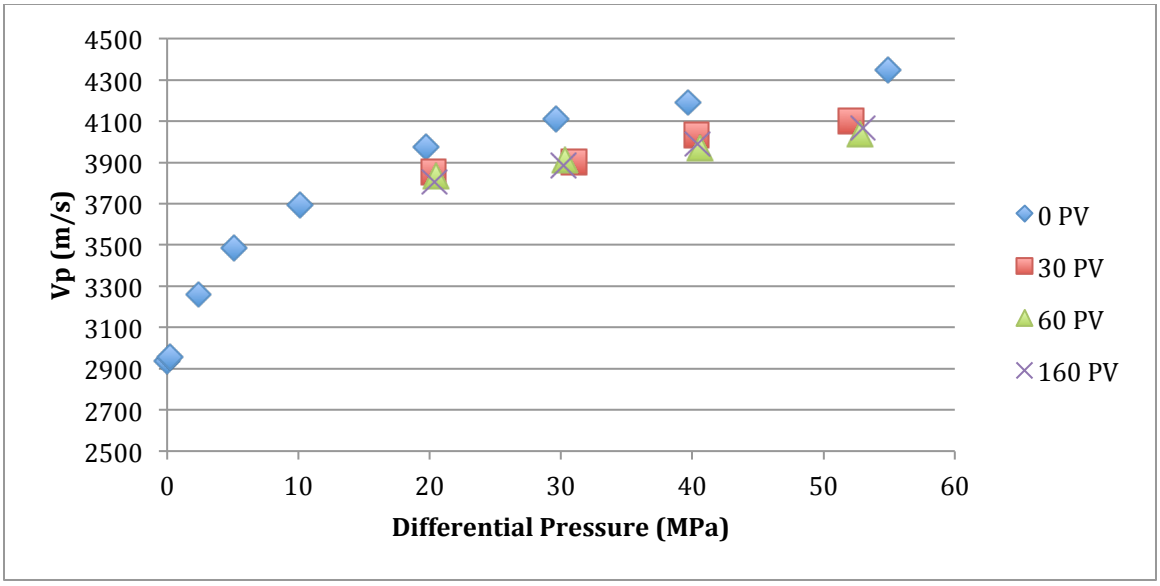

Figure 4.4: Vp versus differential pressure for sample A. Vp nonlinearly increases with differential pressure. Vp decreases with increasing injected pore volumes. The difference between velocities at 0 pore volumes and 30, 60, or 100 pore volumes increases with increasing differential pressure.

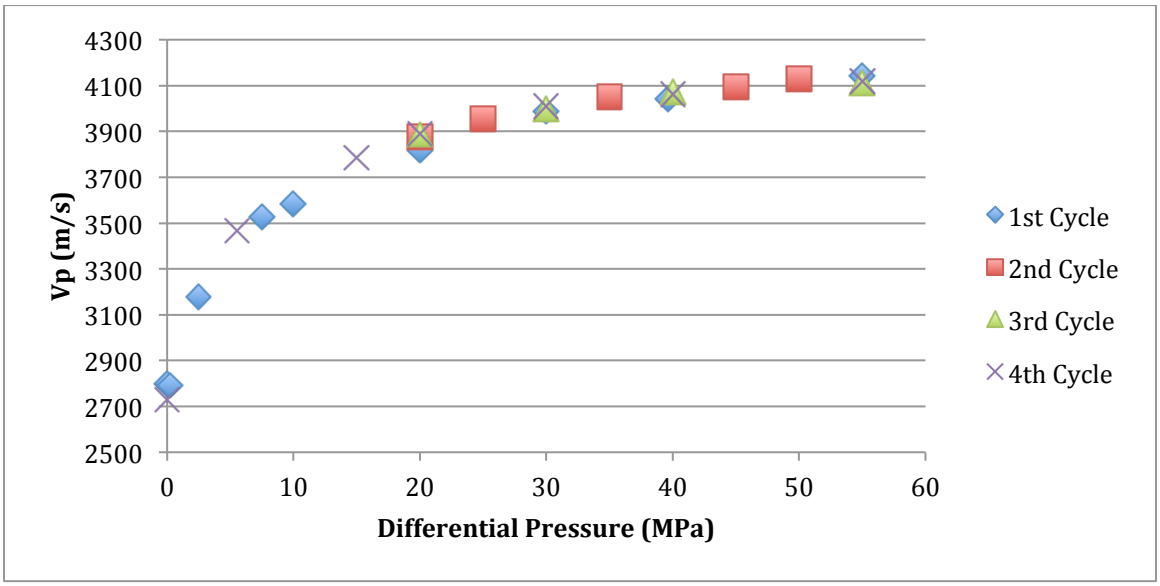

Figure 4.5: Vp versus differential pressure for sample B. Vp nonlinearly increases with increasing differential pressure. Vp for sample B did not change with regards to the number of times the sample was loaded with pressure and unloaded.

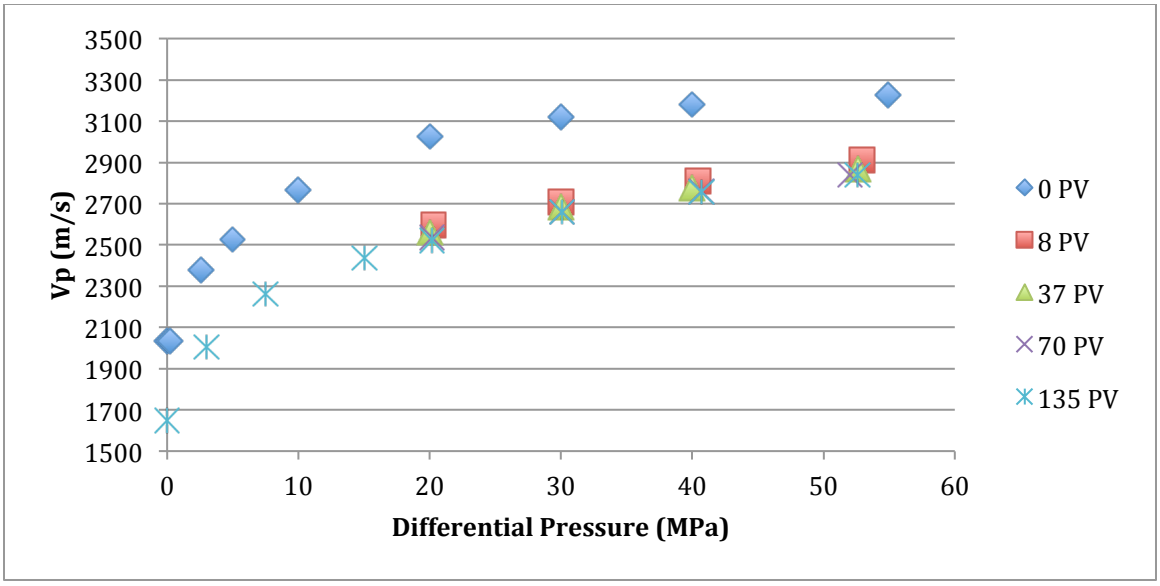

Figure 4.6: Vp versus differential pressure for sample Y. Vp nonlinearly increases with increasing differential pressure. Vp decreases with increasing injected pore volumes. The velocity drops by as much as 480 m/s after the injection of 8 pore volumes.

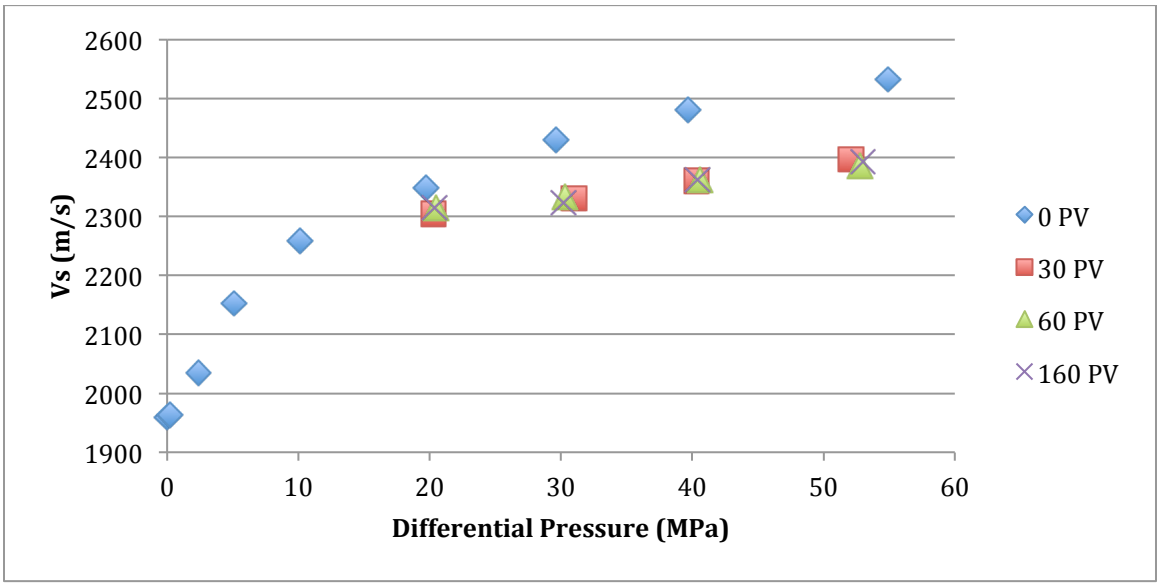

Figure 4.7: Vs versus differential pressure for sample A. Vs nonlinearly increases with differential pressure. Vs decreases with increasing injected pore volumes. The difference between velocities at 0 pore volumes and 30, 60, or 100 pore volumes increases with increasing differential pressure.

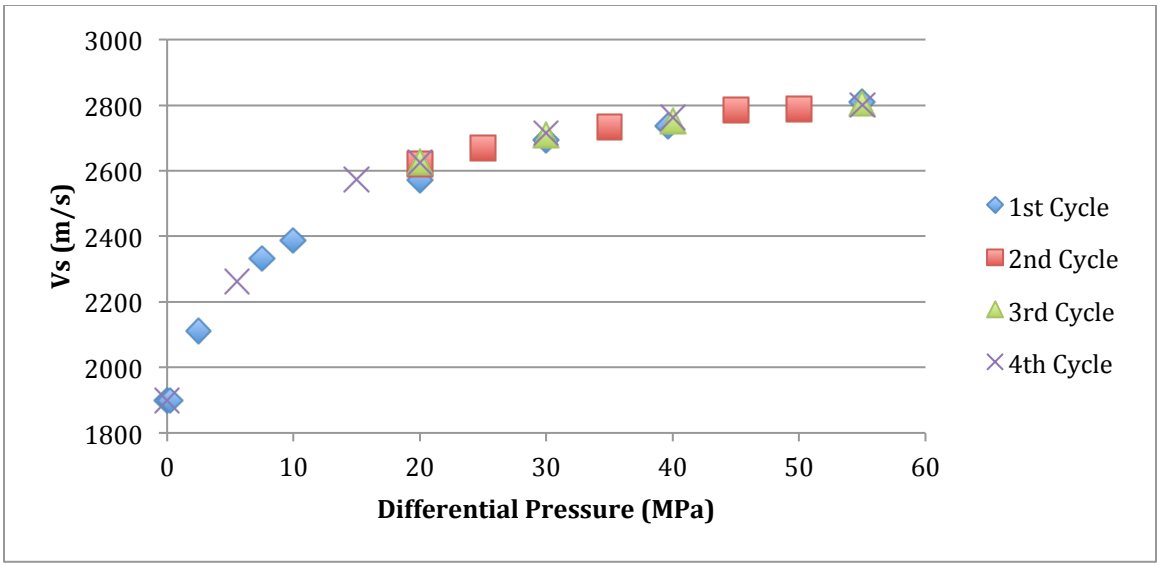

Figure 4.8: Vs versus differential pressure for sample B. Vs nonlinearly increases with increasing differential pressure. Vs for sample B did not change with regards to the number of times the sample was loaded with pressure and unloaded.

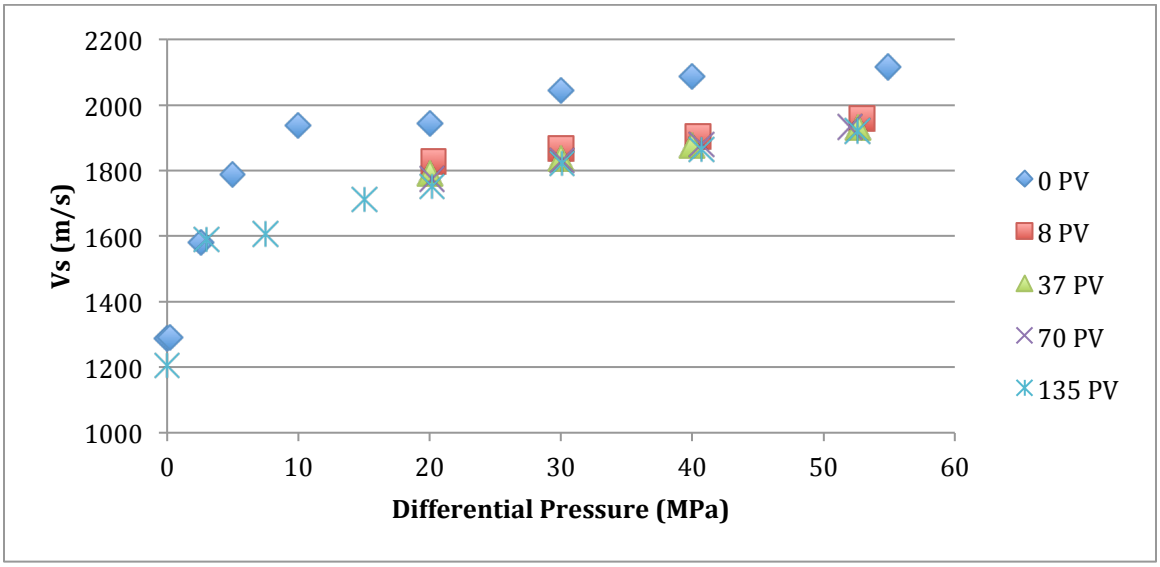

Figure 4.9: Vs versus differential pressure for sample Y. Vs nonlinearly increases with increasing differential pressure. Vs decreases with increasing injected pore volumes. The velocity drops by as much as 200 m/s after the injection of 8 pore volumes.

Elastic parameters

The elastic parameters are derived from experimentally determined elastic wave propagation velocities and bulk densities. The bulk density must be derived from the total mass and volume measured with the potentiometers. However, the potentiometers only measure the length of the sample and not the diameter. Therefore, I assume that the diameters of the samples change by the same amount as the length. The density of a sample is

4.1 $$\rho = \frac{m}{\pi(r-\Delta r)^2(l-\Delta l)},$$

where ρ is bulk density, m is mass, r and Δr are the original and change in radius of the core plug, respectively, and l and Δl are the original and change in length of the core plug, respectively. If the rock is isotropic, the previous statement is a valid assumption because elasticity does not depend on direction and the sample is subjected to a uniform pressure. Finally, the shear modulus and bulk modulus are, respectively,

4.2 $$\mu = \rho V_s^2$$

and

4.3 $$K = \rho V_P^2 - \frac{4}{3}\mu,$$

where μ is shear modulus, *Vs* is the shear wave velocity, and *Vp* is the primary wave velocity.

The following figures show how the dynamic (velocity-estimated) bulk modulus and shear modulus depend on pressure variations and injected pore volumes. The elastic parameters exponentially decay to a constant value at the critical injected pore volumes. The critical injected pore volume is found when the velocity is within 0.5% of a constant for increasing injected pore volumes. The critical injected pore volumes for the bulk and shear modulus of sample A are estimated as 80.5 and 2.2 pore volumes, respectively. In other words, the shear modulus reaches a constant value with less injected pore volumes

than the bulk modulus for sample A. However, the bulk modulus of sample Y reaches a constant value with fewer injected pore volumes than the shear modulus of sample Y. The critical injected pore volumes for the bulk and shear modulus of sample Y are estimated to be 9.6 and 19.7 pore volumes, respectively.

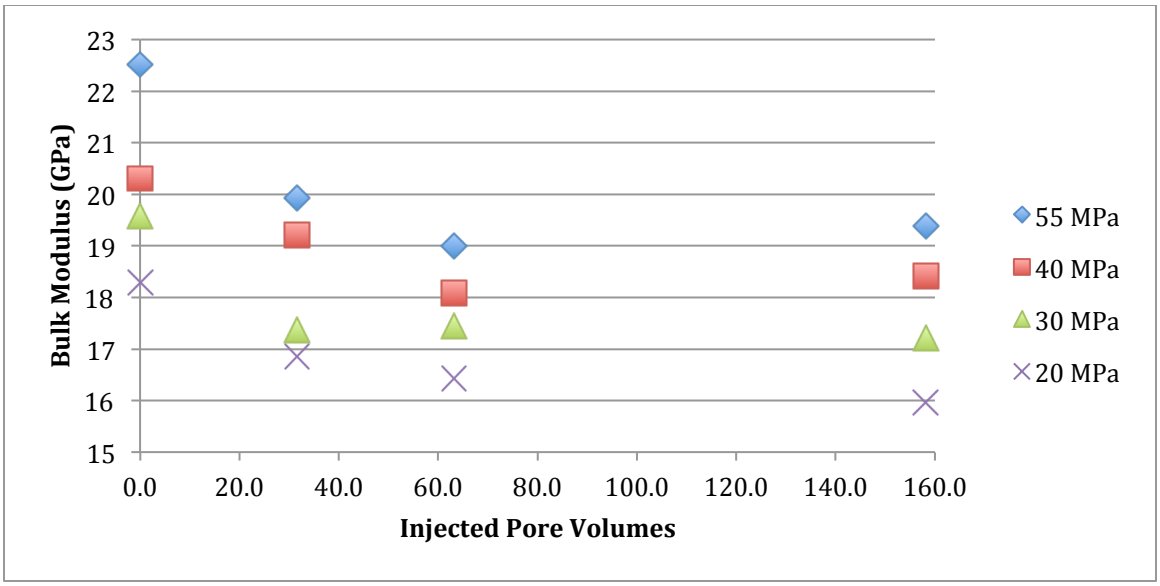

Figure 4.10: Effective bulk modulus of sample A as a function of injected pore volumes at various differential pressures. The bulk modulus for each pressure exponentially decays to a constant value, which depends on differential pressure, after the sample is injected with roughly 80.5 pore volumes.

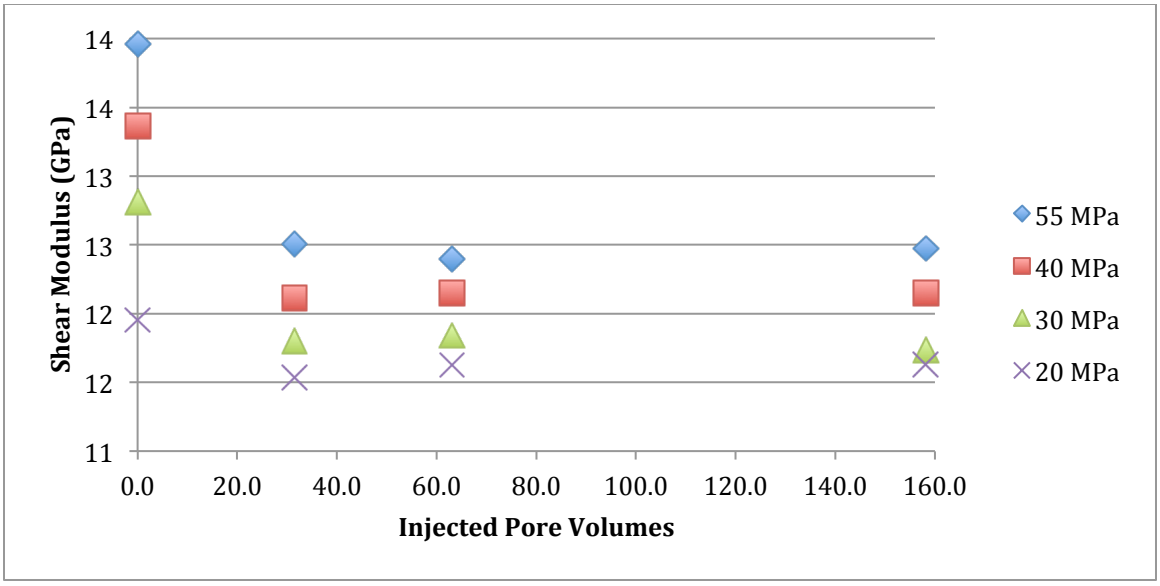

Figure 4.11: Effective shear modulus of sample A as a function of injected pore volumes at various differential pressures. The shear modulus for each pressure exponentially decays to a constant value, which depends on differential pressure, after the sample is injected with the roughly 2.2 pore volumes.

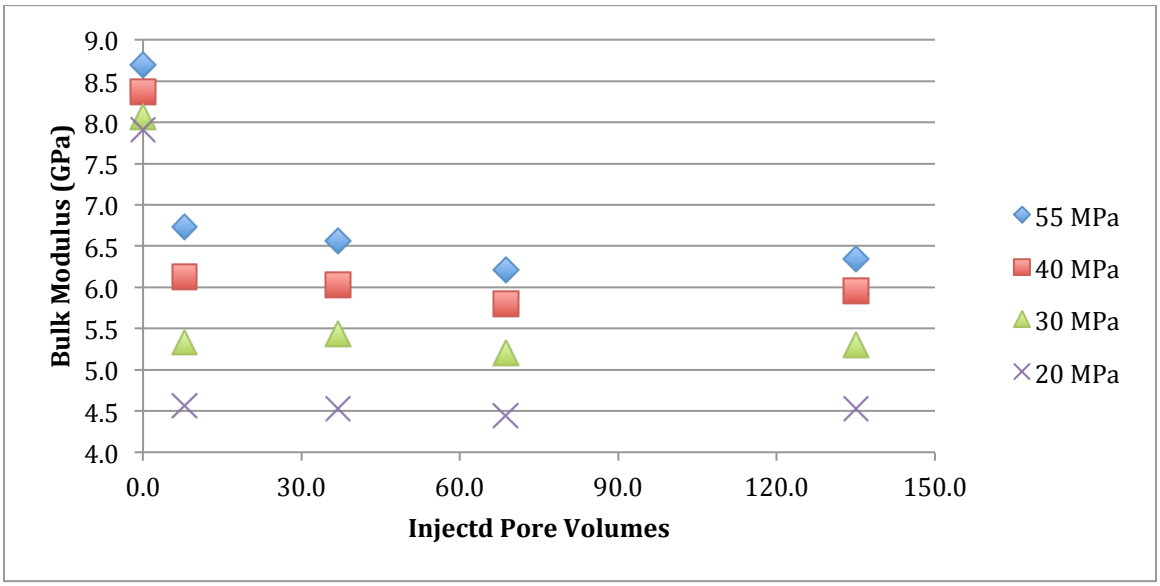

Figure 4.12: Effective bulk modulus of sample Y as a function of injected pore volumes at various differential pressures. The bulk modulus for each pressure exponentially decays to a constant value, which depends on differential pressure, after the sample is injected with roughly 9.6 pore volumes.

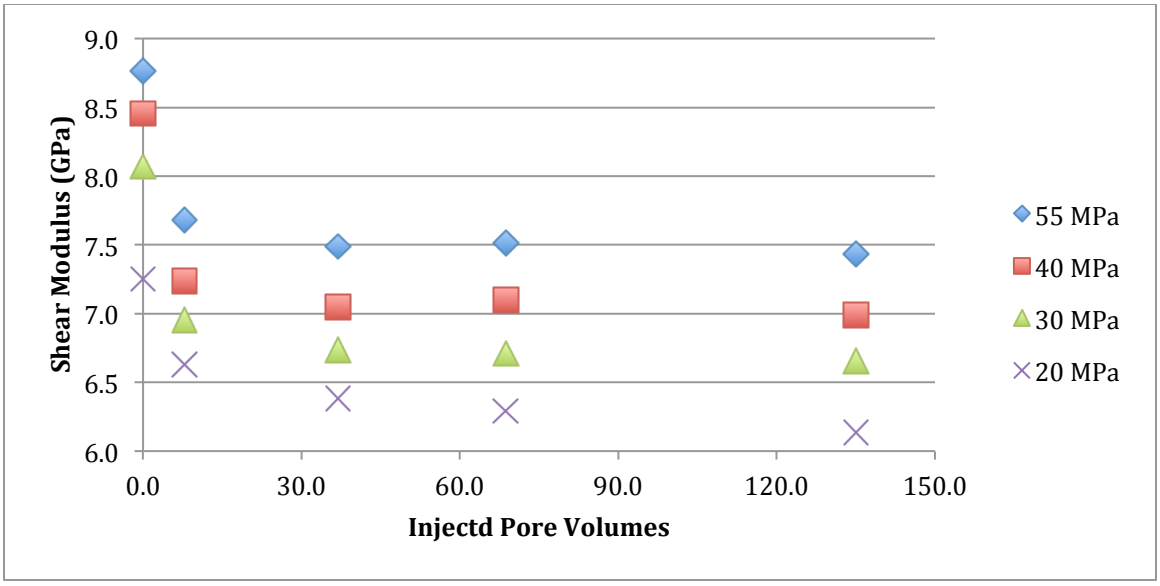

Figure 4.13: Effective shear modulus of sample Y as a function of injected pore volumes at various differential pressures. The shear modulus for each pressure exponentially decays to a constant value, which depends on differential pressure, after the sample is injected with the roughly 19.7 pore volumes.

The equations that fit the elastic parameter data as functions of injected pore volumes (V_N) at a differential pressure of 27 MPa are as follows for sample A

4.3 $$K(V_N) = 2.283e^{-0.041*V_N} + 16.713,$$

4.4 $$\mu(V_N) = 0.740e^{-1.132*V_N} + 11.722,$$

and for sample Y

4.5 $$K(V_N) = 3.036e^{-0.498*V_N} + 5.011,$$

4.6 $$\mu(V_N) = 1.198e^{-0.183*V_N} + 6.545.$$

The previous equations were determined by linearly interpolating for elastic moduli at given injected pore volumes and fit with an exponential regression. They can be substituted directly into Gassmann's fluid substitution (1951). However, pressure cannot be varied in this case. Figures 4.14-4.17 display how the variability of pressure and injected pore volumes can affect the bulk and shear moduli for sample A and Y.

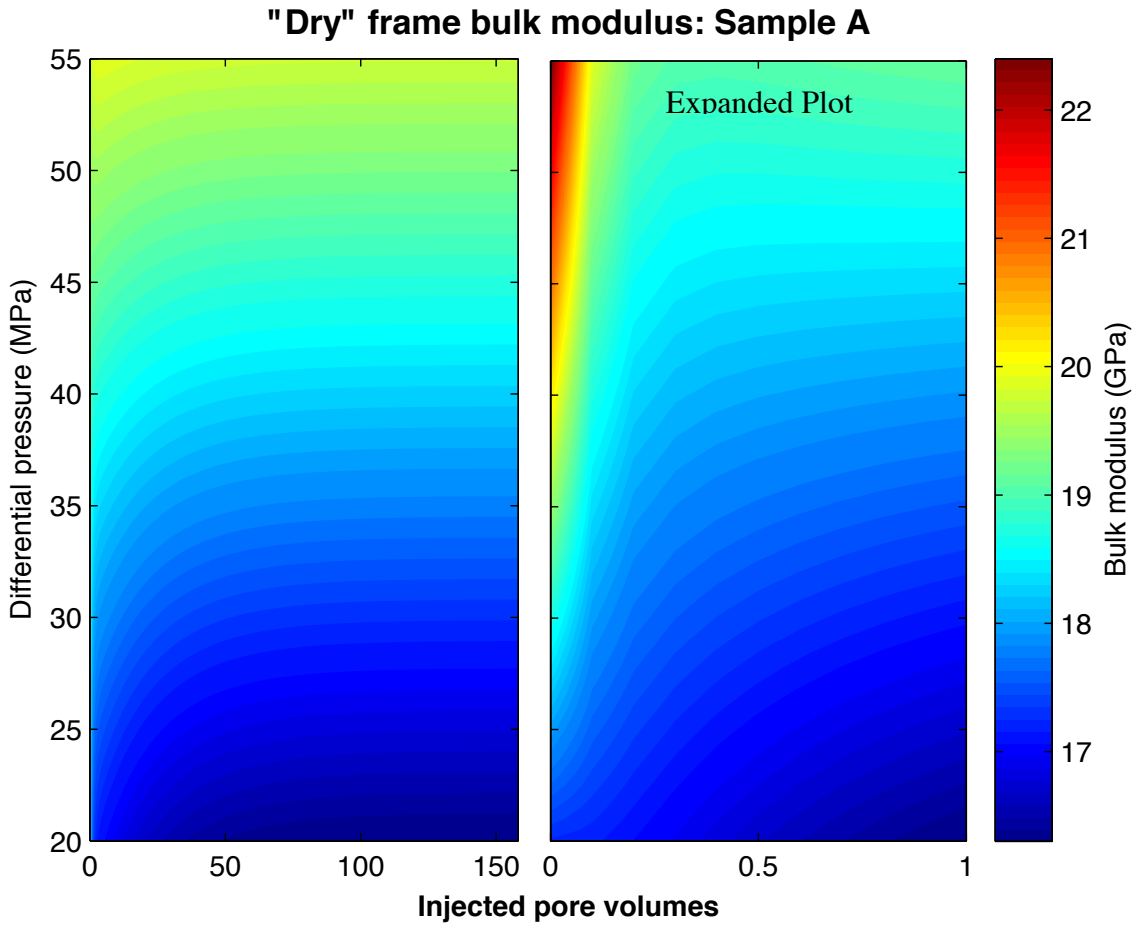

Figure 4.14: Dry-frame bulk modulus of sample A as a function of differential pressure and injected pore volumes up to 160 (left) and 1 (right). The bulk modulus increases linearly as differential pressure increases and decreases nonlinearly as injected pore volumes increases. The majority of the change occurs within the first 0.5 injected pore volumes

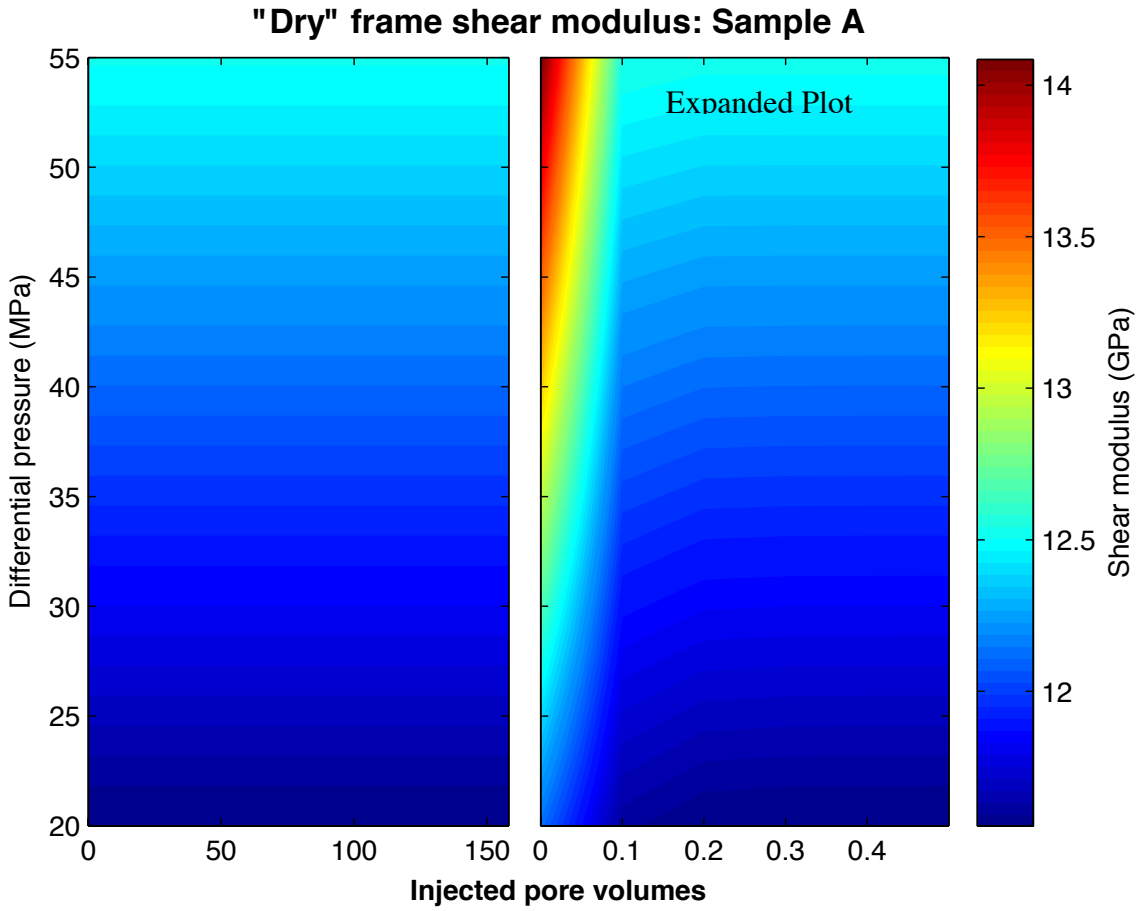

Figure 4.15: Dry-frame shear modulus of sample A as a function of differential pressure and injected pore volumes up to 160 (left) and 0.5 (right). The shear modulus increases linearly as differential pressure increases and decreases nonlinearly as injected pore volumes increases. The majority of the change occurs within the first 0.25 injected pore volumes.

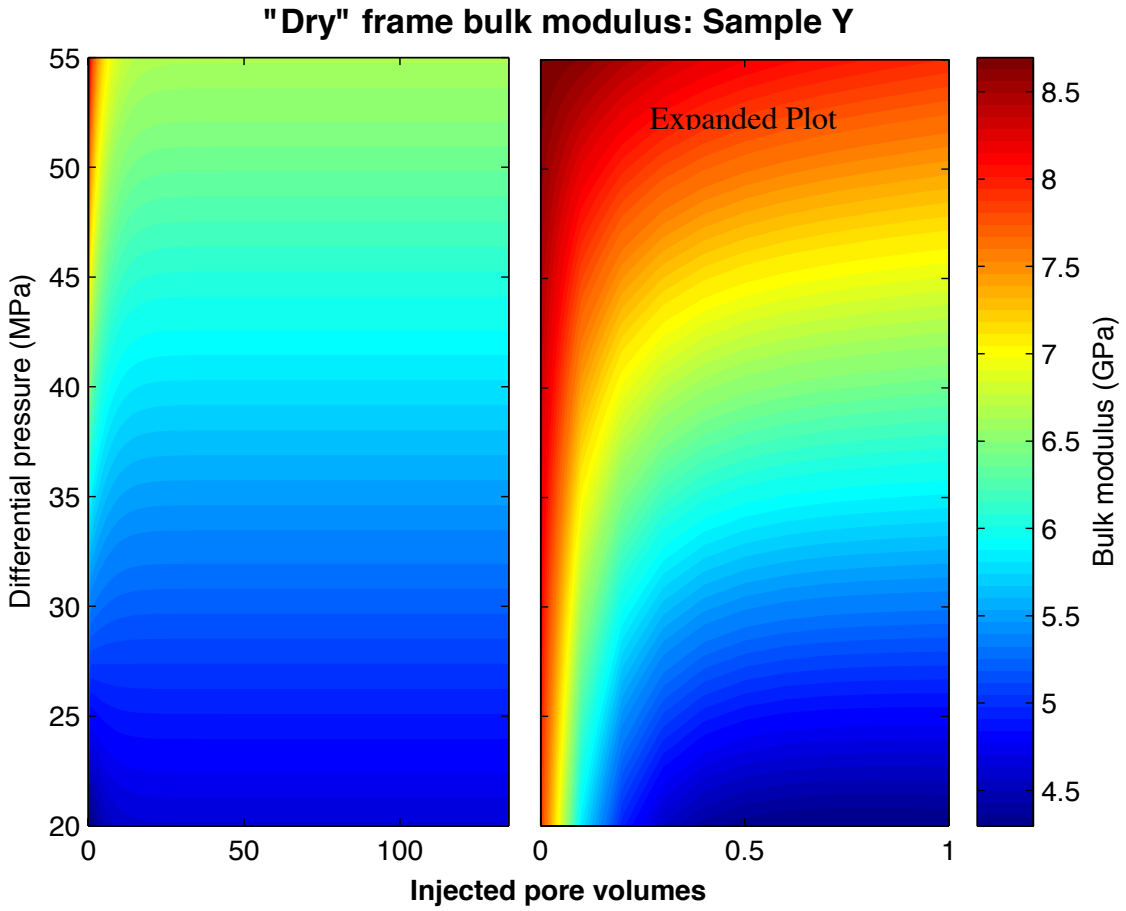

Figure 4.16: Dry-frame bulk modulus of sample Y as a function of differential pressure and injected pore volumes up to 140 (left) and 1 (right). The bulk modulus increases linearly as differential pressure increases and decreases nonlinearly as injected pore volumes increases. The majority of the change occurs within the first 0.5 injected pore volumes

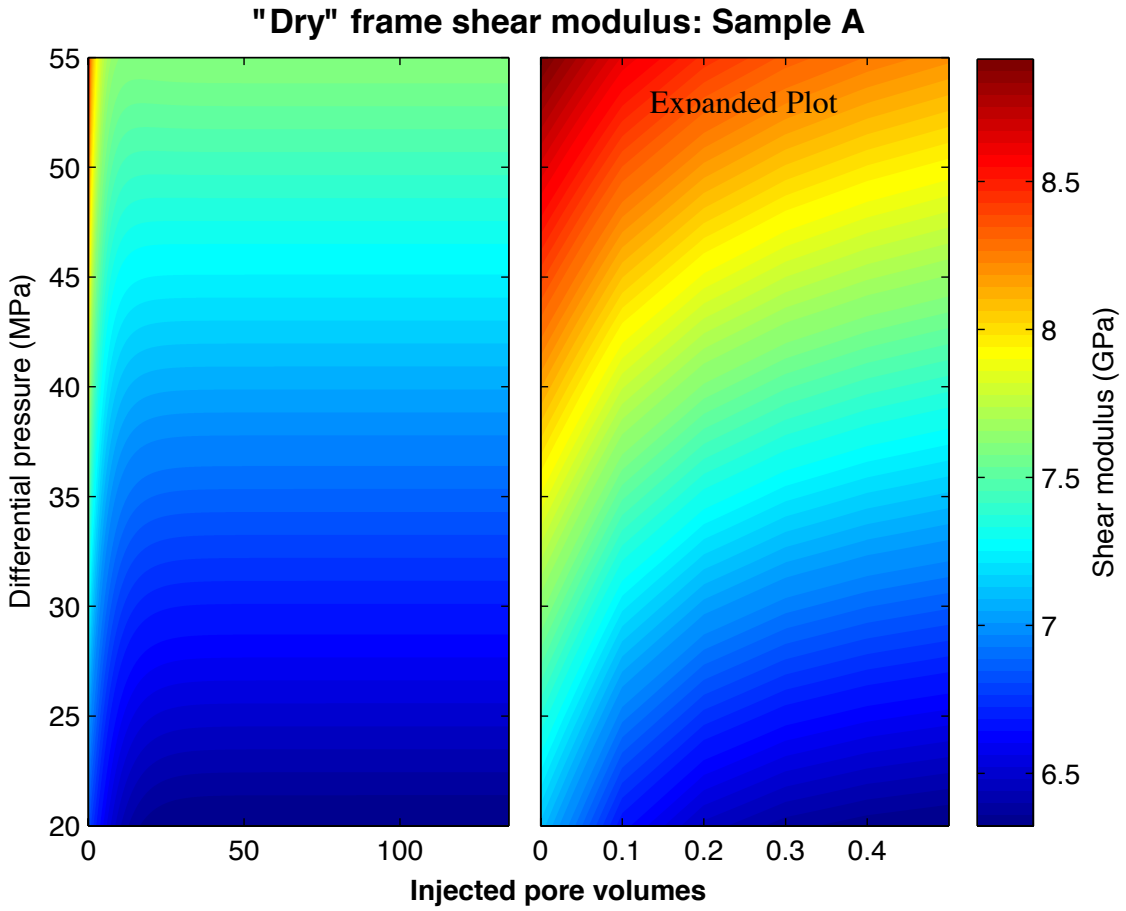

Figure 4.17: Dry-frame shear modulus of sample Y as a function of differential pressure and injected pore volumes up to 140 (left) and 0.5 (right). The shear modulus increases linearly as differential pressure increases and decreases nonlinearly as injected pore volumes increases. The majority of the change occurs within the first 0. 5 injected pore volumes

The bulk modulus and shear modulus for sample A and Y are more sensitive to injected pore volumes than differential pressure within the first 0.5 injected pore volumes. The moduli quickly reach a constant value at constant differential pressures. Any variability in elastic moduli beyond the critical injected pore volumes is purely due to pressure effects.

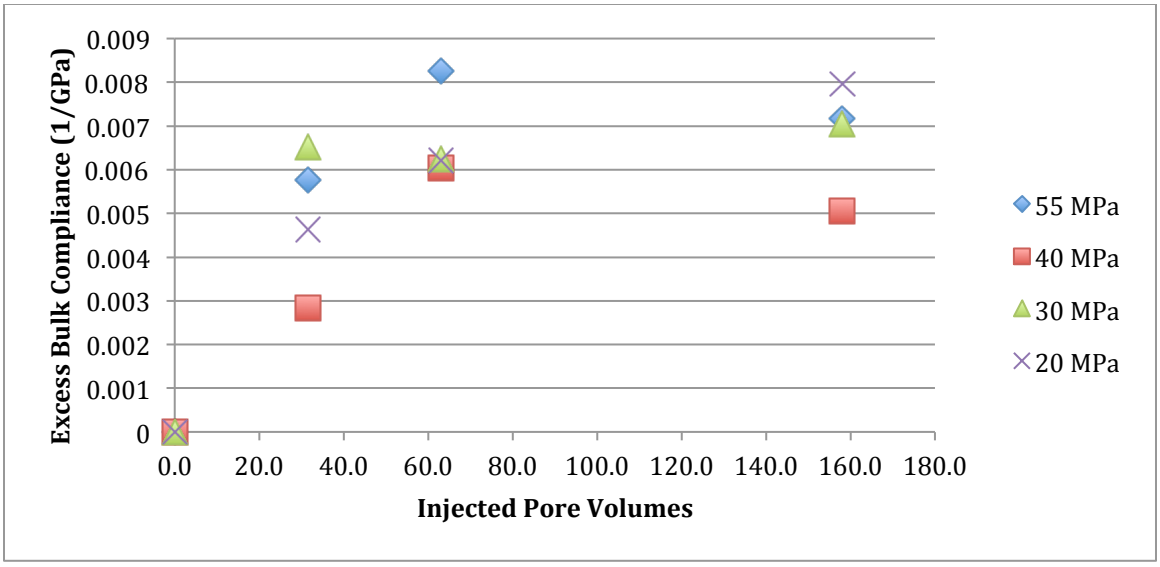

Figure 4.18: Excess bulk compliance for sample A as a function of injected pore volumes at various differential pressures. The excess bulk compliance nonlinearly increases with injected pore volumes to a constant value. The chemically induced compliance is approximately constant at a given injected pore volume for differential pressures between 20 and 55 MPa.

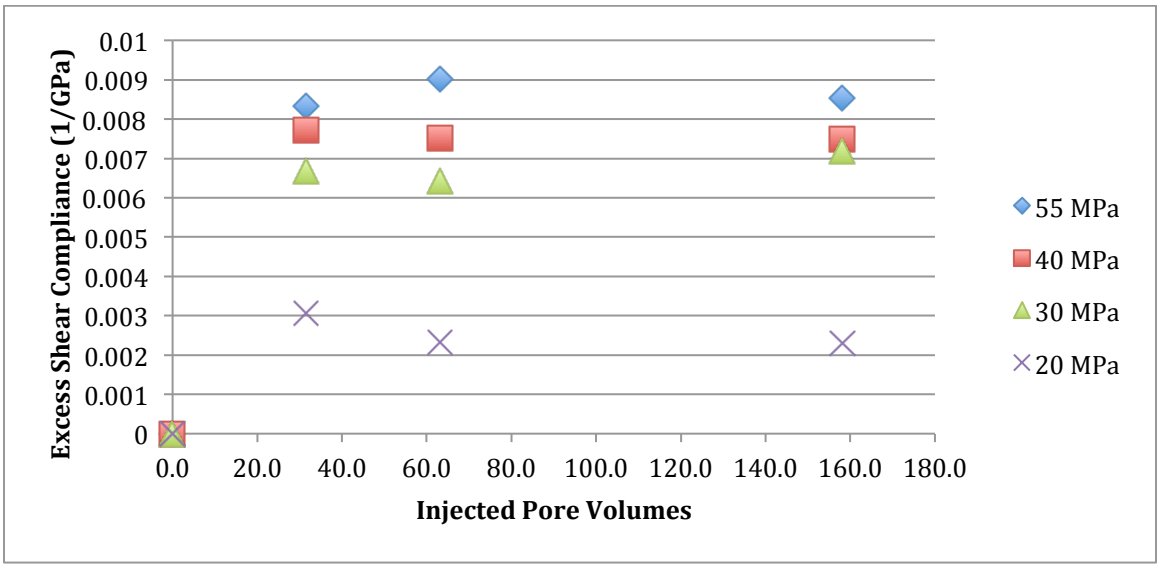

Figure 4.19: Excess shear compliance for sample A as a function of injected pore volumes at differential confining pressures. The excess shear compliance nonlinearly increases with injected pore volumes to a constant value, which depends on differential pressure. The excess shear compliance increases with differential pressure.

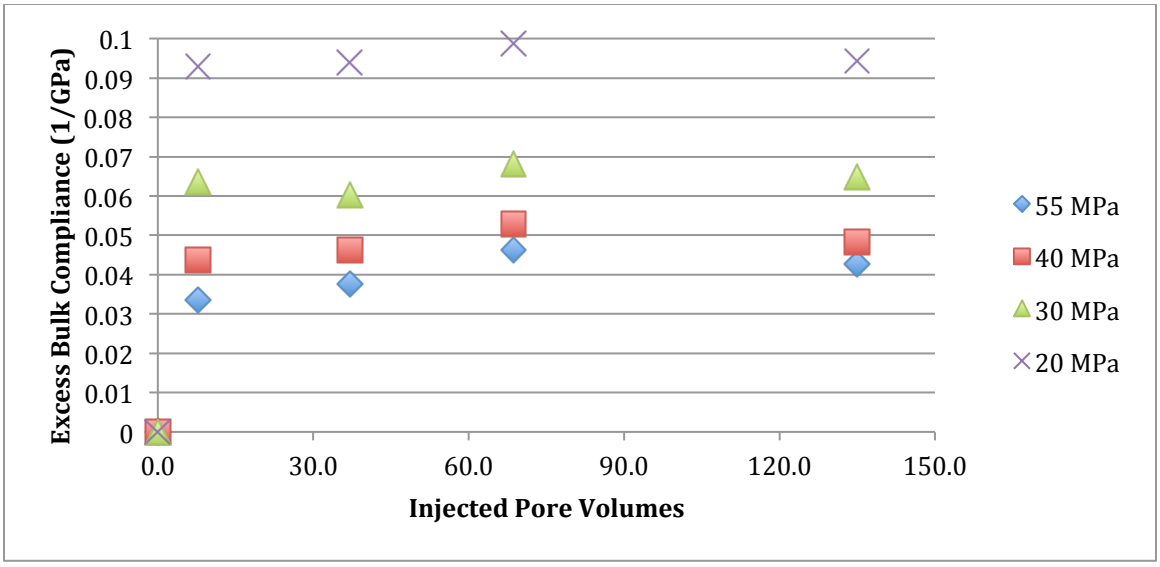

Figure 4.20: Excess bulk compliance for sample Y as a function of injected pore volumes at various differential pressures. The excess bulk modulus nonlinearly increases with injected pore volumes. Excess bulk modulus increases with decreasing differential pressure.

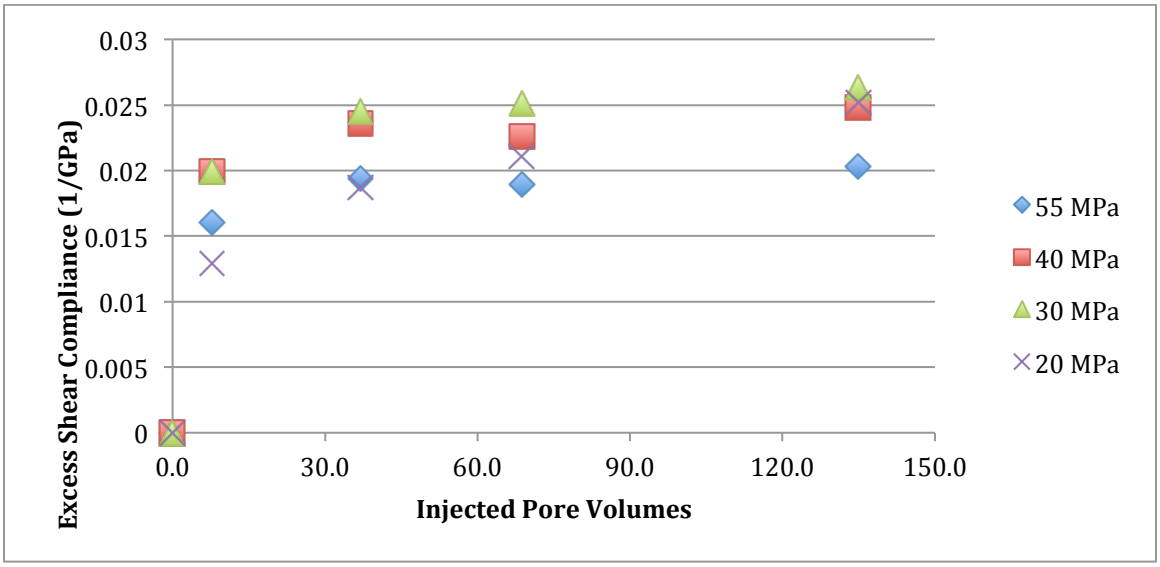

Figure 4.21: Excess shear compliance for sample Y as a function of injected pore volumes at various differential pressures. The excess shear compliance increases nonlinearly with injected pore volumes. The chemically induced shear compliance is approximately constant for a given injected pore volume at all differential pressures between 20 and 55 MPa.

The excess bulk and shear compliances, which are calculated using equations 2.2 and 2.3, respectively, increase with injected pore volumes. The gradients of the curves decrease with increasing pore volumes. The excess shear compliance is more sensitive to CO_2-rich brine injection than the bulk compliance for sample A. In other words, the excess shear compliance increases faster than the excess bulk compliance. However, the excess bulk compliance of sample Y is more sensitive to injection than the excess shear compliance.

Scanning Electron Microscope images

SEM images allow one to visually and qualitatively interpret the change in microstructure after fluid injection. Only images of the injected samples were taken. Different magnifications of the same location for each sample are displayed in the following figures. Sand grains in the figures are the largest grains. The clay mineral, chamosite $(Fe^{2+},Mg)_5Al(AlSi_3O_{10})(OH)_8$, is smaller than the quartz grains and appear as a bud of roses when looking parallel to the platelets. The other clay minerals are much smaller than the quartz grains and are seen at magnifications of 1800x. The cement, which is a mixture of the clay minerals, is lighter gray than the quartz grains.

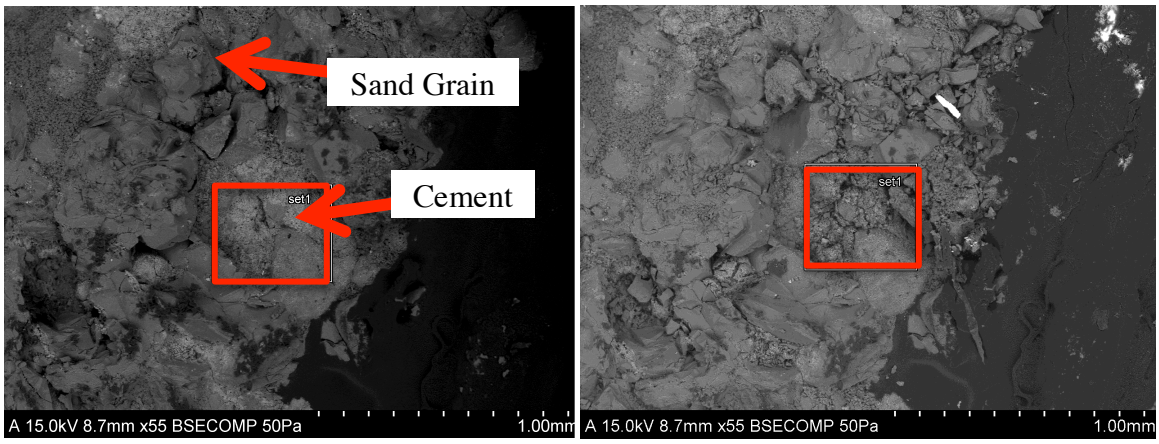

Figure 4.22: SEM image of sample A before (Left) and after (Right) reactant injections. Current magnification is 55x. The quartz grains are larger and darker in color than the clay minerals, which are not visible at this magnification, and cement. Figures 4.27-30 are zoomed in images of the location outlined by the rectangle. Overall, cracks have developed after injection.

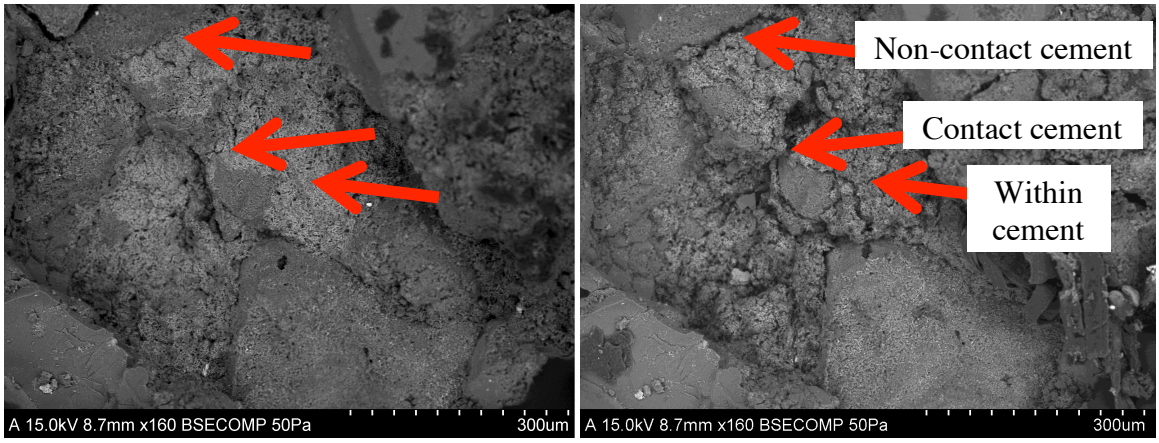

Figure 4.23: SEM image of sample A before (Left) and after (Right) reactant injections. Current magnification is 160x. Cracks within the cement, contact cement and non-contact cement are visible after injection.

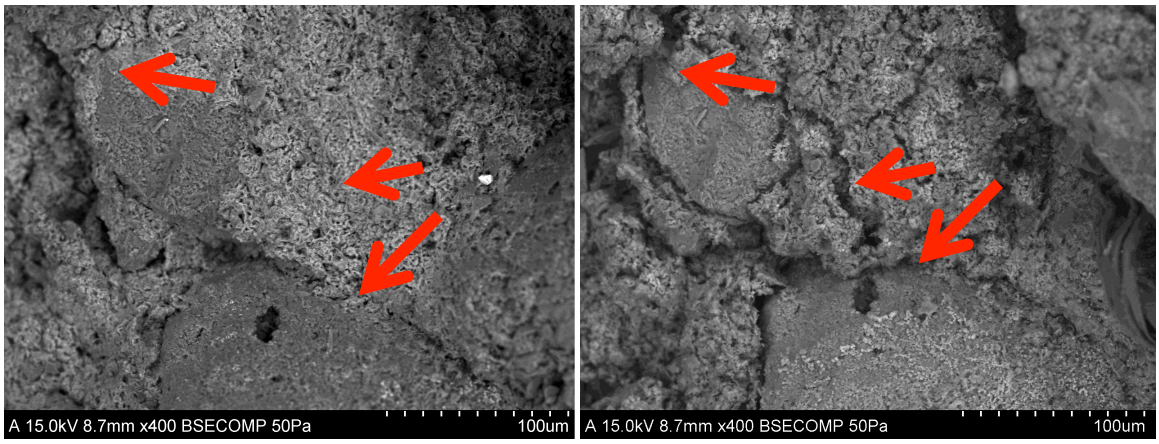

Figure 4.24: SEM image of sample A before (Left) and after (Right) reactant injections. Current magnification is 400x. Cracks within the cement, contact cement and non-contact cement are visible after injection.

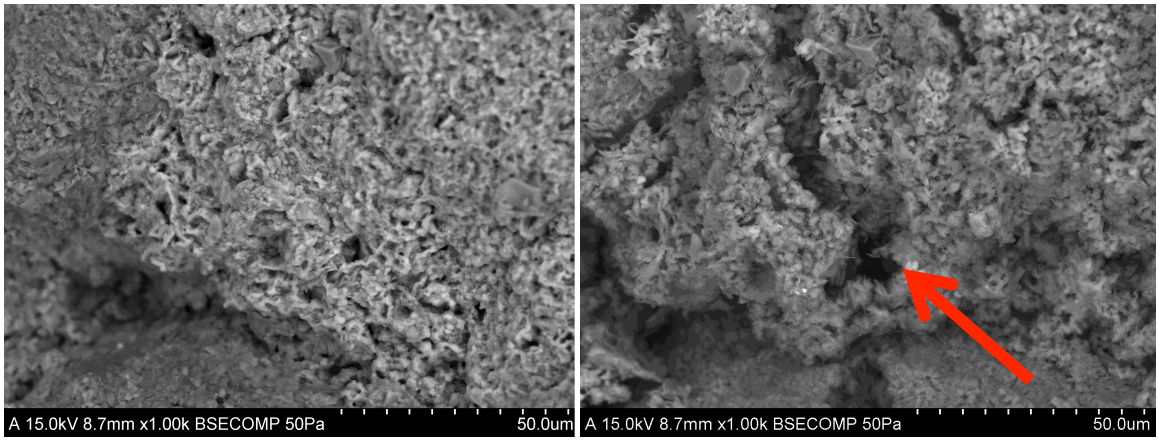

Figure 4.25: SEM image of sample A before (Left) and after (Right) reactant injections. Current magnification is 1000x. A zoomed in image of the relatively large microcrack, compared to the other induced cracking, within the cement.

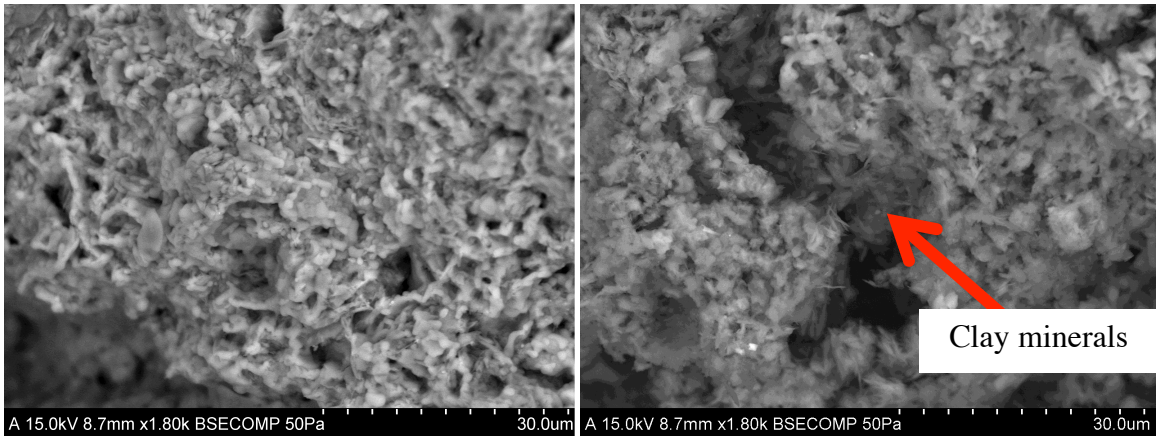

Figure 4.26: SEM image of sample A before (Left) and after (Right) reactant injections. Current magnification is 1800x. This zoomed in image of the relatively large microcrack reveals the presence of clay minerals along the walls of the microcrack, which are not clear in the image before injection. The clay minerals are thin and hair-like.

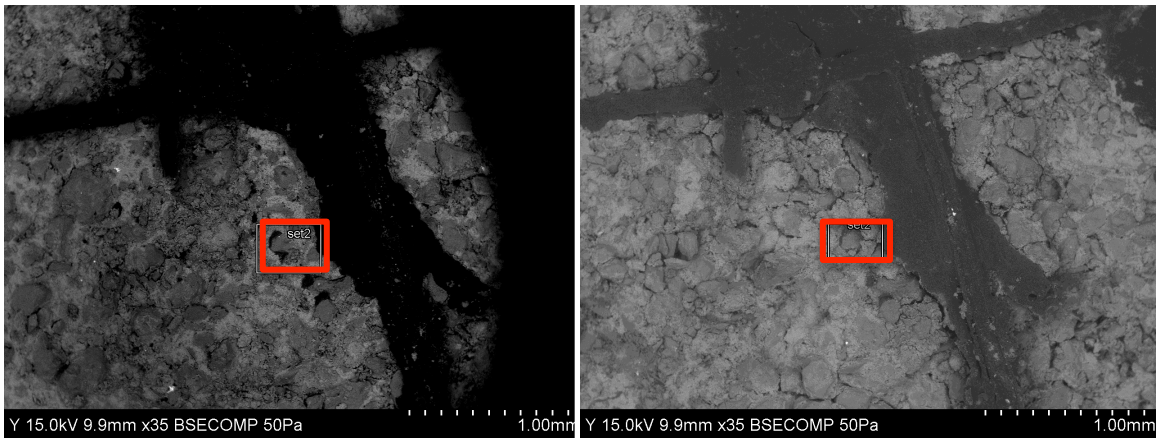

Figure 4.27: SEM image of sample Y before (Left) and after (Right) reactant injections. Current magnification is 35x. The quartz grains are larger and darker in color than the clay minerals and cement. Figures 4.32-35 are zoomed in images of the location outlined by the rectangle. Overall, cracks have developed after injection.

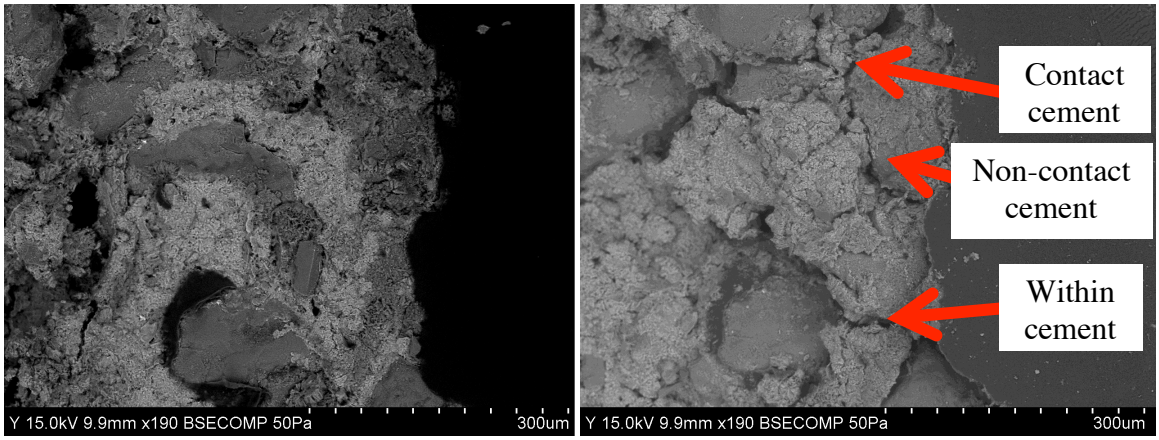

Figure 4.28: SEM image of sample Y before (Left) and after (Right) reactant injections. Current magnification is 190x. Cracks in the pseudo matrix and around the sand grains are visible.

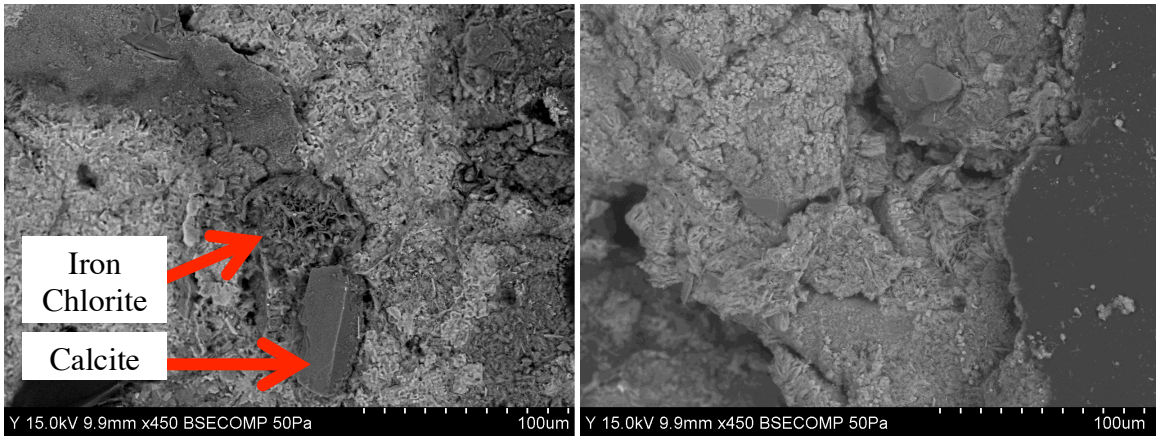

Figure 4.29: SEM image of sample Y before (Left) and after (Right) reactant injections. Current magnification is 450x. Iron chlorite and calcite can be seen in the image taken before injection on the left. The iron chlorite appears missing or structurally altered and the calcite is missing from the image taken after injection on the right.

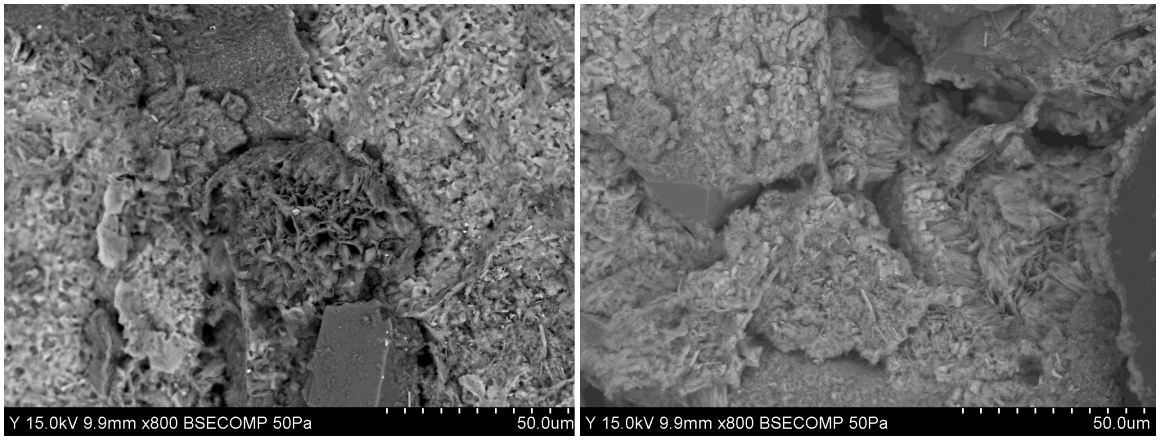

Figure 4.30: SEM image of sample Y before (Left) and after (Right) reactant injections. Current magnification is 800x.

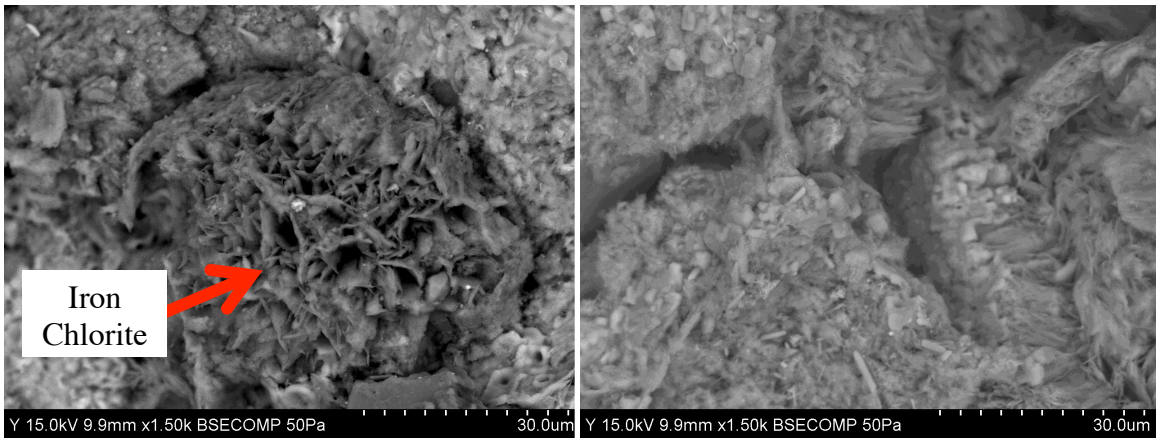

Figure 4.31: SEM image of sample Y before (Left) and after (Right) reactant injections. Current magnification is 1500x. The bud of iron chlorite is missing or altered from the image taken after injection. Also, the microcracks have become relatively larger after injection.

For samples A and Y, it appears that secondary porosity is enhanced by flowing CO_2-rich brine through the core plugs. The secondary porosity tends to be crack-like and have low aspect ratios. Also, it appears that separation has grown between the pseudo matrix, which is the clay minerals and cement, and the quartz grains. Before injection,

the samples appeared tightly cemented. After injection, the samples appeared loosely cemented. Also, the number of exposed quartz grains increased after reactant injection, which appeared to be buried under the pseudo matrix prior to injection.

CONCLUSION

Injection of carbon dioxide-rich brine causes an exponential decrease in the elastic parameters of the core samples with respect to injected pore volumes. The sample is characterized based on dimensions, porosity, permeability, mineral composition, elastic wave velocities and SEM images to understand the cause of the change in elasticity. In samples A and Y, the dimensions, porosity, and permeability hardly changed after reactant injection. However, the pressure-dependent velocity data implies that changes have occurred on the microstructural scale. Were these changes caused by hysteresis due to loading and unloading pressure? Sample B, a "twin" (control sample) of specimen A, was subjected to the same stress path without injecting reactant to monitor hysteresis. However, Vp, Vs, and ΔL followed the same trends while loading and unloading indicating that sample B did not experience hysteresis. Therefore, I conclude that changes in the microstructure of sample A are not caused by loading and unloading the sample. SEM images were taken before and after the samples were injected with reactant. Secondary porosity and microcracks, which can be seen at the lowest magnification of 55x, have increased after reactant injection, which are the likely cause for the excess compliance in the core plugs. The microcracks developed in both contact and non-contact cement at grain boundaries and on grains, respectively. It is unclear which minerals are missing through the SEM images, but it is apparent that the microstructure has changed. Are the microcracks induced by dissolution or mechanically

by injecting fluid at high pressure? The fluid composition before, during and after CO_2 injection into the brine is used to understand which minerals have dissolved.

The original composition of the synthetic brine approximately matched the composition of the in-situ brine prior to the injection of CO_2. Overall, it is important to match the water conditions because the presence of ions and pH can change the reactivity of the water with the rock. For example, the pre-injection pH and calcium concentration were 5.7 and nearly 11,500 mg/L for both synthetic and in-situ brines. The iron concentration of the synthetic brine and in-situ brine were 0 mg/L and 500 mg/L, respectively. During the injection of CO_2, the pH of the synthetic brine and in-situ brine dropped to 3.4 and 3.5-4.0, respectively. After injection, the iron concentration increased by 40-80 mg/L in the experiments and 90-170 mg/L in the field. Also, the pH of the synthetic brine and in-situ brine increased to 4.8 and 5.2, respectively, some time after the injection of CO_2 (Lu et al., 2011). Titration yields only the concentrations of various cations and anions; it does not measure the concentrations of minerals that may have been dislodged. Therefore, I conclude that the microcracks were induced by dissolution. Minerals may have been dislodged, but there is no evidence that dislodging occurred. The increase in iron concentration is likely due to the dissolution of iron hydroxide and not other iron bearing minerals (Lu et al., 2011).

Injecting carbon dioxide in the field increases the pore pressure and decreases the differential pressure of the reservoir, which can change the elasticity of the reservoir. At specific differential pressure and injected pore volumes of reactant, elastic wave velocities can indicate the effects of pressure variations and chemical reactions on the elasticity of the core plugs. It was found that reducing the differential pressure on the core plug from 35 MPa to 27 MPa decreased Vp and Vs for sample A by 60 m/s (-1.9%) and 20 m/s (-1.6%), respectively. For sample Y, Vp and Vs decreased by 45 m/s (-1%)

and 40 m/s (-1.9%), respectively. However, the Vp and Vs of sample A, for a differential pressure of 27 MPa, decreased by 165 m/s (-4%) and 80 m/s (-3%) after injecting 32 pore volumes. At a differential pressure of 27 MPa, the Vp and Vs of sample Y decreased by 410 m/s (-13.5%) and 150 m/s (-7.5%), respectively, after injecting 8 pore volumes. Based on the differences in velocities before and after injection, the velocities depend more on the amount of injected reactant than differential pressure. The core plugs were injected with up to 150 pore volumes to observe the critical injected pore volumes.

The error of the Vp and Vs measurements are roughly ±1% and ±2%, respectively. Therefore, the absolute error is velocity dependent. Also, there is more error picking the first arrival of the S-wave, because the waveform is not as clear as the P-wave. Various factors may affect the certainty of the velocity measurements. First, human error while performing the experiments or taking readings is always possible. For example, picking the incorrect P- or S-wave arrival will result in incorrect calculated velocities. In regards to the equipment, a poor coupling between the source and receiver pressure transducers with the core plug could yield a poor electric signal on the receiving end. A weak electrical signal will yield a poor waveform. Picking the first arrival on a poor waveform could change the velocity ±2% or more.

Injecting carbon dioxide-rich brine increased the permeability of the samples and did not change the porosity of the samples. The permeability of sample A increased from 5.2 mD to 10.4 mD (100%). The permeability of sample Y increased from 18.0 mD to 44.1 mD (145%). Even though the percentage increase of the permeability is significant, the absolute increase of permeability is low.

REFERENCE

Gassmann, F., 1951, Über die Elastizität poröser Medien. *Vierteljahrsschrift der Naturforschende Gesellschaft Zürich*, **96**, pages 1-23.

Lu, J., Kharaka, Y., Thordsen, J., Horita, J., Karamalidis, A., Griffith, C., Hakala, A., Ambats, G., Cole, D., Phelps, T., Cook, P., Manning, M., and Hovorka, S., 2011, Geochemical interactions in the Lower Tuscaloosa reservoir at the Cranfield CO_2 sequestration site, Mississippi, USA, Elsevier Editorial System for Chemical Geology, in press.

Chapter 5: Seismic Implications

In this chapter, I simulate the reflection seismic response of injecting carbon dioxide into a simplified reservoir model based on the results described in chapter 4. The chapter is composed of reservoir modeling pre- and post-CO_2 injection, and simulation of seismic response of post-stack seismic data and pre-stack amplitude variation with angle of incidence (AVA).

MODEL BUILDING

The geological model, based on the structural interpretation of the field, consists of an anticline with a sandstone reservoir and a shale seal. There are two versions of this reservoir model: pre- and post-CO_2 injection. Both the sandstone before injection and shale are homogeneous and isotropic. The sandstone after injection is heterogeneous due to the distribution of the CO_2 saturant and dissolution of iron bearing minerals. The shale (seal) properties are constant in the two models. The seismic properties, which are Vp, Vs and density, of the shale sequence are estimated using average values from the well log in Figure 5.1. The average Vp, Vs, and density of the shale are 4323 m/s, 2284 m/s, and 2.5 g/cc respectively. The seismic properties of the sandstone reservoir are estimated from the values obtained from experimental data for sample A and the chemical fluid substitution calculations. The reservoir is saturated with brine prior to injection (Figure 5.2). After injection, the CO_2 plume in the reservoir is uniformly saturated with 30% free-phase carbon dioxide with varying injected pore volumes as a function of lateral distance from the injection well (Figure 5.3). Also, the differential pressure of the reservoir decreased from 35 MPa, pre-CO_2 injection, to 27 MPa, post-CO_2 injection. Acoustic impedance models are generated to create post-stack simulated traces.

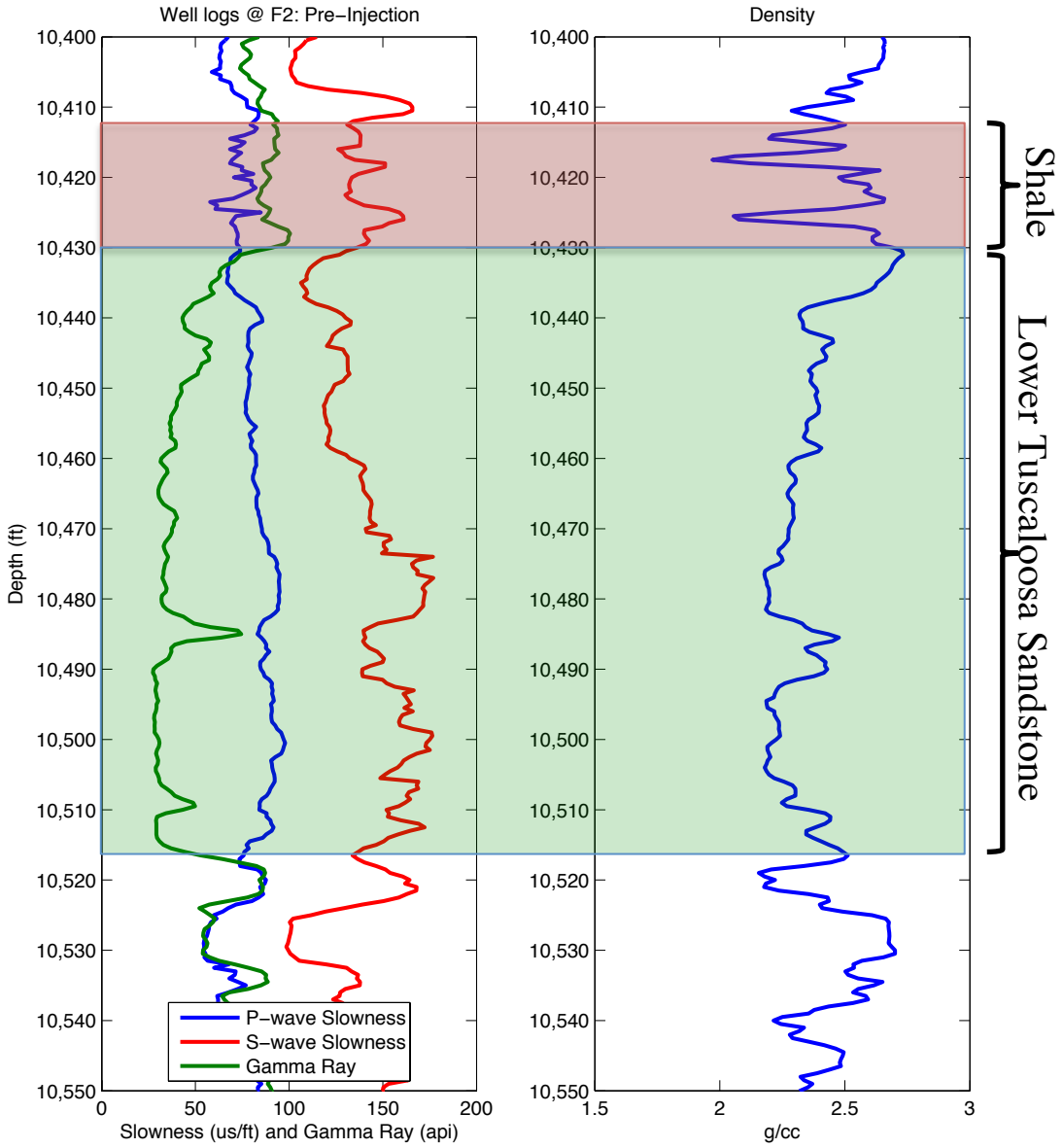

Figure 5.1: Well logs from which seismic properties of the shale seal were extracted. The shale sequence is highlighted by the red rectangle between 10,410 and 10,430 feet depth. The reservoir interval is 10,430 to 10,515 feet deep and highlighted by the green rectangle. The sample A core plug comes from a depth of 10,446.3 feet.

Pre-injection model

Prior to injection, the reservoir is entirely filled with brine. The elastic properties of the "dry" frame are derived from the baseline experimental results at a differential pressure of 34.2 MPa. The bulk modulus of the "dry" frame is 19 GPa, and the shear modulus is 12.5 GPa. The bulk modulus and density of brine are 2.38 GPa and 1.089 g/cm^3 (Mavko et al., 2009). Using Gassmann's fluid substitution equation (1951), the effective bulk and shear moduli of the brine-saturated reservoir are 21.75 GPa and 12.5 GPa, respectively. The pre-injection Vp, Vs and density of the reservoir are 4081 m/s, 2328 m/s, and 2.3 g/cc, consistent with the pre-injection well logs (Figure 5.1).

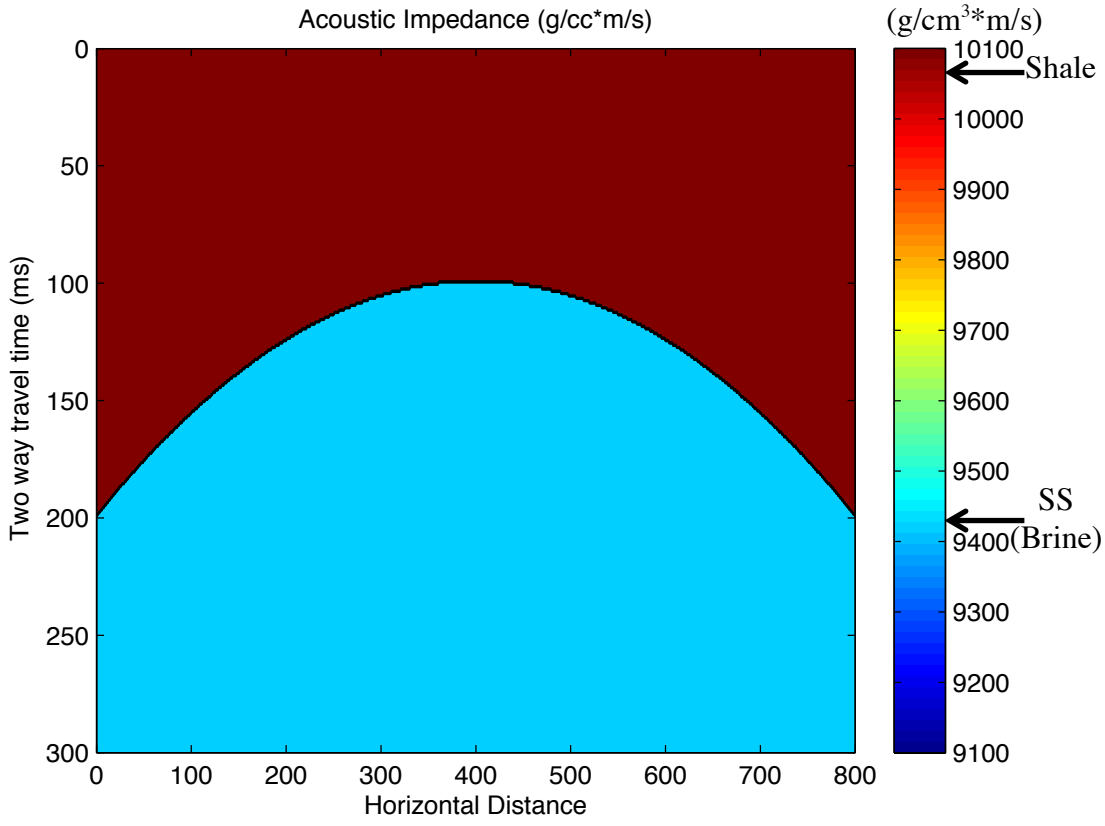

Figure 5.2: Pre-injection acoustic impedance model. The acoustic impedance of the brine-saturated sandstone (SS Brine) is less than that of the shale.

Post-injection model

The flow path of injected carbon dioxide is simulated as a plume that expands upwards and laterally due to the lower density of supercritical CO_2 compared to brine (Vilarrasa et al., 2010). The shape of the assumed plume is arbitrary. The plume is uniformly saturated with 30% free-phase, supercritical CO_2. Also, injected pore volumes vary laterally, from 100 pore volumes at the well to 0 pore volumes at the flank of the plume, to simulate the effects of varying chemical reactions.

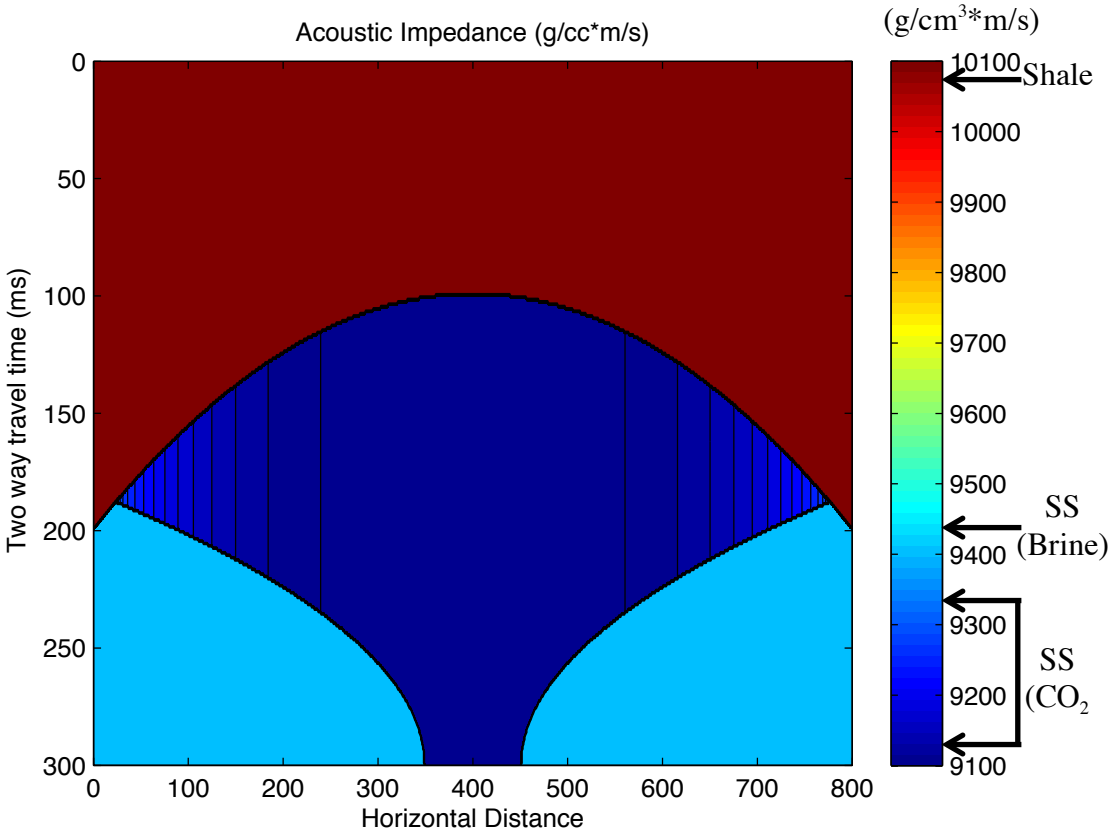

Figure 5.3: Post-injection acoustic impedance model. The injected pore volumes of reactant are varied from 100 pore volumes at the center of the plume to 0 at the edge of the plume. The free-phase, supercritical CO_2 saturation is 30% (S_W=70%) in the plume. The acoustic impedance of the CO_2 plume (SS CO_2), which is less than that of the brine-saturated sandstone, increases from the center to the flank. The acoustic impedance of the brine-saturated sandstone (SS Brine) is less than that of the shale.

POST-STACK SEISMIC MODELING

The post-stack simulated (synthetic) seismograms were created using the convolutional model (Stein and Wysession, 2003), which states that the seismic trace, S(t), is the convolution of reflectivity series, R(t), with the wavelet, W(t),

5.1 $$S(t) = R(t) * W(t).$$

The reflectivity at normal incidence is

5.1 $$R(t) = \frac{\rho(t+1)V_P(t+1) - \rho(t)V_P(t)}{\rho(t+1)V_P(t+1) + \rho(t)V_P(t)}.$$

The wavelet used is a zero phase, Ricker wavelet with a 20 Hz peak frequency (Figure 5.4).

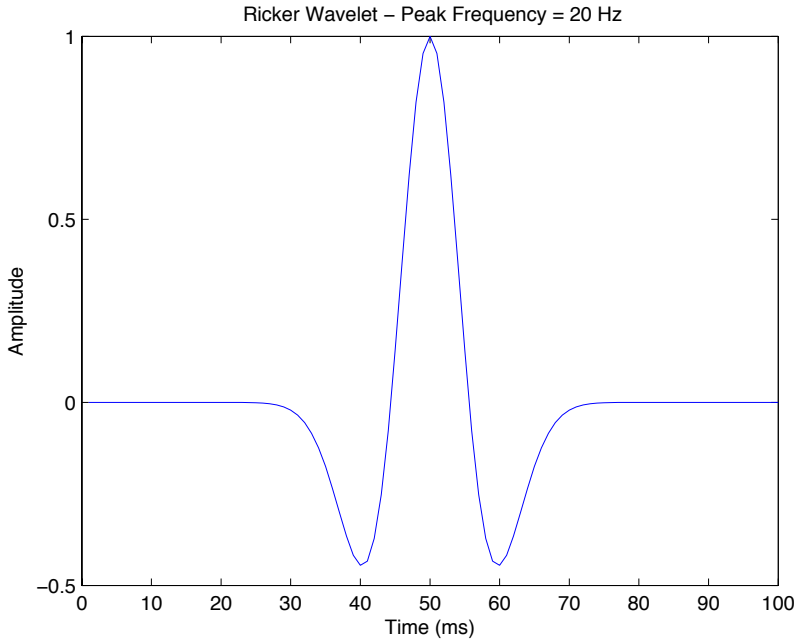

Figure 5.4: Ricker wavelet with a 20 Hz peak frequency used in the seismic modeling.

The post-stack simulated seismic sections (Figure 5.5) are a result of convolving the wavelet with the reflectivity series derived from the acoustic impedance models pre- and post-CO_2 injection.

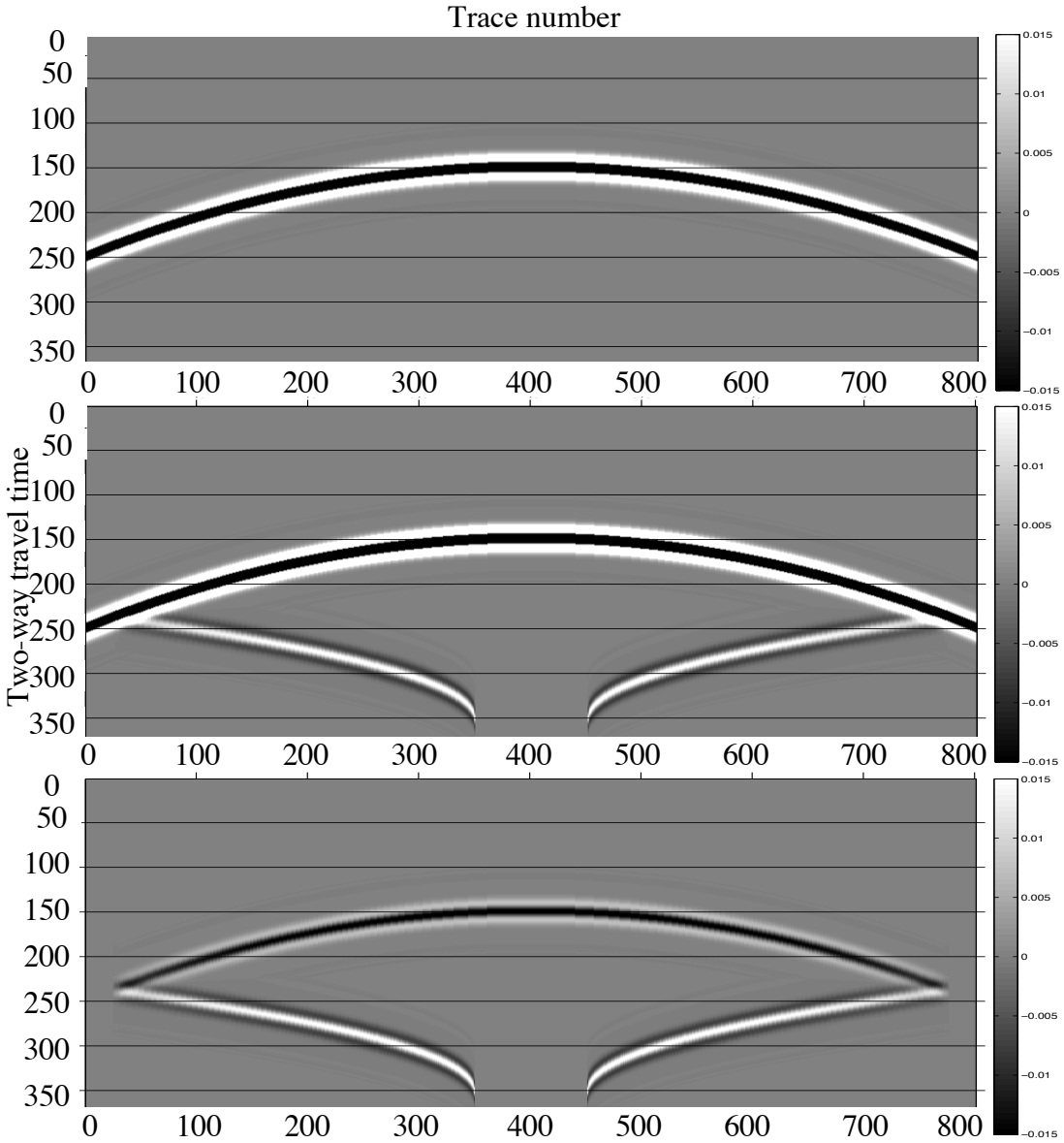

Figure 5.5: Simulated seismic reflection cross-sections for: pre-injection (Top), post-injection (Middle), and the difference of post- and pre-injection (Bottom). The reflection amplitude of the shale-sandstone interface is negative because the brine-saturated and CO_2-saturated reservoir has lower acoustic impedance than the sealing shale. Because the acoustic impedance of the CO_2-saturated reservoir is lower than that of the brine-saturated reservoir, the reflection amplitude off the top of the reservoir is more negative after CO_2 injection. Note the reflections from the fluid (CO_2-brine) contact at the bottom of the plume, which is visible because the thickness of the fluid plume is large enough to yield isolated reflections.

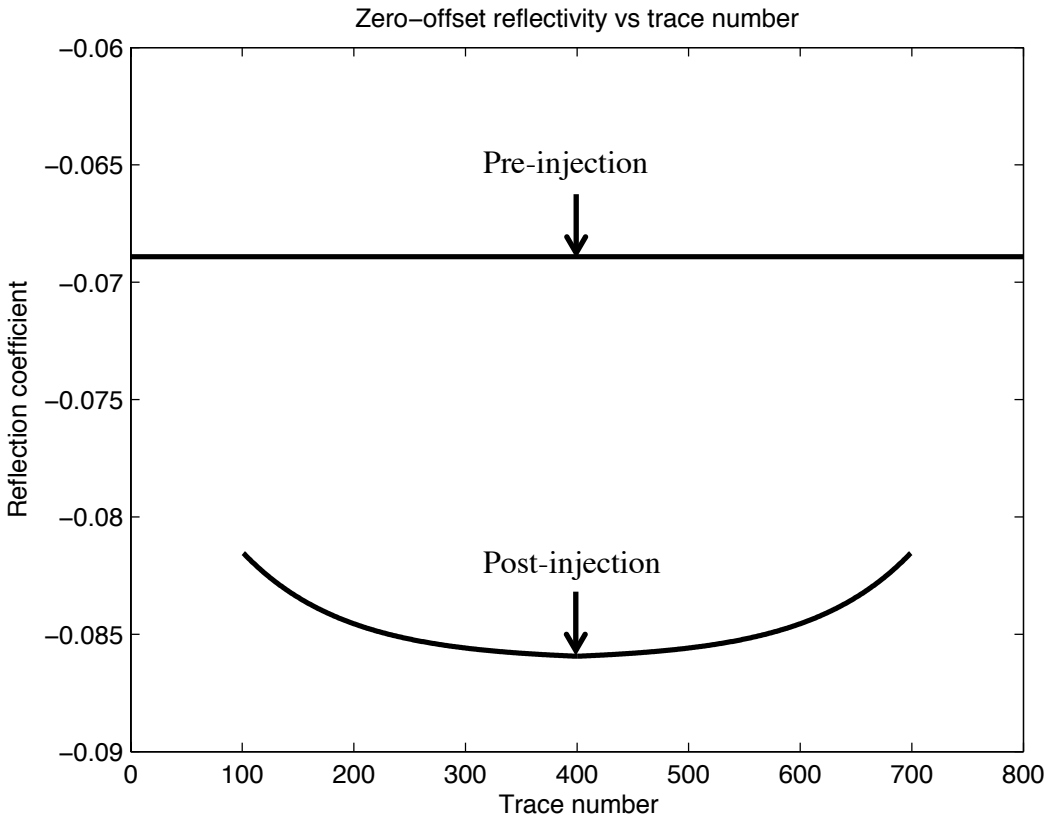

Figure 5.6: Zero-offset reflectivity. The traces of the post-injection reflection coefficients are limited to traces 100-700 to avoid interfering reflections. The amplitude of the reflection from the shale-sand interface is constant before the injection of CO_2. After the injection of CO_2, the magnitude of the reflection coefficient increases and varies with trace number. The largest difference in amplitude occurs at trace #400.

Before simulating the injection of CO_2, the only reflection is from the interface between the shale and brine-saturated sandstone (Figure 5.5), which represents the top of the reservoir. The reflection is negative and constant (Figure 5.6), because the acoustic impedance of the brine-saturated sand is less than that of the shale. After simulating the injection of CO_2, there is a reflection from fluid contact of the CO_2 flank and the brine that is visible due to the sufficient thickness of the plume (Figure 5.5). The amplitude

difference between the two synthetics illustrates how the reflectivity has changed (Figure 5.5). The difference of reflection amplitudes of the post- and pre-injection synthetic seismic sections reveals that the difference in reflection amplitude off the top of the reservoir decreases laterally away from the well (Figure 5.6). This is due to the number of injected pore volumes decreasing away form the well. The amplitude has increased by as much as 25% at the center of the CO_2 plume, which has seen the largest amount of injected pore volumes. In this form, it is difficult to reliably quantify the effect of the chemical reactions and pressure variations on the reflectivity.

PRE-STACK SEISMIC MODELING

The saturation of a free-phase CO_2 and brine mixture makes it difficult to differentiate the effects of the excess compliance due to chemical reactions and the fluid substitution. Therefore, the use of AVA may be used to extract more information about how the bulk modulus and rigidity of the reservoir have changed. Zoeppritz (1919) developed a set of equations to determine reflection coefficients at various angle of incidences for various combinations of incident and reflected wave types. Linear approximations to these equations provide convenient forms to understand reflection coefficients as functions of angle of incidence. Shuey (1985) developed the following approximation for P-P wave reflections

5.3 $$R_{PP}(\theta) \approx R_{P0} + \left[ER_{P0} + {\Delta\gamma}/{(1-\bar{\gamma})^2}\right] sin^2\theta + \frac{1}{2}\frac{\Delta V_P}{\overline{V_P}}(tan^2\theta - sin^2\theta),$$

where

5.4 $$R_{P0} = \frac{1}{2}\left(\frac{\Delta V_P}{\overline{V_P}} + \frac{\Delta\rho}{\bar{\rho}}\right)$$

5.5 $$E = F - 2(1+F)\left(\frac{1-2\bar{\gamma}}{1-\bar{\gamma}}\right)$$

5.6 $$F = \frac{{\Delta V_P}/{\overline{V_P}}}{{\Delta V_P}/{\overline{V_P}} + {\Delta\rho}/{\bar{\rho}}}$$

R_{P0} is the reflectivity at zero-offset, γ is the dynamic Poisson's ratio, and X represents $V_P, \rho,$ or γ; $\Delta X = X_2 - X_1$ and $\bar{X} = \frac{1}{2}(X_2 + X_1)$. The dynamic Poisson's ratio is

5.7 $$\gamma = \frac{V_P^2 - 2V_S^2}{2(V_P^2 - V_S^2)}$$

Generally in practice, the $[tan^2\theta - sin^2\theta]$ term is dropped for values of $\theta < 30^o$. Equation 5.3 is then written as

5.8 $$R_{PP}(\theta) \approx A + Bsin^2\theta$$

where A is the intercept, which is the seismic amplitude at zero offset, and B is the gradient. The equation is valid for small velocity and density contrasts. Figure 5.7 shows the calculated AVA behavior at various injected pore volumes of reactant for S_W=70%.

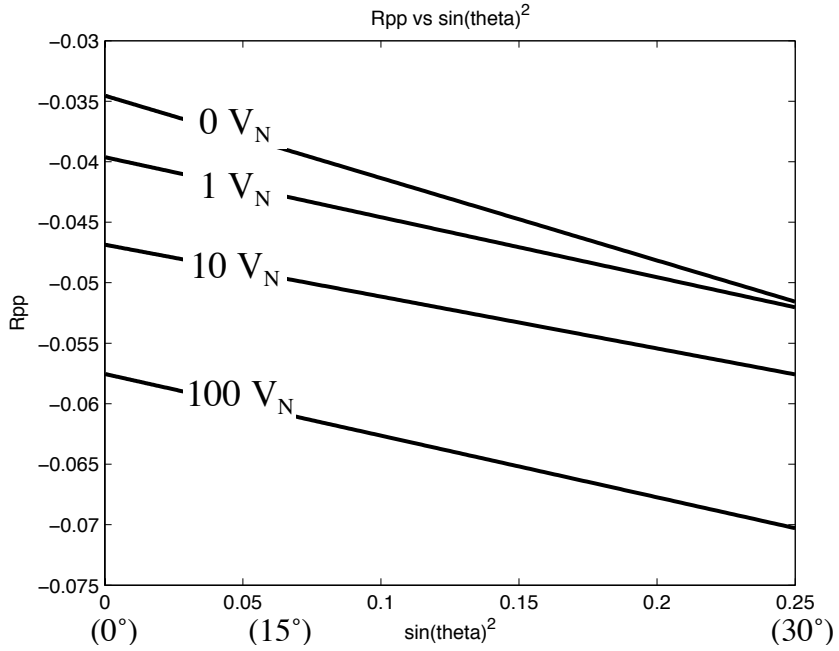

Figure 5.7: P-P reflection coefficients versus angle of incidence for varying injected pore volumes (0, 1, 10 and 100 V_N) and S_W= 70% assuming no dip of the reflective interface. The intercept decreases with increasing injected pore volumes. The AVA gradient (linear slope in terms of $\sin^2(\theta)$) varies yet is negative for all V_N.

The zero-offset intercept of reflectivity increases in magnitude as injected pore volumes and CO_2 saturation increases (Figure 5.8). The intercept becomes more negative as injected pore volumes increase because the acoustic impedance decreases due to increasing excess compliance. The intercept becomes more negative as water saturation decreases because the bulk modulus of CO_2 decreases the overall acoustic impedance of the reservoir.

The AVA gradient depends on the contrast in the dynamic Poisson's ratio of the reservoir. The gradient increases or decreases as the dynamic Poisson's ratio of the reservoir increases or decreases, respectively. Even though the reservoir is weakening overall, the dynamic Poisson's ratio of the reservoir increases with injected pore volumes from 0 to 5 because Vs decreases faster than Vp (Figure 5.9). The gradient becomes more negative with increasing injected pore volumes from 5 to 150 because the dynamic Poisson's ratio of the reservoir decreases. The gradient decreases quickly with decreasing water saturation from 100% to 68%. The gradient increases slowly with decreasing water saturation from 68% to 0%.

A plot of the intercept versus gradient can be helpful to quantify water saturation levels and injected pore volumes for pore volumes less than 5 (Figure 5.10). The solutions for the intercepts and gradients with respect to V_N and S_W become non-unique for V_N>5.

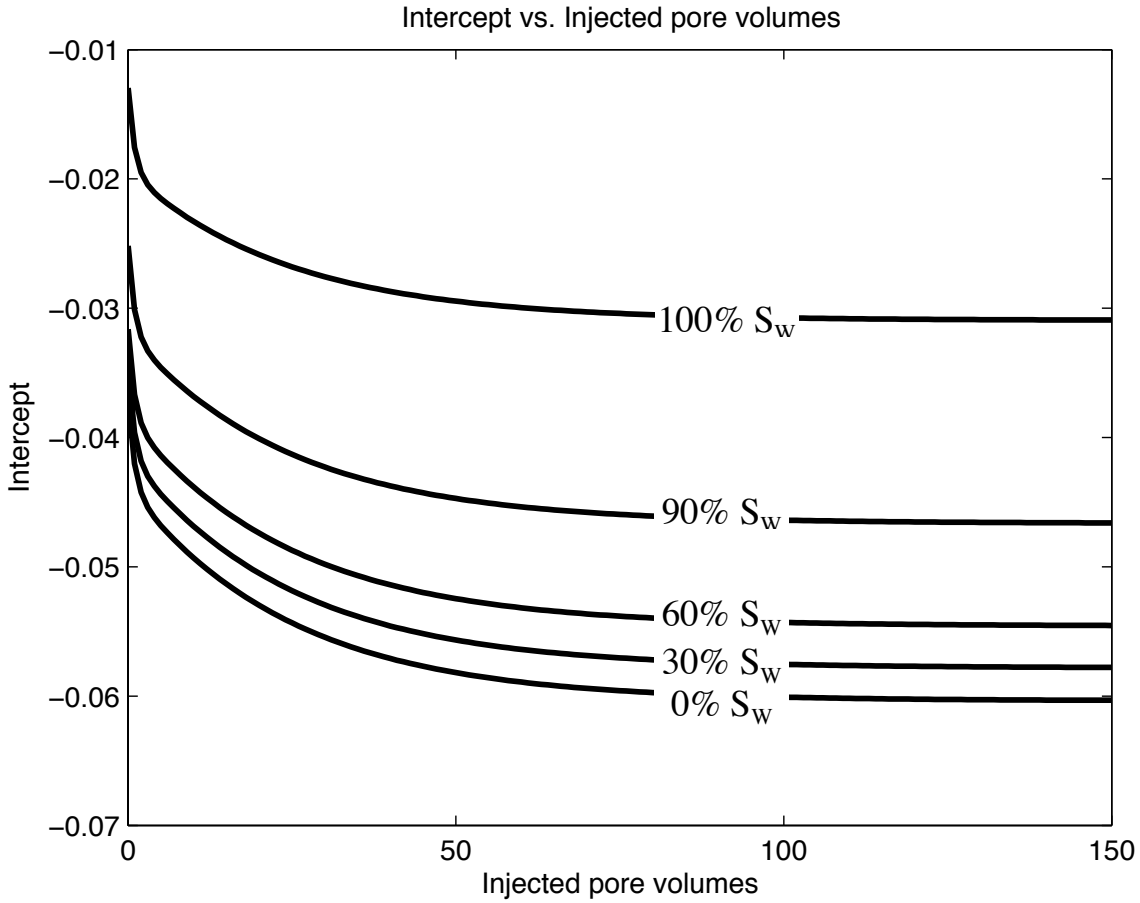

Figure 5.8: Zero-offset intercept of reflectivity as a function of injected pore volumes and water saturation. The intercept decreases exponentially with injected pore volumes because the acoustic impedance decreases exponentially with injected pore volumes. Also, the intercept decreases with decreasing water saturation because the acoustic impedance of the reservoir decreases with increasing free-phase CO_2 saturation. For a given injected pore volume, the acoustic impedance exponentially decreases with decreasing water saturation.

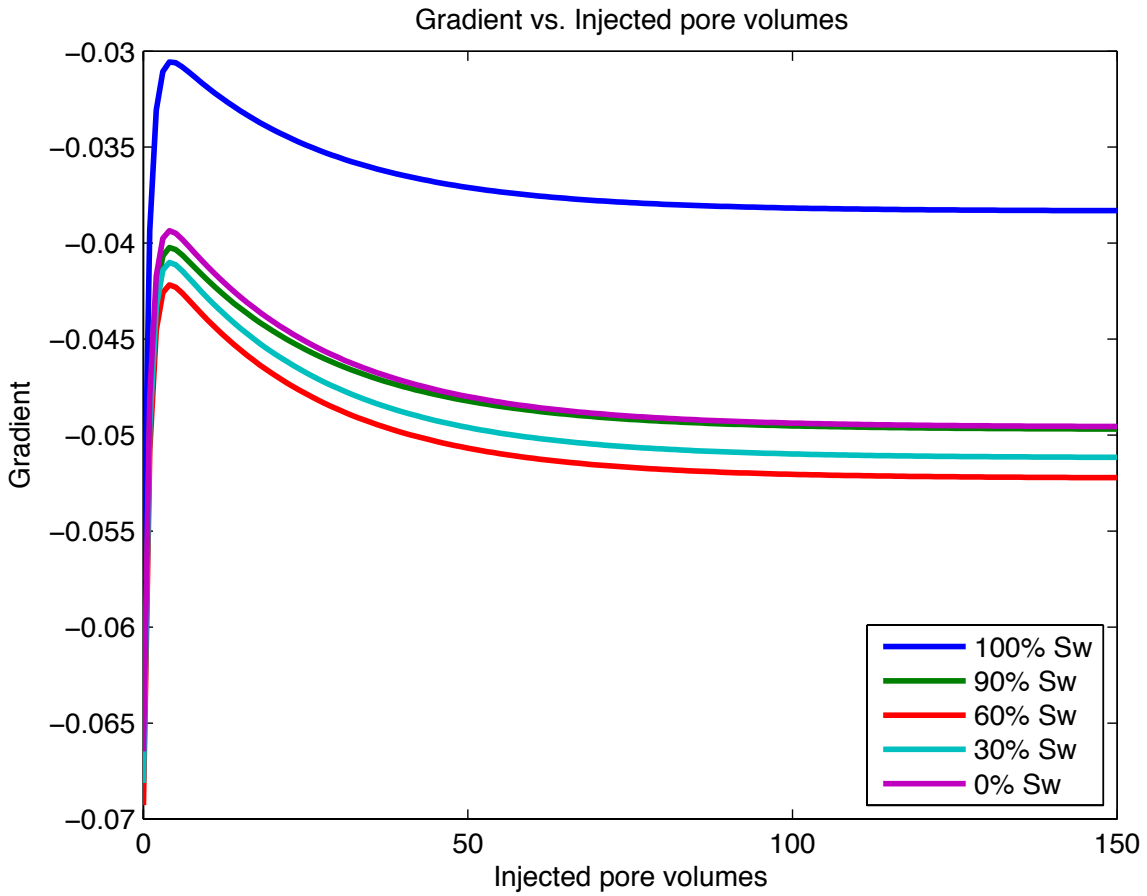

Figure 5.9: AVA gradient as a function of injected pore volumes for various water saturation levels. The gradient is negative for all combinations of water saturation and injected pore volumes. The gradient increases until five total injected pore volumes because the Poisson's ratio of the sandstone increases for all water saturations. The Poisson's ratio increases initially, even though the rock is weakening overall, because Vs decreases faster than Vp decreases. Vs approximately reaches a constant at five pore volumes. Then after five pore volumes have been injected, the gradient decreases exponentially because the Poisson's ratio of the sandstone decreases. The water saturation also has an effect on the gradient. The gradient becomes more negative with decreasing water saturation from 100% to 68% for all injected pore volumes. The gradient increases for water saturations decreasing form 68% to 0% for all injected pore volumes.

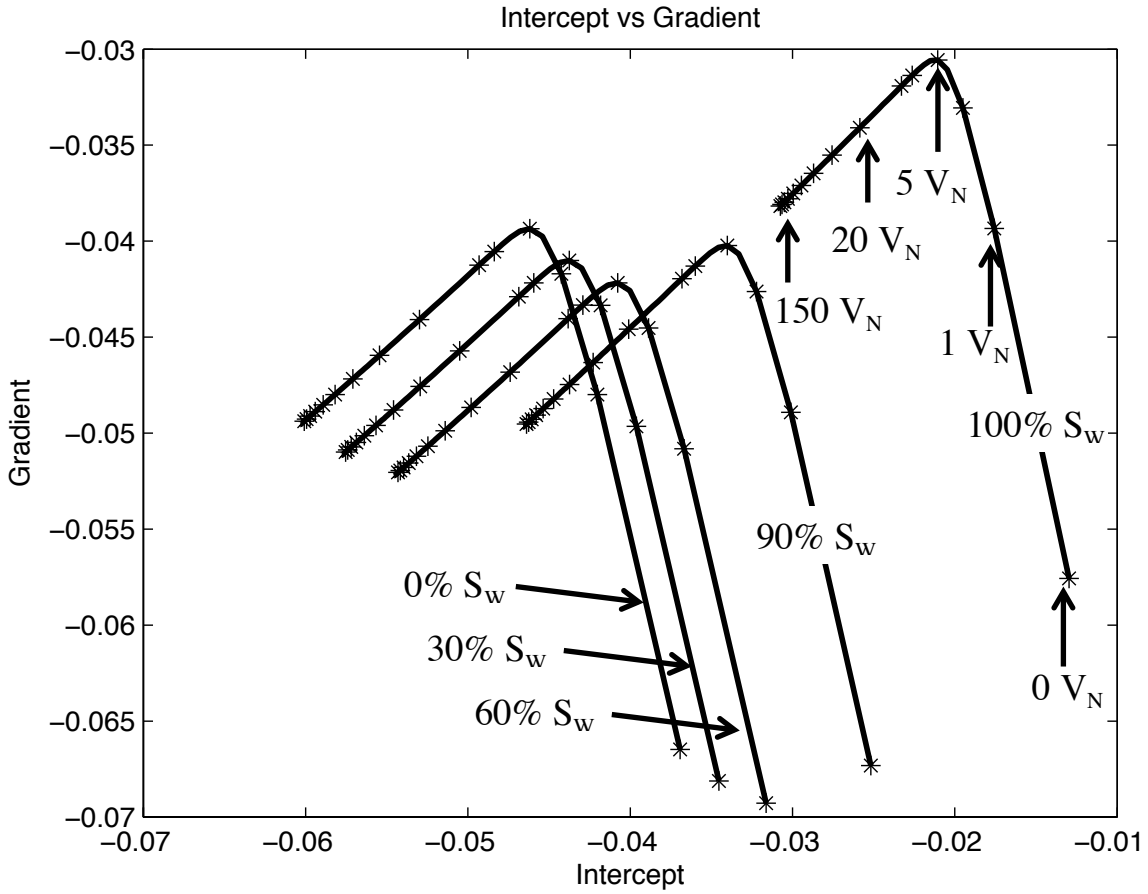

Figure 5.10: AVA intercept versus gradient for varying injected pore volumes of reactant and water saturations. The intercept decreases with increasing injected pore volumes and decreasing water saturation because the acoustic impedance of the reservoir decreases. The gradient increases with increasing pore volumes from 0 to 5 and with decreasing water saturations from 68% to 0%. The gradient becomes more negative with increasing pore volumes from 5 to 150 and with increasing water saturation from 68% to 100%. Multiple solutions (combinations of injected pore volumes and water saturation) may satisfy a given intercept and gradient due to the overlap of multiple curves.

CONCLUSION

The effects of injecting carbon dioxide into the Tuscaloosa sandstone formation can be detected in a simple numerical seismic simulation. Two models are simulated: acoustic impedance models of pre- and post-CO_2 injection. The baseline model consisted of a simple anticline structure of brine-saturated sandstone and a shale seal. The time-

lapse model was similar to the baseline model but had the additional complexity of a CO_2 plume with laterally varying injected pore volumes. The injected pore volumes were the highest (100) at the center of the plume and decreased to 0 at the flank of the plume.

The acoustic impedance of the reservoir prior to injection was less than that of the shale. Therefore, a normal incidence acoustic wave reflected from the top of the reservoir with a negative reflection coefficient. The differential pressure before injection was 35 MPa. The injection of super-critical carbon dioxide decreased the differential pressure (27 MPa), effective elastic properties and density of the reservoir, whereas the seal properties did not change. The mechanically and chemically induced compliance increased the magnitude of the negative reflection coefficient from the top of the reservoir. The difference between the pre-injection and post-injection synthetic seismic data illustrates how various injected pore volumes and 30% CO_2 saturation affect post-stack seismic data. The magnitude of the reflection increased by as much as 25% at the injection zone where the injected pore volumes were the highest. As the injected pore volumes of fluid decreased, the differential amplitude of the time-lapse and baseline seismic data decreased. Interference does not occur until the plume thickness is less than the tuning thickness of 12.5 ms two-way travel time. Tuning occurs at the edge of the flanks. Stacking common depth point (CDP) data may limit the ability to quantitatively interpret seismic data.

Analysis of AVA observations may potentially be used to enhance interpretability, because injecting carbon dioxide can affect the shear properties, particularly the dynamic Poisson's ratio, of a reservoir. Shuey's (1985) form of the linearized Zoeppritz equation (in $\sin^2(\theta)$) was used to estimate the dependency of the amplitude on angle of incidence as a function of injected pore volumes. The following discussion assumes a water saturation of 70% (S_{CO2} = 30%). The intercepts decreased

with increasing injected pore volumes and CO_2 saturation because the acoustic impedance of the reservoir decreased. The gradients increased with increasing injected pore volumes from 0 to 5, because dynamic Poisson's ratio of the reservoir increased. The gradients decreased with increasing injected pore volumes from 5 to 150, because the dynamic Poisson's ratio of the reservoir decreased. Based on the numerical simulation, AVA may potentially be more useful to quantitatively interpret the number of injected pore volumes at a point in the reservoir than the difference in post-stack seismic data for a given water saturation.

This is a simplified seismic model for six primary reasons. The model does not take into account

1. overburden effects,
2. variability in the mixture of dissolved CO_2, free-phase CO_2, and brine,
3. frequency-dependent seismic velocity,
4. upscaling from the experimental data,
5. uncertainty, and
6. reaction time of the chemical reactions.

The depth of the Lower Tuscaloosa formation in Cranfield Field, Mississippi, could pose an issue while extracting amplitudes of reflection events. Energy of seismic waves dissipates with the distance from the energy source (Guéguen and Palciauskas, 1994), which may make the amplitude difference after injecting CO_2 within the noise level of real data. Also, the frequency content of a reflection from 11,000 feet depth may be limited to low frequencies. If the layers of interest fall below seismic resolution, detecting velocity changes from noisy time-lapse data may be impaired.

The mixture of dissolved CO_2, free-phase CO_2, and brine may be quite complicated. The way in which the fluid is distributed (patchy or uniform) may have a

significant impact on the seismic response. The fluids of patchy and uniform mixtures are modeled with iso-strain and iso-stress models, respectively (Mavko et al., 2009). For example, a patchy mixture tends to have a larger effective bulk modulus than a uniform mixture. The injection of CO_2 may initially cause the fluid mixture to be patchy, pore pressure to be heterogeneous and there to be a small amount of dissolved CO_2. With time, the fluid mixture may become uniform with homogeneous pore pressure and a greater amount of dissolved CO_2. The amount of dissolved CO_2 in brine, which yields carbonic acid, is the controlling factor of the chemical reactions.

Dispersion of seismic wave velocities may cause the laboratory observations to be different than the field observations. For example, the elastic wave velocities measured in the lab tend to be faster than those measured in the field. The ultrasonic frequencies (megahertz range) of the laboratory equipment cause the dynamic elastic moduli of the core plug to increase compared to the lower frequency range of seismic and borehole observations (in terms of hertz to kilohertz range, respectively). Also, viscosity of fluids cause wave velocities to be dispersive, which is the reason for drying the core plugs before the travel times of P- and S-waves were measured. Measuring velocities on dry samples minimizes, but does not completely remove, the effects of dispersion (Mavko et al., 2009).

Scaling from laboratory measurements to the field scale poses a problem. Representing an entire reservoir with measurements made on a core plug may be unrealistic, but it may be the best available data. The issue with scaling is heterogeneity. For example, a range of sandstones, calcite-cemented conglomerates to well sorted and clean, make up the Lower Tuscaloosa Sandstone reservoir in the Cranfield Field, Mississippi. The effects of injecting carbon dioxide may vary significantly throughout the reservoir as seen in chapter 4. For example, the response of CO_2-rich brine injection

on sample Y was different than the response of sample A. The seismic wave in the field essentially averages the effects of chemical reactions and pressure variations within the reservoir because the wavelength of the seismic wave is much larger than the ultrasonic wave produced in the lab.

Uncertainty must be considered in any simulation that uses empirical relationships. The error of the velocity measurements in chapter 4 is about ±1%. Therefore, error is velocity dependent. The explanation of possible sources of error is located at the end of chapter 4. Besides experimental error, there is also an unquantifiable amount of error associated with Gassmann's fluid substitution model (1951). Models are approximations at best. However, the sandstone, on which the fluid substitution calculation is performed, is fairly porous (10% to 30%) and permeable (0.1 mD to 1000 mD) (Kordi et al., 2010), which allows the fluid to re-equilibrate under applied stress. Thus, dispersion caused by fluid saturation is minimized in the field.

Reaction time may be a critical variable to model the long-term chemical effects of injecting carbon dioxide. With time, pressure will homogenize, chemical reactions will reach a steady state, and fluid mixtures will become uniform. In this study, time was limited in the experiments and does not seem to play an important role for the chemical reactions. The elastic wave velocities of the core plugs reached constant values with the injection of CO_2-rich brine on the time scale of the experiments. However, the time duration (years) of the experiment is not comparable to the time duration of injection or storage. Therefore, effects that occur on a longer time scale are unknown.

REFERENCES

Gassmann, F., 1951, Über die Elastizität poröser Medien. *Vierteljahrsschrift der Naturforschende Gesellschaft Zürich*, **96**, pages 1-23.

Guéguen, Y. and Palciauskas, V., 1994, Introduction to the physics of rocks. Princeton University Press, Chichester, West Sussex, pages 169-175.

Kordi, M., Hovorka, S., Milliken, K., Treviño, R., and Lu, J., 2010, Diagenesis and reservoir heterogeneity in the Lower Tuscaloosa Formation at Cranfield Field, Mississippi: presented at the 60th Annual Convention of the Gulf Coast Association of Geological Societies and the Gulf Coast Section of SEPM, San Antonio, Texas, October 10-12, 2010. GCCC Digital Publication Series #10-13.

Mavko, G., T. Mukerji, and J. Dvorkin, 2009, The rock physics handbook: tools for seismic analysis of porous media, 2nd Ed. New York: Cambridge University Press, 21-24.

Sheriff, R. E. and Geldart, L. P., 1995. Exploration seismology, 2nd Ed. New York: Cambridge University Press

Shuey, R.T., 1985. A simplification of the Zoeppritz equations. *Geophysics*., **50**, 609-614.

Stein, S. and Wysession, M., 2003, An introduction to seismology, earthquakes, and earth structure, Blackwell Publishing, MA, page 150.

Vilarrasa, V., Bolster, D., Dentz, M., Olivella, S., and Carrera, J., 2010, Effects of CO_2 compressibility on CO_2 storage in deep saline aquifers, Springer, *Transport in Porous Media*, 11242.

Zoeppritz, K., 1919. On the reflection and propagation of seismic waves. *Göttinger Nachricten,* pages 66-84.

Chapter 6: Conclusion

SUMMARY AND CONCLUSIONS

The aim of this thesis was to quantify the effects of pressure variations and chemical reactions on the elasticity of the Lower Tuscaloosa Sandstone of Cranfield Field in Mississippi. The background and experimental data are stepping stones in using surface seismic data to quantify the amount of carbon dioxide retained in the subsurface for carbon capture and storage pertinent to the Cranfield site. The results of the experiments yield the response of two subsurface core samples to the injection of carbon dioxide-rich brine and variations of differential pressure. Using the experimental results, I developed a simplified reservoir model to study the P-P seismic response of injecting carbon dioxide into the subsurface. The following paragraphs discuss the progress made in the field of time-lapse rock physics and a summary of the project. Note any reference to velocities refer to the elastic wave propagation velocities of the "dry" frame.

The injection of a reactive fluid into the subsurface may induce excess compliance or stiffness in the "dry" frame of the rock not predicted by traditional fluid substitution models. Traditional fluid substitution models, such as Gassmann's (1951), do not take into account that chemical reactions may alter the microstructure of the rock by precipitating or dissolving minerals at grain contacts or within the pore space. The precipitation or dissolution of minerals causes the "dry" frame to stiffen or soften, respectively. Also, the injection of fluid at high pressure could mechanically alter the rock. Therefore, allowing the elastic parameters of the "dry" frame to vary, based on the amount of injected fluid and differential pressure, during a fluid substitution calculation should yield a more reliable result.

The effects of pressure variations and chemical reactions on the compressional and shear wave velocities of the Lower Tuscaloosa Sandstone were measured after

injecting the core plugs with carbon dioxide-rich brine and varying the differential pressure. Before injecting the sample with reactant, the baseline velocities were measured as functions of differential pressure. The sample was then injected with a given amount of pore volumes and dried. Again, the velocities were measured as functions of differential pressure. This process was repeated for a total of four to five injections on each sample.

The results of the experiment indicate that dissolution of iron bearing minerals altered the microstructure of the samples. The elastic wave velocities of the samples decreased exponentially with increasing injected pore volumes of carbon dioxide-rich brine. At a differential pressure of 27 MPa, the Vp and Vs of sample A decreased by a maximum of 200 m/s (-4.9%) and 70 m/s (-2.9%), respectively, after injecting about 160 pore volumes of CO_2-rich brine. The Vp and Vs of sample Y decreased by a maximum of 480 m/s (-15.6%) and 210 m/s (-10.5%), respectively, after injecting about 135 pore volumes of CO_2-rich brine. The velocity measurements were within a precision of ±1%.

The elastic wave velocities were found to be approximately linearly proportional to differential pressure between 20 and 55 MPa. Note that these velocities were measured on the samples prior to injection. Decreasing the pressure from pre-injection field conditions (35 MPa) to post-injection field conditions (27 MPa) decreased the Vp and Vs of sample A by 60 m/s (-1.9%) and 20 m/s (-1.6%), respectively. For sample Y, Vp and Vs decreased by 45 m/s (-1.0%) and 40 m/s (-1.9%), respectively, by changing the differential pressure from 35 MPa to 27 MPa.

Both samples A and Y were more sensitive to the chemical reactions associated with the injection of the reactant than to lowering differential pressure by 8 MPa. In conjunction, chemical reactions and pressure variations may have a significant impact on the elasticity of the host rock. Therefore, their total effect must be taken into account

while performing a fluid substitution calculation. For sample A, the combination of injecting 160 pore volumes and decreasing differential pressure from 35 MPa to 27 MPa decreased the bulk modulus and rigidity of the "dry" frame by 14.7% and 9.2%, respectively. For sample Y, the combination of injecting 135 pore volumes and decreasing differential pressure from 35 MPa to 27 MPa decreased the bulk modulus and rigidity of the "dry" frame by 39.0% and 20.1%, respectively. These results must be taken into account while performing fluid substitution calculations to be accurate.

The effects of chemical reactions on the elastic properties of the host rock reached a limit when a critical number of pore volumes were injected, which occurred well before the end of the experiments. One surprising point is that the critical volume of injected fluid for each elastic parameter depends on differential pressure, which can be interpreted from figures 4.14-17. At a differential pressure of 27 MPa, the critical injected pore volumes for the bulk modulus and rigidity of sample A were 80.5 and 2.2, respectively. The critical injected pore volumes for the bulk modulus and rigidity of sample Y were 9.6 and 19.7, respectively, at a differential pressure of 27 MPa. This indicates that the differences in critical injected pore volumes for the samples and their elastic properties arise from variations in mineral in composition.

The time duration of storage may be an important variable when considering the effects of chemical reactions on the elasticity of rocks. In this case, steady state values of the elastic properties of two samples were met within the time-scale of the laboratory observations (less than 48 to 60 hours). The experiments, however, do not address effects of chemical reactions that occur on a longer time-scale. Thus, I limit my conclusion of the experiments to the volume of injected effects fluid for the Lower Tuscaloosa Sandstone of the Cranfield Field.

Even though it is unclear which minerals have dissolved, titrations of the fluid after the first flow through experiment yielded an iron concentration of 40-80 mg/L. Titrations of the fluid used in subsequent flow through experiments yielded iron concentrations below the resolution of the method. According to Lu et al. (2011), the source of iron may be iron hydroxide.

SEM images were used to qualitatively understand why the elastic wave velocities of the core plugs changed with the injection of CO_2-rich brine. The images of the samples before and after the injection of CO_2-rich brine showed that dissolution has occurred in both samples. Cement at grain contacts and away from grain contacts dissolved, leaving behind cracks. The introduction of cracks into the microstructure of the samples is the likely cause of the drop in velocities because cracks induce excess compliance.

I performed a simplified seismic simulation of the effects of injecting carbon dioxide into a brine reservoir. The simulation consisted of building two acoustic impedance models: pre- and post-injection. The reservoir for both models was a simple anticline made of sandstone with a shale seal. The properties of the shale were estimated using well log data, and the properties of the sandstone were estimated using the experimental results of sample A in conjunction with my chemical fluid substitution model. The reservoir was 100% saturated with brine in the pre-injection model. The reservoir of the post-injection model had a CO_2 plume with 30% free-phase CO_2 saturation. Also, the injected pore volumes varied linearly from 100 at the center of the plume to 0 at the edge of the plume. Using the convolutional model with a 20 Hz Ricker wavelet, I found that the magnitude of the negative reflection coefficient from the top of the reservoir increased by 25% after the injection of CO_2. Differentiating between chemical reactions and fluid substitution effects was not possible in post-stack seismic

amplitudes. Pre-stack amplitude analysis may add quantitative interpretability because of the added effect of dynamic Poisson's ratio on seismic data at various angles of incidence. Shuey's (1985) linearized form of Zoeppritz's equations showed that the intercept became more negative with increasing injected pore volumes. The calculated intercept became more negative with increasing injected pore volumes because chemical reactions decreased the acoustic impedance of the reservoir. The gradient increased with increasing injected pore volumes from 0 to 5 because the dynamic Poisson's ratio of the reservoir increased. However, the gradient decreased with increasing injected pore volumes from 0 to 5 because the dynamic Poisson's ratio decreased. Therefore, it may be possible to map gradients to injected pore volumes for a uniform free-phase CO_2 saturation for a two-layer model.

FUTURE RECOMMENDATIONS

This project is a stepping-stone for future work in the field of time-lapse geophysics and rock physics. To better understand the effects of injecting carbon dioxide on elastic properties, a number of improvements can be made to the project to make the chemical fluid substitution model more accurate. First, include time as an experimental variable. Time may play an important role in the long-term effects of chemical reactions on the elasticity of rocks, because the amount of dissolution or precipitation depends on time. Next, perform the experiments at the reservoir temperature, which may depend on time, because temperature is another factor that influences rates of chemical reactions. Currently, there is very little information about mechanical properties of H_2O and CO_2 (dissolved and free-phase) mixtures at varying temperatures and pressures, which is crucial for performing accurate fluid substitution calculations. Therefore, determining the mechanical properties of the fluid mixtures is essential. Finally, perform experiments

on more core samples of the Lower Tuscaloosa Sandstone to build a heterogeneous reservoir model. For example, the lower conglomerate of the reservoir has not been tested and comprises about 25% of the height of the reservoir. Therefore, the effects of CO_2 injection on the lower conglomerate could potentially affect the time-lapse field seismic data. Study thin sections and chemical compositions of the core plugs before and after experimentation to understand which minerals react with the carbon dioxide-rich brine. Finally, use existing rock physics models, such as the self-consistent or the differential effective medium theory, to model the change in elasticity of the host rock due to the dissolution or precipitation of various minerals.

REFERENCES

Gassmann, F., 1951, Über die Elastizität poröser Medien. *Vierteljahrsschrift der Naturforschende Gesellschaft Zürich*, **96**, pages 1-23.

Lu, J., Kharaka, Y., Thordsen, J., Horita, J., Karamalidis, A., Griffith, C., Hakala, A., Ambats, G., Cole, D., Phelps, T., Cook, P., Manning, M., and Hovorka, S., 2011, Geochemical interactions in the Lower Tuscaloosa reservoir at the Cranfield CO_2 sequestration site, Mississippi, USA, Elsevier Editorial System for Chemical Geology, in press.

References

Avseth, P., Dvorkin, J., Mavko, G., and Rykkje, J., 2000, Rock physics diagnostic of north sea sands: Link between microstructure and seismic properties. *Geophys. Res. Lett.*, 27(17), 276102764, doi:10.1029/1999GL008468.

Brown, R. and Korringa, J., 1975. On the dependence of the elastic properties of a porous rock on the compressibility of the pore fluid. *Geophys.* **40**, 608-616.

Darcy, H., Les Fontaines Publiques de la Ville de Dijon, Dalmont, Paris (1856).

Dvorkin, J. and A. Nur, 1996, Elasticity of High-porosity sandstones: Theory for two North Sea datasets, Geophysics, 61, 1363-1370.

Dvorkin, J., and Brevik, I., 1999, Diagnosing high-porosity sandstones: Strength and permeability from porosity and velocity, *Geophysics*, **64**, 795-799

Gassmann, F., 1951, Über die Elastizität poröser Medien. *Vierteljahrsschrift der Naturforschende Gesellschaft Zürich*, **96**, 1-23.

Guéguen, Y. and Palciauskas, V., 1994, Introduction to the physics of rocks. Princeton University Press, Chichester, West Sussex, pages 169-175.

Hill, R., 1952, The elastic behavior of a crystalline aggregate: *Proc. Phys. Soc. London Ser. A*, **65**, 349-354.

Hovorka, S., 2009, Frio brine pilot: The first U.S. sequestration test, *Southwest Hydrology*, **8**(5), 26-31.

Hovorka, S. D., T. A. Meckel, R. H. Treviño, J. P. Nicot, J. W. Choi, J. Lu, H. Zeng, K. Romanak, C. Yang, M. Kordi, and P. Wang, SECARB Phase II – Cranfield, MS: presented at the Southern States Energy Board Stakeholders' Meeting, Atlanta, Georgia, March 3, 2009. GCCC Digital Publication #09-03.

Kharaka, Y.K., Cole, D.R., Hovorka, S.D., et al.., 2006, Gas-water-rock interactions in Frio Formation following CO2 injection: Implications for the storage of greenhouse gases in sedimentary basins, *Geol.*, 34(7): 577-580.

Klinkenberg, L. J.: 1941, The permeability of porous media to liquids and gases, Drilling and Production Practice, American Petroleum Inst., pp. 200–213.

Kordi, M., Hovorka, S., Milliken, K., Treviño, R., and Lu, J., 2010, Diagenesis and reservoir heterogeneity in the Lower Tuscaloosa Formation at Cranfield Field, Mississippi: presented at the 60th Annual Convention of the Gulf Coast Association of

Geological Societies and the Gulf Coast Section of SEPM, San Antonio, Texas, October 10-12, 2010. GCCC Digital Publication Series #10-13.

Kotz, J. C., Treichel, P., and Townsend, J. R. 2009. Chemistry and chemical reactivity, vol. 2. Califronia: Thomson Higher Education, 671-703.

Lu, J., Kharaka, Y., Thordsen, J., Horita, J., Karamalidis, A., Griffith, C., Hakala, A., Ambats, G., Cole, D., Phelps, T., Cook, P., Manning, M., and Hovorka, S., 2011, Geochemical interactions in the Lower Tuscaloosa reservoir at the Cranfield CO_2 sequestration site, Mississippi, USA, Elsevier Editorial System for Chemical Geology, in press.

Mavko, G., T. Mukerji, and J. Dvorkin, 2009, The rock physics handbook: tools for seismic analysis of porous media, 2nd ed. New York: Cambridge University Press, 21-24.

Mikkelsen, E. R., 2009. Monitoring of CO_2 sequestration at the Longyearbyen CO_2 lab by time-lapse seismic, Master's thesis, Norwegian University of Science and Technology.

Mississippi Oil and Gas Board, 1966. Mississippi Oil and Gas Board (MOGB), Cranfield Field, Cranfield unit, basal Tuscaloosa reservoir, Adams and Franklin Counties, pp. 42-58.

Romanak, K.D., 2010, Monitoring CO_2 storage in deep geological formations: presented at the University of Bern, Bern, Switzerland, November 10th, 2010. GCCC Digital Publication Series #10-17.

Schmidt, P. S., O. Ezekoye, J. Howell, and D. Baker. 2006. Thermodynamics: An Integrated Learning System. Hoboken: John Wiley & Sons, Inc.

Sheriff, R. E. and Geldart, L. P., 1995. Exploration seismology, 2nd Ed. New York: Cambridge University Press

Shuey, R.T., 1985. A simplification of the Zoeppritz equations. *Geophysics*., **50**, 609-614.

Southeast Regional Carbon Sequestration Partnership (SECARB), 2011, Phase III early CO2 injection field test at Cranfield.

Span, R. and Wagner, W., 1996. A new equation of state for carbon dioxide covering the fluid region from the triple-point to 1100 K at pressures up to 88 MPa. Journal of Physical and Chemical Reference Data, **25**(6), 1509-1596.

Stein, S. and Wysession, M., 2003, An introduction to seismology, earthquakes, and earth structure, Blackwell Publishing, MA, page 150.

Timoshenko, S.P. and Goodier, J.N., 1934. Theory of Elasticity. New York: McGraw-Hill.

Vanorio, T. et al., 2010. The rock physics basis for 4D seismic monitoring of CO2 fate: Are we there yet?. *The Leading Edge*, Feb., 156-162.

Vanorio, T., Nur, A., and Ebert, Y., 2011, Rock physics analysis and time-lapse rock imaging of geochemical effects due to the injection of CO2 into reservoir rocks, *Geophysics*, in press.

Vilarrasa, V., Bolster, D., Dentz, M., Olivella, S., and Carrera, J., 2010, Effects of CO2 compressibility on CO2 storage in deep saline aquifers, Springer, *Transport in Porous Media*, 11242.

Walsh, J. B., 1965, The effect of cracks on the compressibility of rock: *Journal of Geophysical Research*., **70**, 381-390.

Zoeppritz, K., 1919. On the reflection and propagation of seismic waves. *Göttinger Nachricten,* pages 66-84.